Int. J. Advanced Design and Manufacturing Technology, 2025, Vol. 18, No. 4, pp. 1-9

DOI: *ISSN: 2252-0406* *https://admt.isfahan.iau.ir*

Three-Dimensional Finite Element Analysis of Equivalent Plastic Strain Distribution and Compressive Residual Stress in the Surface Mechanical Attrition Treatment Process of AZ31 Magnesium Alloy

Ali Kazemi, Ali Heidari *, Kamran Amini, Farshid Aghadavoudi, Mohsen Loh-Mousavi

Department of Mechanical Engineering, Khomeinishahr Branch, Islamic Azad University, Khomeinishahr/Isfahan, Iran

E-mail: en_alikazemi975@yahoo.com, heidari@iaukhsh.ac.ir, kamini@iaukhsh.av.ir, aghadavoudi@khsh.ac.ir, lohmousavi@iaukhsh.ac.ir

*Corresponding Author

Received: 15 July 2025, Revised: 28 August 2025, Accepted: 8 September 2025

Abstract: Surface Mechanical Attrition Treatment (SMAT) is a process in which the surface of a component is enhanced by the impact of small steel shots, creating a thin nanostructured layer that improves the mechanical properties of metallic materials. In this process, significant plastic deformation initially occurs due to the impact of steel shots on the surface, and after each shot rebounds, compressive residual stress is generated on the surface. This study numerically investigates the effect of shot size and speed of shot balls on equivalent plastic strain profiles, residual stress depth, and maximum compressive residual stress during the SMAT process of AZ31material using the Finite Element Method (FEM). The plastic deformation process during SMAT was analyzed using ABAQUS Explicit Software. The Explicit Dynamic solver was employed to analyze the effects of shot velocity and diameter using FEM. The results indicated that the maximum compressive residual stress increased from 202 MPa to 205 MPa as the shot diameter increased from 1 mm to 3 mm at a velocity of 10 m/s, while an increase in velocity from 4 m/s to 10 m/s at a shot diameter of 1 mm resulted in an increase in maximum compressive residual stress from 155 MPa to 202 MPa. The results suggest that shot velocity has a significant effect on residual stress, whereas shot diameter has less impact. The change in plastic strain due to shot diameter is less influential than shot velocity. With the help of the method developed in this study, it is possible to achieve the effects of effective parameters in the process, which are very difficult and expensive to achieve with practical methods.

Keywords: AZ31 Magnesium Alloy, Finite Element Method, Residual Stress, SMAT

Biographical notes: Ali Kazemi received his PhD in Mechanical Engineering in 2024. **Ali Heidari** is an Associate Professor at the Department of Mechanical Engineering, Khomeinishahr Branch, Islamic Azad University, Isfahan, Iran. **Kamran Amini** is an Associate Professor at the Department of Mechanical Engineering, Khomeinishahr Branch, Islamic Azad University, Isfahan, Iran. **Farshid Aghadavoudi** is an Associate Professor at the Department of Mechanical Engineering, Khomeinishahr Branch, Islamic Azad University, Isfahan, Iran. **Mohsen Loh-Mousavi** is an Assistant Professor at the Department of Mechanical Engineering, Khomeinishahr Branch, Islamic Azad University, Isfahan, Iran.

Research paper

1 INTRODUCTION

SMAT is an effective technique that enhances the mechanical properties of metal by inducing surface nano crystallization. During this process, spherical shots with high kinetic energy are randomly and continuously impacted onto the surface of a sample multiple times within a chamber by an ultrasonic generator [1-2]. Each shot creates a plastic zone with permanent deformation, surrounded by an elastic region that has not yet reached the plastic limit and remains elastically deformed. This elastic region tends to return to its original state, exerting pressure on the plastic zone, thereby generating compressive residual stress. The multiplicity and overlap of these indentations eventually result in the formation of a layer with compressive residual stress on the surface of the component. This layer significantly enhances the fatigue strength of the component. Therefore, predicting the shape and magnitude of the subsurface residual stress distribution after the SMAT process is of great importance [3-4]. Shot velocity can vary depending on the applied vibration frequency, amplitude, chamber geometry, and shot properties. Shot velocity is the most critical parameter in surface treatment using the SMAT process, and the height and diameter of the SMAT device chamber directly affect shot velocity. Therefore, many researchers have considered shot velocity as the average speed in the SMAT process. In a study, Zhang et al. [5] examined the effect of the SMAT process on the surface of AISI 304 steel using a numerical simulation based on the Johnson-Cook method. Based on the simulation results, the distribution of residual stress was investigated, and the impact of impact frequency and shot size on compressive residual stress was analyzed. The findings indicated that when the only variable parameter is the SMAT process intensity, it effectively means a change in velocity. The depth of residual stress penetration increases significantly with intensity, and the maximum compressive residual stress also slightly increases. Meguid et al. [6] conducted a comprehensive nonlinear dynamic analysis involving an elastoplastic target material and the impact of two shots with varying central distances from each other. The results demonstrated that decreasing the central distance between the two shots increases the depth of the compacted layer due to the overlapping effects of the shots on the surface. They compared double and single impacts on the target material's surface, showing that first, the dynamic friction coefficient has no effect on residual stress distribution, and second, multiple impacts have a significant influence on achieving uniform residual stress distribution across the surface and depth of the target material. For the vibration chamber, Todaka et al. [7] selected an amplitude of 90 micrometers, a frequency of 20 kHz, and a throw distance of 10 mm, claiming that shot velocity could be less than 20 m/s. Chaise et al. [8] used a piezoelectric transducer with a frequency of 20 kHz, setting the amplitude of vibration at 25 micrometers, the vibration chamber height at 50 mm, and the average shot velocity for the numerical model at 4 m/s. Astaraee et al. [9] set the average shot velocity in the vibration chamber at 3.6 m/s in a numerical model. Yin et al. [10] considered the average shot velocity in their study to be 3.6 m/s. Manchoul et al. [11] determined the average shot velocity to be 4 and 8 m/s for two different amplitudes of 32 and 64 micrometers and a constant frequency of 20 kHz. Meng et al. [12] investigated the deformation behavior of AZ31 magnesium alloy using the SMAT process, revealing that the surface grain size reached the nanoscale, with grain size decreasing near the surface and becoming less apparent in the layers closer to the core until it disappeared. Zhang et al. [13] studied the effect of surface mechanical attrition on the nanostructured layers of AISI 304 stainless steel. According to their experiments, the nanostructure was successfully fabricated on the surface layers. XRD results showed that the peak heights were shorter and broader, indicating grain refinement, which led to improved mechanical properties. In another study, Bagherifard et al. [14] investigated the impact of shot peening on the structural behavior of titanium by combining finite element simulations with experimental tests. They calculated factors such as residual stress and X-ray diffraction patterns, concluding that the formation of small crystal regions on the shot impact surfaces leads to improved material strength. Anand Kumar et al. studied the effects of SMAT treatment on the fatigue life of alloy 718. SMAT was performed in vacuum with 5 mm diameter steel balls for 30 and 60 min at a vibration frequency of 50 Hz. SMAT resulted in increased tensile strength, decreased ductility, and increased fatigue life. According to their results, no significant difference was observed between the fatigue life of samples with SMAT times of 30 and 60 seconds.[15]. Given the high cost of experimental tests and the complexity of the SMAT process, numerical simulation methods have been used to examine the influential parameters in this process. For example, investigating the effect of each frequency would require designing a new tool, which involves design challenges and additional costs. Therefore, researchers have tended towards numerical studies [16-21]. Consequently, a highly practical approach to solving such issues is the use of finite element methods. The aim of this study is to statistically analyze the effects of shot diameter and velocity in the SMAT process on residual stress variations and to examine the plastic strain profiles of AZ31 magnesium alloy. In this research, numerical simulations were conducted using an explicit dynamics solver, and residual stress on the surface and in-depth was assessed using the results of finite element simulations.

2 MATERIALS AND METHODS

Considering the nature of the process, which affects the metal surface, shot peening (SP) and SMAT are practically similar; however, the SMAT process differs from the shot peening process in terms of its principles and methods. In the SMAT process, several ball shots impact on surface of the target material. The shot velocities in the SMAT process (generally ranging from 1 to 20 m/s) are lower compared to those in shot peening (usually 20 to 150 m/s). This difference in velocity can lead to a reduction in the energy delivered by the impacting shot, especially in the case of smaller shots. However, to compensate for the lower energy resulting from the reduced velocity in the SMAT process, larger shots are used. During SMAT, ultrasonic vibration at a high frequency of over 20 kHz causes the shots to continuously and randomly impact the sample surface [22-23]. Given the very high strains and strain rates at relatively low temperatures, the SMAT process exposes the surface of the material to severe plastic deformation, leading to the formation of ultrafine-grained or nanostructured surfaces [24-25].

The numerical model of the SMAT process is quite complex, as it involves the dynamic analysis of rapidly moving impacting balls on a metal target, which itself may have a complex geometry. Since SMAT involves random, high-velocity impacts of spherical shots, FEA helps to predict the mechanical effects, such as plastic deformation, residual stress distribution, grain refinement zones, and hardness gradients.

In this study, the target material is AZ31 magnesium alloy. Magnesium, due to its low density and favorable chemical and mechanical properties, has various alloy compositions with numerous industrial applications. AZ31 is a magnesium alloy containing 3 weight percent aluminum (Al) and 1 weight percent zinc (Zn) [26-27]. "Table 1" shows the composition of AZ31 material as a magnesium alloy.

Table 1 The weight percentages (wt%) of the AZ31.

Element	Mg	Ni	Mn	Zn	Al
Composition	Bal.	0.03	0.25	0.71	3.1

To achieve the research objectives, the finite element software ABAQUS is used for simulations. In this study, as shown in "Fig.1", three components are modeled in ABAQUS as: 1) a circular plate with a diameter of 21 mm and a thickness of 3 mm, 2) a vibration chamber modeled as a closed and hollow cylinder with a diameter of 22 mm, and 3) balls with three different diameters (all dimensions are based on real samples). A total of 12 balls are placed on the vibrating platform to cover the underside of the vibration chamber.

In real conditions, stainless steel balls are used for the SMAT process, and the mechanical properties of AZ31 plate are much weaker than steel. Therefore, in finite element simulation, to reduce simulation time, both the vibration chamber and the balls are defined as rigid materials. In contrast, the plate is defined as deformable, as the focus is on analyzing the plate.

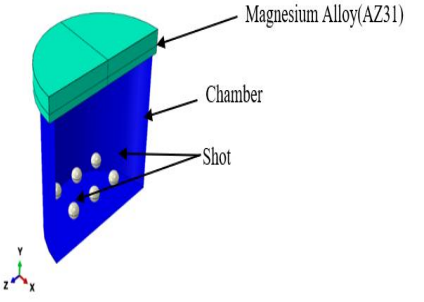

Fig. 1 Simulation display of the assembly: vibrating platform, target material (AZ31), and balls.

"Table 2" shows the parameter values used in the finite element simulation of the structure, including the geometric and mechanical properties of the AZ31 plate and stainless-steel balls. These parameters were defined in the ABAQUS software toolboxes. The mechanical properties of the AZ31 are reported in "Table 3". To determine the yield stress of the material, an experimental tensile test was conducted, and the engineering stress-strain results were extracted in Excel format. The plastic behavior of the material was defined using the true stress-strain curve. Additionally, the material was modeled as homogeneous and isotropic.

Table 2 The parameter values and geometric and mechanical properties of the 3D FEA simulated model

Parameter	Value
Simulation Time	10 milliseconds
Sheet Size (Target material)	Diameter: 21(mm), Thickness: 3(mm)
Ball Speeds	4 m/s, 8 m/s, 10 m/s
Ball Diameters	1mm, 2mm, 3mm
Ball Property	Density: 7800 (kg/m^3)
Target Material (AZ31) Properties	Density: 1770 (kg/m^3) Young's Modulus: 45 (GPa) Poisson's Ratio: 0.3

Table 3 Mechanical properties of AZ31 magnesium alloy used in modeling

Parameter	Value
Young's Modulus	45 (GPa)
Yield Strength	285 (MPa)
Tensile Strength	313 (MPa)
Elongation (%)	18%

Given the transfer of kinetic energy through the vibrating platform at the bottom of the SMAT chamber, it can be inferred that the shots move along a directed path with an impact angle very close to 90 degrees, and negligible interactions between the shots can be ignored. The shot impact velocity was estimated by finite element modeling of 1, 2, and 3 mm shots within a cylindrical chamber representing the device's chamber. The actual dimensions of the chamber were considered in the modeling. As shown in "Fig. 2", in the SMAT device, the vibrational signal generated by the ultrasonic generator is in the form of a harmonic sine function, which was modeled as a boundary condition using Equation (1):

$$x(t) = A \sin \omega t \quad (1)$$

Impact Conditions are performed as follows:

- Impact angle: Often normal (90°) for simplicity, but can vary.
- Single or multiple sequential impacts simulated.
- Dynamic, explicit time integration is usually necessary (due to high-speed impact).

ABAQUS/Explicit was used for the 3D Finite Element Simulation of the process. Several outputs, such as Residual stress distribution (depth & magnitude), Plastic strain distribution, and Equivalent von Mises stress, were obtained. Fine mesh was used near the impact area for accuracy, and a Coarser mesh away from the impact zone to reduce computational cost. The Path-FE method was used to extract the residual stresses along a predefined path (vertical from the impact point into the depth of the substrate). This path was selected through the center of the impact zone in the 3D model. After the simulation completes, the residual stress is extracted node-by-node along this path. The principal stresses, also known as von Mises stresses, were plotted against depth. No additional sub-modeling or cell division was needed.

The contact between the sheet surface and the balls was defined using a penalty contact method (frictional contact). The coefficient of friction between the sheet and the balls was set to μ=0.1, with hard contact behavior used in the vertical direction. To investigate the effect of the element size, a sensitivity analysis was performed. The simulation process was carried out using a mesh of elements with a size of 0.25 mm to determine the maximum residual stress induced in the sheet. According to experimental testing in the SMAT process, the chamber floor oscillates based on Equation (1). Ultrasonic vibration was defined as a harmonic sine function for the vibration chamber. In the simulation, vibration was initially applied to the platform so that the balls would impact the sheet and induce stress on it. In the subsequent stage, vibration and loading were removed to allow for the measurement of residual stresses in the free body.

To study the effects of speed and ball size on the SMAT process, two test scenarios were considered. The investigation includes three different speeds (4, 8, and 10 m/s) and three ball sizes (1, 2, and 3 millimeters in diameter) according to SAE J444 standards. The analysis and boundary conditions are entered into specific parts of the ABAQUS software. After inputting all the parameters into the software, the analysis and evaluation of the results are performed.

3 RESULTS AND DISCUSSION

In this study, the effects of diameter and speed on residual compressive stress, depth of residual compressive stress, and maximum equivalent plastic strain were investigated in SMAT process. The analysis was performed through finite element simulations, and the results are presented in "Table 4".

Table 4 Characteristics of the samples and main results of finite element models

Case Study No.	Ball Diameter (mm)	speed (m/s)	Maximum compressive Residual Stress (MPa)	Maximum Equivalent Plastic Strain
1	1	4	-155	0.064
2	1	8	-166	0.073
3	1	10	-202	0.079
4	2	4	-173	0.065
5	2	8	-182	0.073
6	2	10	-203	0.080
7	3	4	-176	0.066
8	3	8	-190	0.073
9	3	10	-205	0.080

As shown in "Table 4", residual stresses in two conditions and nine models were examined. After performing the simulation and analysis with ABAQUS, the outputs, including stress histories (Smises, Smax, Smin) and equivalent plastic strain (PEEQ) in different directions, as well as the thickness of the sheet sample for all time steps during the defined process duration, were obtained. Figure 2 displays the deformed sample, the graphical distribution of stress, equivalent plastic strain, and displacement.

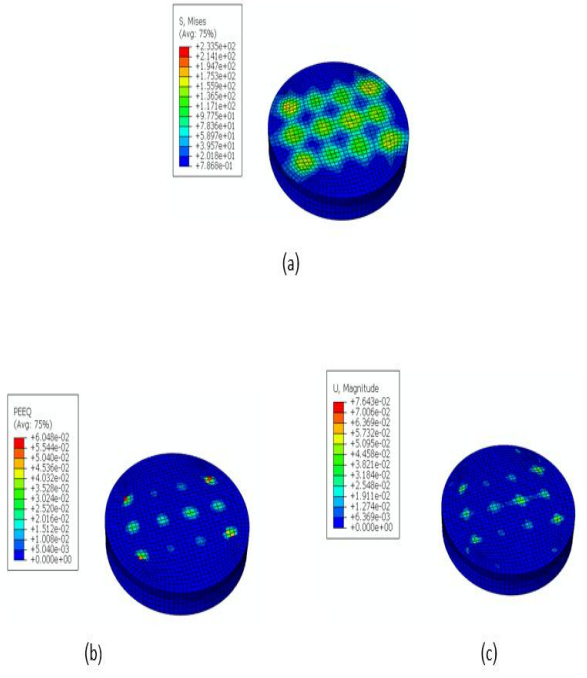

Fig. 2 Results from the simulation, a) distribution of von Mises stress, b) distribution of equivalent plastic strain, c) displacement.

The process involves numerous parameters that need to be controlled to achieve a suitable residual stress distribution on the workpiece. Therefore, the effect of ball diameter and speed on residual stress distribution (Section 4-1) and the effect of ball diameter and speed on equivalent plastic strain (Section 4-2) will be examined.

3.1. Influence of Ball Diameter and Speed on Compressive Residual Stress

3.1.1. Effect of Ball Diameter on Residual Stress

To investigate the effect of ball diameter on the residual stress curve, three different diameters, 1mm, 2 mm, and 3 mm, are considered. The impact speed is set at 4 m/s. Figure 3 shows the residual stress distribution along the depth of the compacted layer in the direction of the impact. It can be observed that the maximum absolute residual stress is 155 MPa, 173 MPa, and 176 MPa, respectively, for the different ball diameters 1, 2 and 3mm. The differences between the results for the various ball diameters are relatively close.

As the ball diameter increases, the maximum compressive residual stress gradually increases, while the depth affected by the residual stress shows a significant increase. The results of this study are in good agreement with the research conducted by Meguid and colleagues [6]. In another study, Meguid et al. [28] examined the influence of speed, size, shape, and number of balls in the shot-peening process on a metal workpiece. The results showed that with an increase in ball speed, the stress applied to the subsurface increases, and the stress penetrates deeper layers. This study demonstrates that each particle's impact on the workpiece increases the applied surface stress in the simulation. Additionally, the size of the particles has a direct relationship with the intensity of the stress applied to the surface of the workpiece and with the depth of stress penetration, such that as the ball diameter increases, the depth of stress penetration also increases.

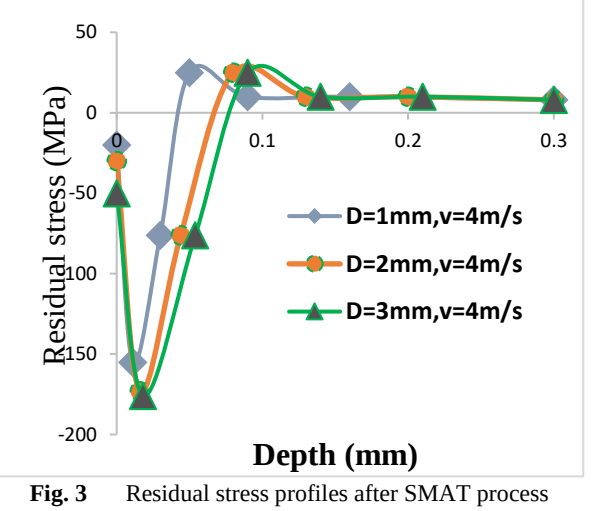

Fig. 3 Residual stress profiles after SMAT process (diameters: 1, 2, and 3 mm at 4 m/s speed).

3.1.2. Effect of Ball Speed on Residual Stress of The Target Material

Figure 4 illustrates the residual stress distribution along the depth of the compacted layer in the direction of impact for different diameters and speeds. As the speed increases, the depth of the compressive residual stress zone slightly increases. The impact speed significantly affects the surface stress and the maximum subsurface stress. It is observed that increasing the speed from 4 m/s to 10 m/s for a 1 mm diameter ball increases the compressive residual stress from 155 MPa to 205MPa. This increase could be related to greater work hardening resulting from the higher impact force at greater speeds. The results indicate that increasing ball speed has a more significant impact on compressive residual stress compared to increasing ball diameter. As one moves towards the depth of the sample, it is evident that with the increase in impact speed, the depth of the plastic zone and compressive stress on the surface, along with the maximum residual stress at depth, will increase.

The increase in the maximum compressive residual stress and the depth of the compacted layer due to higher ball speed is more noticeable than that due to ball diameter.

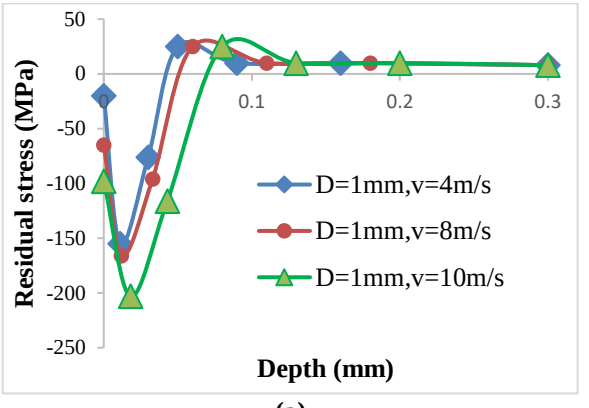

(a)

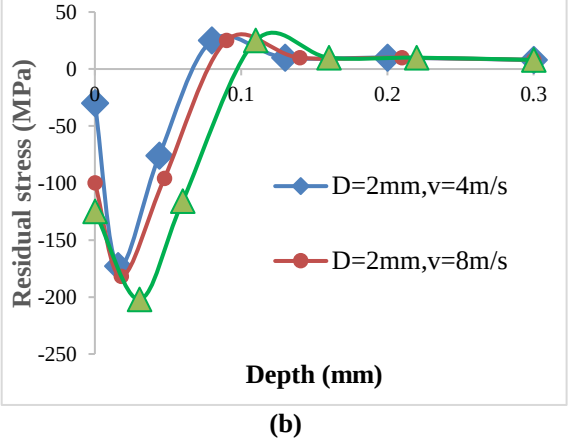

(b)

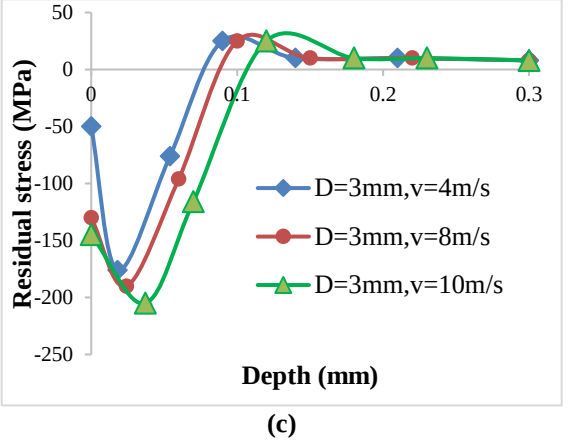

(c)

Fig. 4 Residual stress profiles after SMAT Process at various speeds for ball diameters: (a): 1mm, (b): 2mm, and (c): 3mm.

The trend of results of this study are in agreement with the research conducted by Majzoobi et al. [16]. They used LS-DYNA finite element simulation to examine the impact of several balls (9, 13, and 25 in number) arranged in different configurations at various speeds ranging from 50 to 100 m/s. They observed that the maximum compressive residual stress occurred when 25 balls impacted at a speed of 90 m/s, reaching a value of up to 1100 MPa. They demonstrated that ball speed significantly influences the maximum compressive residual stress.

3.2. Influence of Ball Diameter and Speed on Equivalent Plastic Strain

4.2.1. Effect of Ball Diameter on Equivalent Plastic Strain

Equivalent plastic strain is a key parameter for surface densification and grain boundary production [29-30]. Figure 5 shows the plastic strain profile in the depth of the compressed layer along the impact direction for different ball diameters (1, 2, and 3 mm) at a speed of 4 m/s. The ball size significantly affects the depth of the affected area where plastic deformation occurs, but it has a minimal impact on the maximum equivalent plastic strain. As the ball diameter increases from 1 mm to 3 mm, the maximum plastic strain changes from 0.06 to about 0.07. This result aligns well with the study by Yarar et al.[18], who investigated the multiple ball impacts due to the SMAT process in aluminum alloy 7075 to achieve maximum equivalent stress, equivalent plastic strain, residual stress depth, and maximum compressive residual stress. It was observed that ball size is not as influential as ball speed on maximum equivalent stress. The findings indicate that increasing ball diameter and speed leads to an increase in residual stress, showing a similar and incremental trend, consistent with the results of this study and the dynamic finite element analysis on single-impact plastic deformation behavior in aluminum alloy 7075 as presented in reference [18].

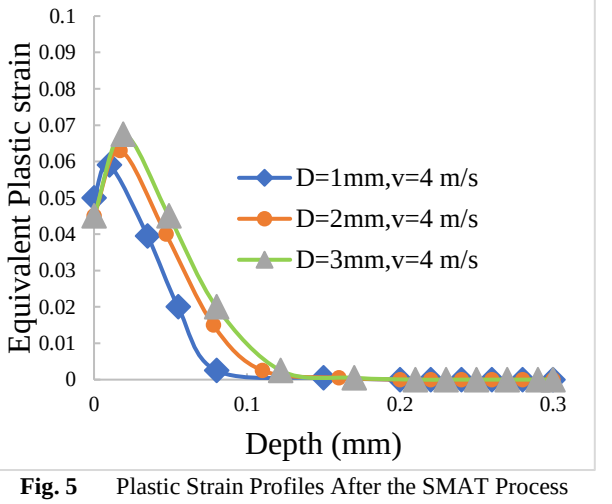

Fig. 5 Plastic Strain Profiles After the SMAT Process (Diameters of 1, 2, and 3 mm at a Speed of 4 m/s).

3.2.2. Effect of Ball Speed on Effective Plastic Strain

Figure 6 shows the equivalent plastic strain profiles for a 1 mm diameter shot at speeds of 4, 8, and 10 m/s along the depth.

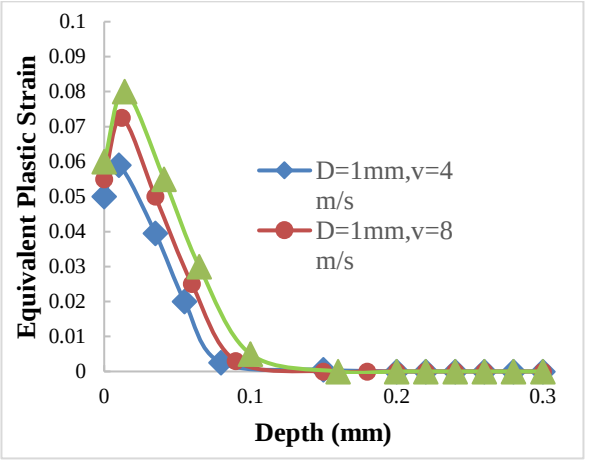

Fig. 6 Profile of equivalent plastic strains after the SMAT process for ball diameters of 1 mm at various speeds.

It can be observed that as the speed increases from 4 m/s to 10 m/s for a 1 mm diameter shot, the equivalent plastic strain on the surface increases from 0.05 to 0.06. The depth of target material, affected by plastic deformation, increases as the ball speed increases. It can be concluded that, generally, an increase in shot speed will significantly influence the depth of effective plastic strain.

The phenomenon of work hardening is another benefit of SMAT, which is due to the localized plastic deformation in the target material caused by the impact of the shots. These impacts and plastic strains reduce grain size and increase the dislocation density on the surface. Consequently, these locked dislocations cause the work hardening of the part. Therefore, with the increasing speed of shot particles and reduced microstructure, it can be concluded that the yield strength and material hardness can increase according to the Hall-Petch theory. The Equations of the Hall-Petch theory are as below:

$$\sigma_y = \sigma_0 + kd^{-\frac{1}{2}} \tag{2}$$

$$H = H_0 + kd^{-\frac{1}{2}} \tag{3}$$

In these Equations, σ_y represents the yield stress, σ_0 is the material's constant for the starting stress for dislocation movement, d is the grain diameter, and k is a constant related to the influence of grain boundaries on dislocation movement. In this Equation, H denotes the material hardness, H_0 is the hardness constant of the Equation, d is the grain diameter, and k is another constant. As the grains become smaller, the material's strength and hardness increase because the number of grain boundaries rises. These boundaries act as obstacles to dislocation movement, thereby enhancing the material's strength. Further increases in dislocation density behind the grain boundaries lead to greater work hardening, contributing to additional strengthening mechanisms and increased material strength.

4.3. Effect of Speed on Displacement in The Depth of The Target Material

Figure 7 shows the amount of displacement caused by indentations for a particle with a diameter of 2 mm at speeds of 4, 8, and 10 m/s. According to the Figure, it is clear that the amount of displacement at the surface of the material is the highest. The amount of displacement has increased with increasing impact velocity, such that the maximum amount of displacement is related to the velocity of 10 meters per second with a magnitude of 0.06 mm. At all three speeds, the amount of displacement has decreased with a similar pattern as it moves into depth. Creating displacement at the surface increases the density of the dislocations and increases the strength of the surface in the SMAT process.

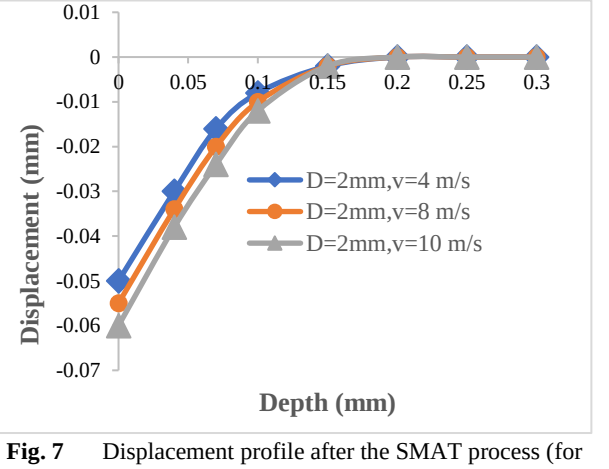

Fig. 7 Displacement profile after the SMAT process (for ball diameter 2 mm at speeds of 4, 8, and 10 m/s).

4 CONCLUSIONS

The effects of steel ball impacts on changes in compressive residual stresses and effective plastic strain in AZ31 magnesium alloy were analyzed using dynamic finite element methods with explicit integration, and evaluated using ABAQUS. The results obtained from this study are as follows:

1. Effect of ball diameter and speed: Increasing the ball diameter and speed has a positive impact on increasing the residual stress and plastic strain values of the material. However, the effect of increasing ball speed on maximum compressive residual stress is greater than the effect of increasing the ball diameter. This is due to the squared effect of speed on translational kinetic energy ($E = 1/2mv^2$), as the impact of speed on kinetic energy is more significant than mass.
2. Compressive residual stress trends: The maximum compressive residual stress increases from

155MPa to 176MPa when the ball diameter is increased from 1 to 3mm at a speed of 4 m/s. Increasing the speed from 4 to 10m/s, for 1 mm ball diameter, raises the maximum compressive residual stress from 155 MPa to 202 MPa. It can be concluded that increasing the diameter from 1 to 3mm has increased the amount of residual stress by up to 13%, while increasing the speed from 4 to 10m/s has increased the amount of residual stress by up to 30%.

3. Impact of SMAT process: The surface residual stress, maximum compressive residual stress, and depth of residual stress penetration, which indicate the effectiveness of the SMAT process, increase with the ball diameter and speed.

4. Improvement of Alloy Properties: The impacts and plastic strains reduce grain size and increase the dislocation density on the surface. Increasing the speed of shot particles and reducing microstructure size increase the material strength and surface hardness. The highest increase in strength can be achieved with a 3 mm diameter ball at a speed of 10 m/s.

5. Optimal conditions: The highest surface residual stress and maximum compressive residual stress are achieved with a 3 mm diameter ball at a speed of 10 m/s. The effect of ball speed on maximum compressive residual stress and depth of penetration is greater than the effect of ball diameter. This is because maximum compressive residual stress is controlled by the material's yield strength, while deformation depth is controlled by plastic strain and strain. As the dynamic stresses from the ball impact the target material, changes in maximum compressive residual stress below the surface decrease.

REFERENCES

[1] Lu, K., J. Lu, Nanostructured Surface Layer on Metallic Materials Induced by Surface Mechanical Attrition Treatment, Materials Science and Engineering: A, Vol. 375, 2004, pp. 38–45.

[2] Liu, G., Lu, J., and Lu, K., Surface Nanocrystallization of 316l Stainless Steel Induced By Ultrasonic Shot Peening, Materials Science and Engineering: A, Vol. 286, No. 1, 2000, pp. 91–95.

[3] Al-Obaid, Y., The Use of Shot Peening Technology In an Aircraft Industry, Third Conf. on Aeronautical Sciences and Aviation Technology, 1989, pp. 4–6.

[4] Shaw, M. C., DeSalvo, G. J., On the Plastic Flow Beneath A Blunt Axisymmetric Indenter, Vol. 92. 1970, pp. 450.

[5] Zhang, X., Lu, J., and Shi, S., A Computational Study of Plastic Deformation in AISI 304 Induced By Surface Mechanical Attrition Treatment, Mechanics of Advanced Materials and Structures, Vol. 18, No. 8, 2011, pp. 572–577.

[6] Meguid, S., Shagal, G., and Stranart, J., 3D FE Analysis of Peening of Strain-Rate Sensitive Materials Using Multiple Impingement Model, International Journal of Impact Engineering, Vol. 27, No. 2, 2002, pp. 119–134.

[7] Todaka, Y., Umemoto, M., and Tsuchiya, K., Comparison of Nanocrystalline Surface Layer in Steels Formed by Air Blast and Ultrasonic Shot Peening, Materials Transactions, Vol. 45, No. 2, 2004, pp. 376–379.

[8] Chaise, T., and et al., Modelling of Multiple Impacts for The Prediction of Distortions and Residual Stresses Induced by Ultrasonic Shot Peening (USP), Journal of Materials Processing Technology, Vol. 212, No. 10, 2012, pp. 2080–2090.

[9] Astaraee, A. H., et al., Incorporating the Principles of Shot Peening for A Better Understanding of Surface Mechanical Attrition Treatment (SMAT) by Simulations and Experiments, Materials & Design, Vol. 116, 2017, pp. 365–373.

[10] Yin, F., and et al., Numerical Modelling and Experimental Approach for Surface Morphology Evaluation During Ultrasonic Shot Peening, Computational Materials Science, Vol. 92, 2014, pp. 28–35.

[11] Manchoul, S., and et al., A Predictive Approach to Investigate the Effect of Ultrasonic Shot Peening on A High-Cycle Fatigue Performance of an AISI 316L target, The International Journal of Advanced Manufacturing Technology, Vol. 95, No. 9, 2018, pp. 3437–3451.

[12] Meng, X., and et al., The Deformation Behavior of AZ31 Mg Alloy With Surface Mechanical Attrition Treatment, Materials Science and Engineering: A, Vol. 707, 2017, pp. 636–646.

[13] Zhang, H., and et al., Formation of Nanostructured Surface Layer on AISI 304 Stainless Steel by Means of Surface Mechanical Attrition Treatment, Acta Materialia, Vol. 51, No. 7, 2003, pp. 1871–1881.

[14] Bagherifard, S., and et al., Experimental and Numerical Analysis of Fatigue Properties Improvement in A Titanium Alloy by Shot Peening, Engineering Systems Design and Analysis, Vol. 49163, 2010, pp. 317–322.

[15] Anand Kumar, S., Ganesh Sundara Raman, S., and Sankara Narayanan, T., Effect of Surface Mechanical Attrition Treatment on Fatigue Lives of Alloy 718, Transactions of the Indian Institute of Metals, Vol. 65, No. 5, 2012, pp. 473–477.

[16] Majzoobi, G., Azizi, R., and Nia, A. A., A Three-Dimensional Simulation of Shot Peening Process Using Multiple Shot Impacts, Journal of Materials Processing Technology, Vol. 164, 2005, pp. 1226–1234.

[17] Liu, Y., Lv, S. L., and Zhang. W., Shot Peening Numerical Simulation of Aircraft Aluminum Alloy Structure, IOP Conference Series: Materials Science and Engineering, Vol. 322, 2018, pp. 032003.

[18] Yarar, E., Erturk, A. T., and Karabay, S., Dynamic Finite Element Analysis on Single Impact Plastic Deformation Behavior Induced by SMAT Process in 7075-T6 Aluminum Alloy, Metals and Materials International, Vol. 27, No. 8, 2021, pp. 2600–2613.

[19] Cao, L.J., Li, S. J., and Shangguan, Z. C., Numerical Simulation of Residual Stresses Induced from Shot Peening with Finite Element Method, Applied Mechanics and Materials, Vol. 433, 2013, pp. 1898–1901.

[20] Hong, T., Ooi, J., and Shaw, B., A Numerical Simulation to Relate the Shot Peening Parameters to the Induced Residual Stresses, Engineering Failure Analysis, Vol. 15, No. 8, 2008, pp. 1097–1110.

[21] Xiao, X., and et al., Prediction of Shot Peen Forming Effects with Single and Repeated Impacts, International Journal of Mechanical Sciences, Vol. 137, 2018, pp. 182–194.

[22] Lei, W., and et al., Effect of Nanocrystalline Surface and Iron-Containing Layer Obtained by SMAT on Tribological Properties of 2024 Al Alloy, Rare Metal Materials and Engineering, Vol. 44, No. 6, 2015, pp. 1320–1325.

[23] Chen, G., and et al., Effects of Strain Rate on The Low Cycle Fatigue Behavior of AZ31B Magnesium Alloy Processed by SMAT, Journal of Alloys and Compounds, Vol. 735, 2018, pp. 536–546.

[24] Peng, J., and et al., The Effect of Surface Mechanical Attrition Treatment on Texture Evolution and Mechanical Properties of AZ31 Magnesium Alloy, Materials Characterization, Vol. 148, 2019, pp. 26–34.

[25] Tomczak, J., Pater, Z, and Bulzak, T., Thermo-Mechanical Analysis of A Lever Preform Forming from Magnesium Alloy AZ31, Archives of Metallurgy and Materials, Vol. 57, No. 4, 2012, pp. 1211–1218.

[26] Hou, X., and et al., A Systematic Study of Mechanical Properties, Corrosion Behavior And Biocompatibility of AZ31B Mg Alloy After Ultrasonic Nanocrystal Surface Modification, Materials Science and Engineering: C, Vol. 78, 2017, pp. 1061–1071.

[27] Mukai, T., and et al., Ductility Enhancement in AZ31 Magnesium Alloy by Controlling Its Grain Structure, Scripta Materialia, Vol. 45, No. 1, 2001, pp. 89–94.

[28] Meguid, S., and et al., Three-Dimensional Dynamic Finite Element Analysis of Shot-Peening Induced Residual Stresses,Finite Elements in Analysis and Design, Vol. 31, No. 3, 1999, pp. 179–191.

[29] Kumar, S., Chattopadhyay, K., and Singh, V., Effect of Ultrasonic Shot Peening on LCF Behavior of the Ti–6Al–4V Alloy, Journal of Alloys and Compounds, Vol. 724, 2017, pp. 187–197.

[30] Bagherifard, S., Ghelichi, R., and Guagliano, M., Mesh Sensitivity Assessment of Shot Peening Finite Element Simulation Aimed at Surface Grain Refinement, Surface and Coatings Technology, Vol. 243, 2014, pp. 58–64.

Int. J. Advanced Design and Manufacturing Technology, 2025, Vol. 18, No. 4, pp. 11-24

DOI: *ISSN: 2252-0406* *https://admt.isfahan.iau.ir*

A New Method for Generating Trading Signals in Financial Markets by a Combination of Deep Learning and Reinforcement Learning

Ahang Golabi, Mojtaba Salehi *, Hossein Nahid Titkanloo

Department of Industrial Engineering
Payame Noor University, Tehran, Iran
E-mail: ahang.golabi@pnu.ac.ir, Mojtaba.salehi@pnu.ac.ir, Hossein_Nahid@pnu.ac.ir
*Corresponding author

Received: 20 May 2025, Revised: 29 June 2025, Accepted: 5 August 2025

Abstract: The present study offers a new approach for identifying trading signals in the financial market using machine learning techniques. It employs graphical and correlational research methods, utilizing support learning techniques in MATLAB to test hypotheses. The study proposes an automated trading system combining reinforcement learning and deep learning to determine trade signals and position sizes. The framework combines an LSTM network with Q-learning, an out-of-policy reinforcement learning algorithm. Q-learning aims to maximize overall reward by learning from actions deviating from the existing policy. Our study introduces a new framework that utilizes the collective intelligence of multiple expert traders to learn across different time frames. It shows that using Fundamental and technical indicators independently or in combination to train LSTMs for predicting currency movements in Forex significantly improves prediction accuracy. The study introduces a third class to represent small changes in currency pair prices between two consecutive days, improving prediction accuracy. It also describes a new method for determining the most suitable threshold value to define the unchanged class. Additionally, the study trains LSTMs to predict values k days into the future, and searches for the influence of varying training iterations on accuracy values.

Keywords: Financial Market, Machine Learning, Trading Signals

Biographical notes: Ahang Golabi received her BSc in Industrial Engineering from Azad University of Sanandaj. She received her MSc in Information Technology Management from Payame Noor University and is currently a PhD candidate in industrial engineering at this university. **Mojtaba Salehi** received his PhD in Industrial Engineering from Tarbiat Modares University. He is currently an Assistant professor at Payame Noor University. His field of research is mainly Financial Engineering, System dynamics, Machine Learning & Data Mining and Applied Operation Research. **Hossein Nahid Titkanloo** received his PhD in Industrial Engineering from the Payame Noor University. Also, he is currently an Assistant Professor at Payame Noor University. His field of research is mainly industrial engineering, artificial intelligence and System Analysis.

Research paper

1 INTRODUCTION

Stock prices fluctuate daily due to various factors, including politics. This unpredictability complicates trading strategies for buying or selling stocks. Stock market analysis focuses on optimizing portfolios [1], identifying investment strategies [2], and assessing risks [3]. Forecasting stock price trends has attracted interest from various fields, including economics, finance, statistics, and machine learning [4-6].

Financial trading has been extensively studied, leading to the development of various methods. These approaches are classified into two classes: modern and traditional. Traditional ones are technical [2] and fundamental analysis [3]. Modern trading methods include algorithmic trading [4] and machine learning (ML) [3]. Abundant data, limitations of traditional methods, and the complicated nature of financial markets emphasize the need for strategies like algorithmic trading.

Studies have proposed algorithms for anticipating stock movements using machine learning (ML) techniques like support vector machines (SVM) and artificial neural networks (ANN) [5-8]. Researchers are using deep learning approaches like LSTM and RNN [9-10] for predicting stock prices. They also use trading algorithms to maximize profits [3]. Algorithmic trading can use rule-based strategies or ML approaches. Rule-based strategies are derived from traditional or mathematical models, while ML-based trading involves training computers on historical data to operate autonomously. This method offers several advantages over traditional trading.

Algorithmic trading, which utilises machine learning, offers advantages over rule-based trading. ML-based algorithms have the capability of extracting information and patterns from historical data without predefined rules. Additionally, ML-based trading can generate insights and support decision-making through algorithms like reinforcement learning and Q-learning [11].

In a study [12], researchers used reinforcement learning to optimize securities and stock exchanges. DeepMind mastered seven Atari video games, reaching human expert level in three, and eventually achieved expert-level performance in more than 20 different Atari games [13].

Machine learning (ML) has attracted considerable interest from scholars, which has led to the development of various algorithms for extracting information from different types of data. Initially, most ML algorithms were confined to prediction.

Machine learning algorithms, like deep reinforcement learning (DRL), are able to provide optimal decisions independently in complicated settings, such as financial markets. It has made ML a captivating study area in finance. DRL has shown significant achievement in solving complicated sequential decision-making problems. Research in Reinforcement Learning (RL) focuses on multi-agent frameworks, which are used in various fields. Fewer studies have examined multi-agent RL [14], especially in financial trading [15].

The Fractal Market Hypothesis (FMH), introduced by Peters, offers a substitute for the generally recognized efficient market theory. FMH suggests that market price behaviour is not random, as assumed in EMH, but instead exhibits a fractal characteristic with a comparable framework across various time intervals. It describes market behaviour with chaos, fractals, breakdowns, and crises. The Elliott wave theory [13] suggests that price has repetitive behavior across different time frames, with markets following repetitive cycles based on collective trading behavior.

Several studies suggest that the market's fractal nature may be attributed to traders' intuition, which involves varying data interpretations and investment horizons [15]. Financial markets exhibit unique characteristics within specific time frames. According to the Fractal Market Hypothesis (FMH), there may be interrelationships between different periods due to varying interpretations of information. The system is made using an LSTM network integrated with Q-learning, an RL algorithm that operates outside the policy to identify the optimal action based on the present conditions.

The Q-learning algorithm operates outside the current policy and seeks to maximize total reward. Our framework is built upon a deep Q network. Analysts have used various machine learning methods for stock showcase determination [15-19]. Deep learning models are gaining popularity in financial trading [20-22]. Ding et al. [23] presented a deep convolutional neural network for predicting stock prices.

In RL, the agent learns to link states with actions in order to maximize rewards [29]. The agent tracks state information from its environment and autonomously learns to choose actions based on the reward it receives and the current state [14].

The use of DRL strategies has obtained popularity in various trading methods [36-37] and has been assessed for their effectiveness in stock markets [38]. A suggested three-layer multi-group strategy outperformed a traditional buy-and-hold approach [39]. Our work employs this approach as a benchmark.

2 BACKGROUND OF THE RESEARCH

Touché and Safel [12] presented Repetitive Reinforcement Learning (RRL), a coordinated reinforcement method with a better performance compared to Q-learning. This RRL agent employs a

single-layer neural network for maximizing a risk-adjusted return function based on previous returns and yield. Dorson et al. [31] employed RRL and Q-learning strategies to optimise investment strategies, integrating reinforcement learning with a trading system. They demonstrated a solid execution of the Q-learning.

In a specific data setup, the results outperformed the buy-and-hold strategy by a factor of two. Nomiwaka et al. [32] conducted an extensive experimental use of RL to solve the optimal execution problem by large-scale NASDAQ market microstructure data bases. These authors utilized historical records from INET and performed tests on three stocks - Qualcomm (QCOM), NVIDIA (NVDA), and Amazon (AMZN). The results demonstrated that RL outperformed the send-and-leave (S&L) strategy previously used in a basic market. Additionally, [33] applied adaptive reinforcement learning (ARL) in the financial market. They integrated a dynamic hyperparameter optimization layer and a risk management layer and examined the framework using two years of real EUR/USD data (January 2000 - January 2002), with 1-minute granularity, and achieved an average annualized return of 26%. Li et al. [34] presented a novel stock trading framework according to RL. The proposed system, MQ-trader, comprises four collaborative Q-learning agents.

Cumming et al. [35] used an LSTD-based RL algorithm (Reinforcement Learning Algorithm based on Least Squares Temporal Difference) to achieve an annual profit of 1.64% in the EUR/USD market. Akita et al. [24] found that combining textual and numerical data is more effective for predicting stock prices. [25] suggested an LSTM-based model by the use of technical indicators and historical price measures for anticipating stock price movements. [26] developed the ATT-ERNN model for anticipating stock price movements based on global events, using a two-stage attention-based recurrent neural network. Zhao et al. [28] used a market-aware framework to predict stock returns by combining fundamental and technical indicators. Caesar and Ozbayoglou [41] used technical analysis indicators and stock price data to label images for a CNN model.

In their research, Wen and Yuan [42] used a hybrid LSTM-CNN model to analyze data, incorporating various inputs such as Sunspot data, technical analysis indicators, fundamental analysis information, and economic indicators. According to their findings, the hybrid model showed better performance compared to individual CNN and LSTM models, particularly in terms of parameters such as Score-F1. Kim and Kim [43] also employed a combined CNN-LSTM model to predict S&P 500 share prices, outperforming individual LSTM and CNN methods. Additionally, Caesar et al. [44] utilized a different approach to predict buy, sell, and hold signals, concluding that their method showed higher effectiveness compared to the buy-and-hold approach. In their study, Ghorbani et al. [45] used a combined colored Petri nets strategy and genetic algorithm for simulating and forecasting buy/sell signals of stock exchanges. They found this method to be more effective in generating correct signals in comparison with other techniques, like neural networks, decision trees, and linear regression. Melki et al. [46] focused on efficiently summarizing and visualizing stock market information due to the large amount of data generated in the Tehran stock market. They used the incremental clustering method along with the k-means algorithm to identify stock movement signals. Chen et al. [47] concentrated on predicting stock trading signals, emphasizing the unstable and complex nature of stock market impacted by various interconnected variables.

In another study, Li et al. [48] discuss the challenges of algorithmic trading, proposing the TFJ-DRL model, which combines RL and deep learning for financial decision-making improvement.

Singh et al. (2022) discuss how the accessibility of information has transformed financial frameworks. They highlight how modern reinforcement learning can improve decision-making in complex financial scenarios. Gororge et al. [47] compared linear regression and SVM for stock price forecasting, aiming to demonstrate the advantages of SVM over linear regression.

3 RESEARCH METHODOLOGY

The descriptive and correlational research strategy aims to illustrate and understand existing conditions and relationships between factors using historical data. It examines cause and effect, identifies dependent and independent variables, and utilizes tools such as surveys, interviews, observations, tests, vouchers, and analysis for data collection.

This study uses a library strategy to collect specific data on the forex market from 2018 to 2021. Machine learning techniques in Python or MATLAB are applied for data analysis focusing on reinforcement learning (RL) to generate trading signals that maximize overall profit using the Q-learning algorithm in the stock market.

4 RESEARCH FRAMEWORK

An RL system comprises four major constituents: a value function, a reward signal, a policy, and, optionally, an environment model. The agent has interaction with the environment in discrete time steps, $t = 0, 1, 2, 3$, receiving information about the environment state at t time steps.

$st \in S$, where S denotes a set of possible states, and therefore an action is chosen.

An action, denoted as '∈ A(st)', belongs to the set of actions present in state 'st'.
After taking a step, the agent obtains a numerical reward, rt+1 ∈ ℝ, entering a new state, st+1.
The agent maps states to the probabilities of selecting different activities, known as the agent's approach (πt). The likelihood of choosing action a (at) when in state s (st) is represented by πt(s, a). An LSTM cell can retain and recall past data for an extended period. It includes an output gate, an input gate, and a forget gate, each of which holds values between 0 and 1. A value of 1 means to retain the data, and 0 means to discard it. The input gate determines which portions of the input data are added to the cell's content and to what degree. The forget gate makes a decision on which parts of the cell's content are removed. The output gate regulates which portions of the cell's content are included in the hidden state.

5 DISCOVERIES

The current work aims at predicting a specific exchange rate's medium-term trend by analyzing relationships among various exchange rates. We focused on cross-currency trades that reveal arbitrage opportunities in the forex market, exploiting short-term price differences between a currency and its associated currencies.
Triangular arbitrage involves three currencies, where one is derived from the exchange rates of the other two. This study focuses on the cross rates of GBP/USD, EUR/GBP, and EUR/USD, using EUR/USD as the base currency. In the foreign exchange market, the EUR/USD cross rate should be calculated based on the EUR/GBP and GBP/USD pairs. “Eq. (1)”:

$$Er=reur/usd=reue/gbp.rgbp/usd \quad (1)$$

In connection (1), we mentioned the exchange rate as Er. To prevent arbitrage in regulated financial markets, a precise timing ratio for currency transactions is necessary. Short-term discrepancies in forex markets create trading opportunities for financial advisors. Analyzing features on a forex time series chart can reveal early differences in currency prices.
We analyze related currencies using triangular arbitrage to assess the medium-term direction of a currency. By using EUR/USD as the base currency alongside EUR/GBP and GBP/USD, we identify potential arbitrage opportunities. It is possible to apply this approach to other currencies with comparable monetary properties.
Profit function: To calculate efficiency and profit, if the price at time "t" is denoted as "pt", then the profit function is as follows, “Eq. (2)”:

$$Rit=\log(pit/pit-1)*100 \quad (2)$$

Function (2) is positive when the logarithm of the upper face of the number is 100.
Loss function, “Eq. (3)”:

$$CE = -\sum_{I=1}^{C=2} T_I \, LOG(S_I) = -t1\log(s1) - (1 - t1)\log(1 - s1) \quad (3)$$

In this scenario, there are two targets, labeled as 1C and 2C. The values (t0, t1) and S1 represent the actual label and output score of the network for target 1C, respectively.
Furthermore, 1 - t1 = 2t and 1 - S1 = 2S represent the actual label and output of the network for target 2C, respectively.

Inputs:
The dataset comprises values for the 2018-2021 period, with 1,325 data points during market hours. The EUR/USD ratio saw an increase of 680 and a decrease of 645 over this span.
Entry and exit signal:
The initial trading strategy involves using the stochastic oscillator.
This strategy involves using a version of stochastic volatility to generate buy and sell signals to enter and close trades.
Second trading strategy (mean reversion):
The average reversion strategy, which includes Bollinger Bands and directional averages, uses the directional average to identify the trend and Bollinger Bands to determine potential reversal points for entering transactions.
The implementation of the first strategy with the most optimal parameter values in each time step is carried out in the following sequence:
When there are no open transactions and the random oscillator exceeds 85, we enter a short position. The closing price is set at the last support level of the Donchian channels. To prevent losses, we use two stop loss levels: one based on the maximum allowed pips and the other on the Donchian channel position.
If there’s no open trade and the random oscillator is below 15, we will enter a long position. The trade will close at the latest resistance level in the 14-period Donchian channels. We will set two stop-loss values: one based on our maximum pip loss and the other on the Donchian channel position.
If the trade is open and its position is long, the trade will be closed if the value of the random oscillator is greater than 70. If the trade is open and its position is short, the trade will be closed if the value of the random oscillator is less than 30.
In the implementation of the second strategy, the following order is followed in each tick, using optimal parameters.
If no trade is open and the directional average exceeds 40 for the 14-day time frame, it indicates a strong trend.

In that case, we will enter a short position if the closing price is beyond the upper Bollinger Band and the current price is less than or equal to that upper band for a longer time frame. A stop-loss will be set based on the maximum pips we are willing to risk.
If a trade is open with a long position and the current price value is lower than the middle band value of the Bollinger bands, the trade is closed.
If a trade is open with a short position and the current price value is above the middle band value of the Bollinger bands, the trade is closed.
We employed a deep learning algorithm to dynamically choose the values of four parameters for trading thresholds, loss limits, trading windows, and estimation windows. The values utilized as input for the deep learning algorithm are as follows:

Trading thresholds are set at a distance of 2.5 standard deviations on both sides of the average price difference, with an accuracy of 0.5 standard deviations.
The loss limit thresholds are set at a distance of four standard deviations on both sides of the average price difference, with an accuracy of 0.5 standard deviations.
The trading window is 15 minutes with a 10-minute accuracy.
The estimation window is 60 minutes with a 10-minute accuracy. The estimation window is 240 minutes with a 10-minute accuracy.

Turnover:
Here, data description, cleaning approaches, and feature extraction are discussed. The data includes the first trade price, the highest and lowest traded prices, the last trade price, and the trade volume, represented as candlestick charts (“Table” 1).

Table 1 This data is shown in the form of candlesticks

	Date	Time	Open Price	High Price	Low Price	Close Price	Volume
0	2000.01.02	23:15	1.0078	1.0087	1.0076	1.0086	41
1	2000.01.02	23:30	1.0087	1.0089	1.0079	1.0079	68
2	2000.01.02	23:45	1.0078	1.0132	1.0078	1.0129	66
3	2000.01.03	00:00	1.0129	1.0133	1.0120	1.0122	37
4	2000.01.03	00:15	1.0123	1.0125	1.0120	1.0124	37

The following sections explain each component depicted in the diagram of the presented model (“Fig. 1”).

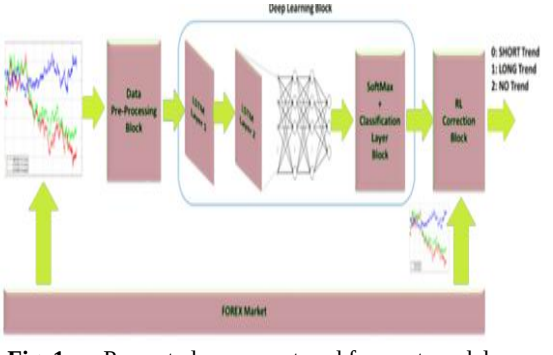

Fig. 1 Presented currency trend forecast model.

Data Preprocessing Block:
The text below explains the purpose of this part, which is to send financial period data. In this Block, the time series data is normalized within the range of 0 to 1, (“Table 2”).
To prepare the proposed model, the creator compiled a comprehensive database of financial data. They collected 99.9% accurate historical data for EUR/USD, GBP/USD, and EUR/GBP from 2018 to 2021. This included open, close, high, and low prices for each currency pair, excluding timestamps (CET time), to support the algorithm

The dataset has been classified into two sets: for training and for testing and validation. Training and validation simulations were conducted annually, as follows:
75% of the dataset was employed by training the model, whereas twenty-five percent was set aside for validation and testing. Both sets were analyzed to ensure equal representation of patterns (LONG, SHORT, INVALID) to prevent overfitting in the deep learning system.
Organized financial data is used as input for the preprocessing framework described in this section, and its output is processed by the subsequent deep learning component.

Table 2 Data pre-processing

AUDUSD	N/A	N/A	0.00345	0.53%
EURUSD	N/A	N/A	0.01184	1.10%
GBPUSD	N/A	N/A	0.01384	1.10%
NZDUSD	N/A	N/A	-0.0024	-0.39%
USDCAD	N/A	N/A	0.00768	0.57%
USDCHF	N/A	N/A	0.00251	0.29%
USDJPY	N/A	N/A	-0.853	-0.57%
EURCHF	N/A	N/A	0.01313	1.39%
EURGBP	N/A	N/A	-0.00148	-0.17%
EURJPY	N/A	N/A	0.823	0.51%
GBPJPY	N/A	N/A	0.951	0.50%
GBPCAD	N/A	N/A	0.02861	1.69%
CHFJPY	N/A	N/A	-1.796	-1.05%

CADCHF	N/A	N/A	-0.00081	-0.12%
NZDCAD	N/A	N/A	0.00021	0.03%
CADJPY	N/A	N/A	-1.227	-1.10%
AUDJPY	N/A	N/A	-0.058	-0.06%
EURCAD	N/A	N/A	0.02466	1.70%
EURAUD	N/A	N/A	0.00755	0.46%
EURNZD	N/A	N/A	0.02615	1.48%
GBPCHF	N/A	N/A	0.01611	1.45%
GBPAUD	N/A	N/A	0.00925	0.48%
GBPNZD	N/A	N/A	0.0299	1.45%
NZDCHF	N/A	N/A	5.0E-5	0.01%
NZDJPY	N/A	N/A	-0.953	-1.04%
AUDCAD	N/A	N/A	0.01047	1.19%
AUDCHF	N/A	N/A	0.0065	1.13%
AUDNZD	N/A	N/A	0.00993	0.93%
USDSGD	N/A	N/A	-0.00889	-0.66%
USDCNH	N/A	N/A	-0.01173	-0.16%
USDHKD	N/A	N/A	0.00352	0.05%
USDDKK	N/A	N/A	-0.0716	-1.03%
USDNOK	N/A	N/A	0.08572	0.81%
USDSEK	N/A	N/A	-0.0922	-0.88%
USDPLN	N/A	N/A	-0.0922	-2.29%
EURPLN	N/A	N/A	-0.05193	-1.20%
USDCZK	N/A	N/A	-0.4416	-1.88%
USDTRY	N/A	N/A	1.31109	4.27%
USDHUF	N/A	N/A	-0.5	-0.14%
USDZAR	N/A	N/A	-0.2017	-1.06%
USDMXN	N/A	N/A	-0.3342	-1.96%
EURZAR	N/A	N/A	0.0169	0.08%
USDRUB	N/A	N/A	0.0967	0.10%
EURRUB	N/A	N/A	N/A	N/A
USDILS	N/A	N/A	0.0504	1.39%
GBPTRY	N/A	N/A	2.04867	5.28%
EURSGD	N/A	N/A	0.00789	0.54%
EURHKD	N/A	N/A	0.08636	1.03%
EURTRY	N/A	N/A	1.74432	5.25%
GBPNOK	N/A	N/A	0.25732	1.94%
GBPDKK	N/A	N/A	-0.00761	-0.09%
NZDSGD	N/A	N/A	-0.0084	-1.02%
GBPSGD	N/A	N/A	0.00716	0.42%
GBPSEK	N/A	N/A	0.0205	0.16%
GBPZAR	N/A	N/A	0.012	0.05%
EURMXN	N/A	N/A	-0.1662	-0.91%
USDKRW	N/A	N/A	24.4	1.89%

Deep Learning Block:

This section provides forecasts for the short- and medium-term performance of the EUR/USD currency pair, focusing on Long Short-Term Memory (LSTM) networks. These networks are a kind of Recurrent Neural Network (RNN) that efficiently seize long-term dependencies. Each LSTM cell has three data ports—input, memory, and output—with a sigmoid activation function (σ) for processing. A tanh activation transforms the cell state and input. The cell retains values over time, while gates manage the flow of data in and out.

The mathematical model that describes the dynamics of a single LSTM cell is "Eq. (4)":

$$f_t = \sigma\big(W_f[h_{t-1}.x_t] + b_f\big).\, i_t = \sigma(W_i[h_{t-1}.x_t] + b_i).$$
$$\tilde{C}_t = tanh(W_c[h_{t-1}.x_t] + b_c).\quad C_t = f_t * C_{t-1} + i_t * \tilde{C}_t$$
$$, o_t = \sigma(W_o[h_{t-1}.x_t] + b_0).\, h_t = o_t * tanh(C_t), \qquad (4)$$

- W_f, W_i, W_C, Wo present the LSTM weights
- b_f, b_i, b_C, bo denote the biases used for cells
- Ct denotes the state of the cell

In the LSTM network's data processing stage, input data from selected currencies is processed using specific equations to calculate the triangular spread. The network retains relevant information while discarding unnecessary data through a forget gate.

We used the LSTM architecture to classify input signals and aggregated data. Our deep learning model includes LSTM, fully linked layers, a classifier, and a SoftMax layer. The classifier assigns outputs to classes based on SoftMax probabilities and calculates loss and performance metrics.

Our model uses LSTM cells to process financial time series data, effectively classifying features via the classifier and SoftMax layer. It excels at feature extraction from LSTM, convolutional neural networks, and autoencoders, demonstrating strong detection capabilities.

The deep architecture that is proposed includes these components:

Input Layer:

LSTM layer (HiddenCellNumber);
LSTM layer (HiddenCellNumber);
Fully connected layer (NumberClasses)

Soft Max Layer:

Classification Layer:

In the developed model, the HiddenCellNumber variable representing the number of cells for each LSTM layer is 368, whereas NumberClasses is 3, i.e. (0): indicates a short process. (1) Shows the long trend. (2) No trend, because the currency is in a trading range, which is usually stated in financial terms to illustrate that a financial instrument does not present a clear trend.

In our model, each currency pair's input time series is segmented using a specific length as the input sequence for the deep learning model. Subsequent quotes form an input sequence to identify the economic trend of the target currency. In this case, we use 100 candles per input currency, representing one segment of the financial time series.

We are focusing on high-frequency trading (HFT) algorithms with 15-minute, 1-hour, and 4-hour time

frames. Our analysis will use the closing prices for the EUR/USD currency pair, along with triangle arbitrage involving EUR/GBP, GBP/USD, and EUR/USD.

To make predictions, our deep learning system processes 100 closing price quotes for the mentioned currencies and generates an estimate for the trend of the next 100 quotes against the selected currency. This predictive estimate is used for trading, for instance, in the case of EUR/USD.

RL Correction Block:

This block aims to correct and verify the currency trends identified in the previous deep learning block. As shown by tests, the prior block's performance is consistent. For instance, when analyzing 2 million data points from 2021, its accuracy in predicting the EUR/USD trend averages 75%. The validation curve is in "Fig. 2".

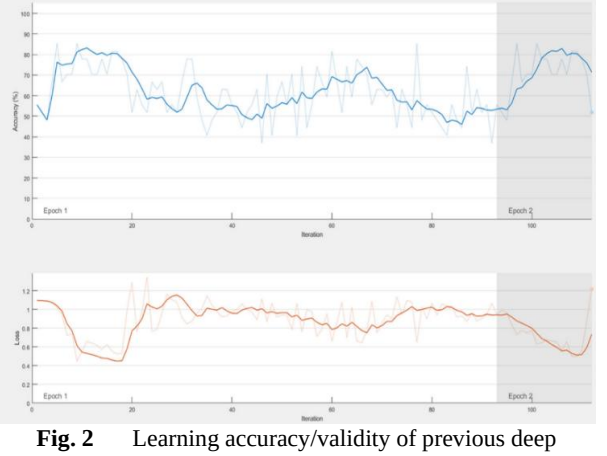

Fig. 2 Learning accuracy/validity of previous deep learning Block.

In this section, we aim to verify and correct the currency trends from the previous deep learning block, which has shown consistent performance. An analysis of 2 million instances from 2021 indicates that the block predicts the EUR/USD trend with an average accuracy of 75% during training, as shown in "Fig.2". To enhance this process, the algorithm now includes an excessive learning layer utilizing unsupervised deep learning and RL methods.

This section outlines the RL (Reinforcement Learning) algorithm in "Fig. 3", which uses two matrices: Wkin (x, y) for input synaptic weights and Wout (x, y) for output weights. Our study suggests a 900-cell RL motor map in a 30x30 grid, with initially randomly populated rows. Input weights might have real values, while output weights, Wout (xk, yk), can only be 0, 1, or 2, representing a short trend, long trend, and trading range, respectively.

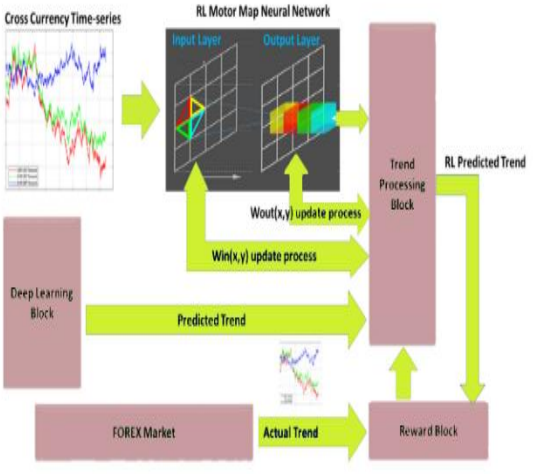

Fig. 3 Developed RL Block for correcting the expected trend made by the deep learning Block.

The learning process analyzes time series data for three currencies: GBP/USD, EUR/GBP, and EUR/USD. The normalized closing prices serve as input for the reinforcement learning (RL) engine. Each neuron in the input layer computes the distance between synaptic weights based on the EUR/USD forecast, resulting in a 30 x 30 distance matrix for the RL engine map: "Eq (5)":

$$d(x.y) = \sqrt{\sum_{K=1}^{N}\left(w_{in}^{k}(x.y) - p_c^{\frac{EUR}{USD}}(T_K)\right) + \sum_{K=1}^{N}\left(W_{in}^{k}(x.y) - p_C^{\frac{GBP}{USD}}(tk)\right)^2} + \forall x.y = 1..30; N = 100 + \sum_{K=1}^{N}\left(w_{in}^{k}(x.y) - p_c^{\frac{EUR}{GBP}}(t_k)\right) \quad (5)$$

By using Equation (4) to obtain the distance matrix \(K(x, y) \), we identify the neuron that is closest to the input point. This selection is based on the Euclidean distance of the synaptic weights. In Poole's time series, we show the correlation between the neuron with the minimum distance \(K(x, y) \) and the coordinates \((xmin, ymin)\).

Let's look at the position (xmin, ymin) in the RL motor map's output layer. This position produces a specific syntactic weight value that reflects the expected trend for the next 100 closing price quotes of the EUR/USD currency, allowing us to achieve practical results.

$$W_{out}(X_{min}.y_{min}) = \begin{cases} 0\ SHORT\ Trend \\ 1\ LONG\ Trend \\ 2\ TRADING\ range \end{cases} \quad (6)$$

At this stage, the RL system evaluates the system state, including Ytmin, Xtmin, DT(Xtmin, Ytmin), Wtin(xtmin, ytmin), $pEUR/USDc(tk)$, wtout(xtmin,

ytmin), $pEUR/pEUR/US\ GBPc(tk)$, and $pGBP$/currency D.

The weights of the winning neuron at \((xtmin, ytmin)\) are adjusted to align the given currency with patterns of transition time segments. This training of the reinforcement learning engine helps it identify financial dynamics and corrects predictions from the previous deep learning block based on input data, ("Table 3").

Table 3 Calculation of profit-loss

	Pred (no_act)	Pred (dec)	Pred (inc)
True (no_act)	-	False_dec_noact	False_inc_noact
True (dec)	-	True_dec	False_inc_dec
True (inc)	-	False_dec_inc	True_inc

	First 15 minutes	First 1 hour	first 4 hours
True (no_act)	73.9	68.31	79.42
True (dec)	64.24	63.91	68.58

By application of the labeling algorithm, a balanced distribution of three classes was achieved in the dataset. Labeling algorithm computes threshold values for time periods, leading to varying class distributions. "Table 4" shows the thresholds and the equivalent data points for each class in both the training and test sets.

Our models predict whether there will be an "increase" or "decrease" in the next 15 minutes, 1 hour, or 4 hours. When a prediction is made, a transaction occurs at the end of the test day for that time frame. If there's no prediction, no transaction happens. A successful trade results in a profit if the prediction is accurate.

Table 4 Statistics of data sets (training and test sets)

Threshold	# of no_action	# of decrease	# of increase	
15 minutes	0.0023	412 (334–78)	400 (327–73)	402 (310–92)
at 1 o'clock	0.0040	413 (317–96)	414 (357–57)	385 (295–90)
4 hours	0.0055	400 (311–89)	422 (370–52)	388 (287–101)

Test on real data:

When analyzing time series data, the main objective is to predict the upcoming value. It's also feasible to forecast multiple future points by specifying the desired number of forecasts. However, during testing, the model's accuracy often diminishes with longer intervals. In 2017, Zhang et al. utilized a comparable model for predicting stock prices.

Our tests also covered 15-minute, 1-hour, and 4-hour forecasts of the directional movement of the EUR/USD currency pair.

We provide the total number of transactions for each test, along with accuracy results based on executed trades. The enhanced forecasting system integrates a deep learning module and a reinforcement learning (RL) framework, achieving an average trend forecasting accuracy of about 85%. "Table 5" displays validation results for the trend prediction line in "Fig. 3", comparing outcomes with and without the RL-based trend corrections.

Table 5 Accuracy of trend forecasting performance for \\ EUR / USD currencies

Fiscal year	Deep learning prediction Block	Deep learning prediction Block + RL trend correction
2018	79.17 %	86.15 %
2019	67.12 %	85.29 %
2020	74.16 %	88.10 %
2021	75.41 %	85.65 %

It's evident from testing the proposed EUR/USD forecasting channel over several years that the trend prediction system built upon deep learning has lower accuracy compared to the modified RL line system.

Forex Trend Forecasting Program: HFT Network Trading System:

In previous chapters, we discussed predicting medium-term currency trends using triangular arbitrage and integrating deep learning and reinforcement learning. Now, it's crucial to develop a trading strategy based on these predictions. The system buys during forecasted LONG trends and sells during SHORT trends. An algorithm prevents opening positions too close together during portfolio fluctuations and aims to close existing positions during declines. The system does not enter trades when forecasts indicate a trading range. This trend prediction method has proven effective, especially for trading the EUR/USD crossover.

We tested our trading strategy using multi-currency data for GBP/USD, EUR/GBP, and EUR/USD from 2018 to 2021, achieving 99.9% accuracy. The simulations were conducted on an AMD Ryzen 16-core server with an Nvidia RTX 2080 Ti GPU and the full MATLAB toolbox. Our trading account started with USD, using a bid/ask size of 2 pips, a capital ratio of 1:400, and a specific LOT size for each FX trade.

The proposed method has been validated from 2018 to 2021 through experiments involving different daily market average windows. "Table 6" compares our method with similar ones in the literature, using the same forex currency for each comparison.

Table 6 Commercial performance analysis of the presented line

Method	FX Currency Cross	ROI (%)	MD (%)
Grid trading system	EUR/USD	95.18	12.25
Trading system	EUR/USD	62.79	23
Threshold (0.025%) – Strategy	EUR/USD	96.542	52.14
Threshold (0.075%) – Strategy	EUR/USD	65.145	8.90
Proposed	EUR/USD	98.23	15.97

The proposed High-Frequency Trading (HFT) method outperforms previous approaches by generating better returns and reducing loss-making operations. It operates on a 3-minute timeframe, executing 50 to 100 trades daily on the EUR/USD pair under favourable conditions. Analysis of "Table 6" reveals significant advantages in Return on Investment (ROI) compared to earlier versions and other methods. This HFT strategy has been effectively implemented in the currency market, offering valuable insights into performance when combined with average maximum drawdown (MD) data.

The ROI increased despite a slight decrease in comparison to the previous channel, justifying the small loss. The proposed algorithm's ROI is significantly lower than the suggested method, even with the same rate of return on invested capital. The method in the literature requires substantial capital investment under various conditions. Therefore, the decrease in Table 6 indicates that the designed profit return method outperforms the previously reported results by the authors in the EUR/USD crossover in the United States. "Table 7" also presents information about the changes in ROI and MD values over the test period of the proposed line.

Table 7 Planned line Business Performance Analysis Fan: Dynamic ROI / MD

Year(s)	FX Currency Cross	ROI Min (%)	MD Min (%)	ROI Max (%)	MD Max (%)
2018.2022	EUR/USD	62.79	8.90	98.23	52.14

In "Table 7", it is evident that the ROI remains almost unchanged within the validation sessions, while the capital utilization undergoes significant changes. It reaches maximum values to compensate for short-term losses caused by incorrect forecasting trends (e.g., MD index).

The data in "Table 6" confirms the effectiveness of the presented technique in anticipating medium-term trends using high-frequency trading (HFT) algorithms. Despite a slight decrease in performance compared to earlier versions, the method remains strong in forecasting trends, enabling better financial assessments and the development of trading strategies for a diverse portfolio to maximize gains and minimize losses.

We're adapting LSTM architectures and reinforcement learning frameworks for the STM32 architecture with integrated Cortex cores. Our goal is to create a portable financial platform, enabling users to monitor stocks, forecast financial trends, and conduct transactions using their mobile phones anytime and anywhere.

Time results of three forms: 15 minutes, 1 hour and 4 hours

Forecast for the next 15 minutes ("Table 8"):

Table 8 ME model: summary of the results of the next 15 minutes

Iterations=50	47.53	248/248
Iterations=100	56.00	45/248
Iterations=150	49.36	248/248
Iterations=200	65.25	59/248
Average	51.72	150.50/248

Technical model results ("Table 9"):

Table 9 TI model: summary of the results of the next 15 minutes

Iterations=50	**52.28**	**190/248**
Iterations=100	51.93	162/248
Iterations=150	54.11	179/248
Iterations=200	54.48	89/248
Average	52.19	158.24/248

Technical and fundamental results, ("Table 10"):

Table 10 ME_TI model: summary of the results of a future day

Iterations=50	48.62	235/248
Iterations=100	56.40	142/248
Iterations=150	47.65	189/248
Iterations=200	63.54	65/248
Average	54.12	158.12/248

Hybrid Model Results:

"Table 11" presents the number of transactions for each case and profit accuracy values in the model. In certain experiments with 200 iterations, our model produced very few transactions for both upward and downward predictions, with an average of 64.75 total predictions.

Table 11 Results of the combined model: 15-minute forecasts

Iterations		Hybrid model-modification based on ME_		Hybrid model-modification based on TI_	
ME	TI	Profit_ accuracy (%)	# of transactions	Profit_accuracy (%)	# of transactions
50	50	70.80	137/248	70.80	137/248
50	100	73.50	117/248	74.36	117/248
50	150	69.60	125/248	77.60	125/248
50	200	81.63	52/248	82.35	52/248
100	50	78.13	32/248	65.63	32/248
100	100	69.23	26/248	65.38	26/248
100	150	70.59	34/248	70.59	34/248
100	200	73.17	46/248	75.00	46/248
150	50	76.56	128/248	78.13	128/248
150	100	72.64	106/248	78.30	106/248
150	150	73.17	123/248	80.49	123/248
150	200	100.00	8/248	100.00	8/248
200	50	80.00	20/248	76.47	20/248
200	100	80.77	28/248	80.77	28/248
200	150	84.00	26/248	82.61	26/248
200	200	83.33	28/248	85.71	28/248
Average		77.32	64.75/248	77.76	64.75/248

Forecast for the next 1 hour:
Results of fundamental model ("Table 12"):

Table 12 ME model: summary of the results of the next 1 hour

Iterations=50	57.44	242/248
Iterations=100	54.40	182/248
Iterations=150	39.83	236/248
Iterations=200	53.57	38/248
Average	51.31	174.50/248

Results of the technical model, ("Table 13"):

Table 13 TI model: Summary of the results of the next 1 hour

Iterations=50	43.31	157/248
Iterations=100	47.78	180/248
Iterations=150	51.37	146/248
Iterations=200	51.85	103/248
Average	48.58	146.50/248

Technical and macroeconomic model results, ("Table 14"):

Table 14 ME_TI model: summary of the results for the next 1 hour

Iterations=50	43.16	234/248
Iterations=100	43.81	226/248
Iterations=150	42.68	164/248
Iterations=200	85.71	10/248
Average	53.84	158.50/248

Results of hybrid model, ("Table 15"):

Table 15 The combined model: forecasts for the next 1 hour

ME	TI	profit_ accuracy (%)	# of transactions	profit_accuracy (%)	# of transactions
50	50	58.39	137/248	57.66	137/248
50	100	58.71	155/248	56.13	155/248
50	150	61.60	125/248	61.60	125/248
50	200	94.74	21/248	95.00	21/248
100	50	76.06	71/248	71.83	71/248
100	100	69.41	85/248	70.59	85/248
100	150	79.37	63/248	80.95	63/248
100	200	100.00	2/248	100.00	2/248
150	50	67.44	86/248	70.93	86/248
150	100	70.80	113/248	74.34	113/248
150	150	69.79	96/248	73.96	96/248
150	200	95.00	43/248	95.00	43/248
200	50	77.78	9/248	75.00	9/248
200	100	84.62	13/248	84.62	13/248
200	150	100.00	9/248	100.00	9/248
200	200	100.00	14/248	100.00	14/248
Average		78.98	65.13/248	79.23	65.13/248

Forecast for the next 4 hours:
Results of macroeconomic model, ("Table 16"):

Table 16 ME model: summary of the results of the next 4 hours

Iterations=50	43.40	235/242
Iterations=100	47.11	242/242
Iterations=150	44.74	228/242
Iterations=200	54.00	120/242
Average	47.31	206.25/242

Technical model results, ("Table 17"):

Table 17 TI model: summary of the results of the next 4 hours

Iterations=50	48.13	187/242
Iterations=100	41.48	176/242
Iterations=150	45.73	164/242
Iterations=200	64.18	79/242
Average	49.88	151.50/242

Technical and macroeconomic model results, ("Table 18"):

Table 18 ME_TI model: summary of the results for the next 4 hours

Iterations=50	44.44	81/242
Iterations=100	42.72	206/242
Iterations=150	46.51	172/242
Iterations=200	61.25	96/242
Average	48.73	138.75/242

Hybrid model results, (“Table 19”):

Table 19 The combined model: forecasts for the next 4 hours

Iterations		Hybrid model-modification based on ME_		Hybrid model-modification based on TI_	
ME	TI	Profit_accuracy (%)	# of transactions	Profit_accuracy (%)	# of transactions
50	50	77.14	105/242	77.14	105/242
50	100	82.98	94/242	76.60	94/242
50	150	78.49	93/242	80.65	93/242
50	200	88.57	36/242	87.88	36/242
100	50	79.46	112/242	82.14	112/242
100	100	80.81	99/242	79.80	99/242
100	150	77.66	94/242	81.91	94/242
100	200	100.00	9/242	100.00	9/242
150	50	78.30	106/242	77.36	106/242
150	100	82.98	94/242	75.53	94/242
150	150	79.78	89/242	80.90	89/242
150	200	Nan	0/242	Nan	0/242
200	50	92.68	43/242	92.68	43/242
200	100	86.36	44/242	86.05	44/242
200	150	90.00	40/242	87.88	40/242
200	200	86.00	51/242	85.11	51/242
Average		84.08	69.31/242	83.44	69.31/242

Validation:

To validate our findings, we expanded our dataset to include a recent case, resulting in 1,687 data points with 785 increases and 845 decreases. We used a labeling algorithm to ensure a balanced distribution across three classes. The dataset statistics are given in “Table 20”.

Table 20 Statistics of extensive datasets (training and testing sets)

Threshold	# of no_action	# of decrease	# of increase	
15 minutes ahead	0.0022	497 (438–59)	515 (464–51)	507 (465–42)
An hour ahead	0.0040	507 (451–56)	527 (476–51)	483 (438–45)
4 hours ahead	0.0054	503 (448–55)	532 (483–49)	480 (432–48)

The dataset was split into 10% for testing and 90% for training. The prediction results for all three forms of the proposed hybrid model, according to the developed data, are reported below.

Forecast 15 minutes, (“Table 21”):

Table 21 Combined model (on extended data set): 15 min forecasts

Iterations		Hybrid model-modification based on ME_		Hybrid model-modification based on TI_	
ME	TI	Profit_accuracy (%)	# of transactions	Profit_accuracy (%)	# of transactions
50	50	55.42	83/152	53.01	83/152
50	100	59.38	96/152	61.46	96/152
50	150	74.63	67/152	76.12	67/152
50	200	81.82	52/152	81.82	52/152
100	50	64.18	67/152	67.16	67/152
100	100	59.49	79/152	65.82	79/152
100	150	66.04	53/152	73.58	53/152
100	200	75.34	84/152	74.65	84/152
150	50	60.47	86/152	55.81	86/152
150	100	57.73	97/152	61.86	97/152
150	150	69.12	68/152	75.00	68/152
150	200	84.13	75/152	84.38	75/152
200	50	83.08	71/152	81.36	71/152
200	100	79.31	67/152	79.66	67/152
200	150	79.31	64/152	78.18	64/152
200	200	85.45	62/152	85.19	62/152
Average		70.93	73.19/152	72.19	73.19/152

Forecast 1 hour, (“Table 22”) and 4 hours forecast, (“Table 23”):

Table 22 Combined model (on extended dataset): 1-hour forecasts

Iterations		Hybrid model-modification based on ME_		Hybrid model-modification based on TI_	
ME	TI	Profit_ accuracy (%)	# of transactions	Profit_ accuracy (%)	# of transactions
50	50	60.71	56/152	57.14	56/152
50	100	71.43	42/152	66.67	42/152
50	150	51.79	56/152	58.93	56/152
50	200	100.00	2/152	100.00	2/152
100	50	63.86	83/152	53.01	83/152
100	100	73.02	63/152	61.90	63/152
100	150	58.11	74/152	58.11	74/152
100	200	86.67	55/152	88.68	55/152
150	50	82.00	50/152	74.00	50/152
150	100	65.00	40/152	67.50	40/152
150	150	62.50	48/152	64.58	48/152
150	200	81.25	37/152	82.35	37/152
200	50	88.89	10/152	88.89	10/152
200	100	83.33	6/152	83.33	6/152
200	150	57.14	8/152	62.50	8/152
200	200	62.50	8/152	57.14	8/152
Average		71.76	39.88/152	70.30	39.88/152

Table 23 Combined model (on the extended dataset): 4-hour forecasts

Iterations		Hybrid model-modification based on ME_		Hybrid model-modification based on TI_	
ME	TI	Profit_ accuracy (%)	# of transactions	Profit_ accuracy (%)	# of transactions
50	50	79.66	59/152	71.19	59/152
50	100	67.21	61/152	67.21	61/152
50	150	68.85	61/152	60.66	61/152
50	200	75.34	84/152	72.73	84/152
100	50	77.61	67/152	73.13	67/152
100	100	62.86	70/152	61.43	70/152
100	150	67.14	70/152	62.86	70/152
100	200	75.00	77/152	71.88	77/152
150	50	79.69	64/152	75.00	64/152
150	100	69.12	68/152	67.65	68/152
150	150	63.77	69/152	59.42	69/152
150	200	75.68	84/152	72.73	84/152
200	50	71.64	71/152	72.46	71/152
200	100	66.67	84/152	66.22	84/152
200	150	67.61	81/152	68.06	81/152
200	200	72.06	75/152	69.35	75/152
Average		71.24	71.56/152	68.25	71.56/152

6 CONCLUSIONS

The proposed hybrid model underwent testing with recent datasets. The test results were consistent with previous findings, presenting just a slight decline in accuracy gains. This work shows that it is possible to use technical and macroeconomic indexes separately or together for training LSTM models for predicting currency pair movements in Forex. Processing these indicators with separate LSTMs and integrating the results through intelligent decision logic enhances prediction accuracy. A third category was added to capture small price changes between consecutive days, improving accuracy in direction prediction. The study introduces a method for defining the unchanged class threshold. LSTM networks were trained for predicting the next day's value and values of k days onward, although they slightly decreased accuracy when predicting three periods. The research also shows that increasing training iterations boosts accuracy, along with reducing the transaction numbers, which consequently lowers potential profit and risk. Future research will extend this approach to include additional currency pairs like EUR/GBP, GBP/USD, and others. We propose developing a trading simulator to validate the model and observe its real-time behaviour, while addressing key trading issues such as account management and leverage ratios. Additionally, we plan to explore the use of deep learning methods for structuring financial portfolios with diverse instruments, allowing a reinforcement learning agent to optimize allocations to minimize risk and maximize profits.

REFERENCES

[1] Benita, F., López-Ramos, F., Nasini, S. A., Bi-Level Programming Approach for Global Investment Strategies with Financial Intermediation, Eur. J. Oper. Res., Vol. 274, 2019, pp. 375–390.

[2] Liu, Z., Wang, J., Supply Chain Network Equilibrium with Strategic Financial Hedging Using Futures, Eur. J. Oper. Res.,Vol. 272, 2019, pp. 962–978.

[3] Sermpinis, G., Stasinakis, C., Rosillo, R., and De La Fuente, D., European Exchange Trading Funds Trading with Locally Weighted Support Vector Regression. Eur. J. Oper. Res., Vol. 258, 2017, pp. 372–384.

[4] Doyle, J. R., Chen, C. H., Patterns in Stock Market Move Ments Tested as Random Number Generators, Eur. J. Oper. Res., Vol. 227, 2013, pp. 122–132.

[5] Oztekin, A., Kizilaslan, R., Freund, S., and Iseri, A., A Data Analytic Approach to Forecasting Daily Stock Returns in an Emerging Market. Eur. J. Oper. Res., Vol. 253, 2016, pp. 697–710.

[6] Zhang, J., Cui, S., Xu, Y., Li, Q., and Li, T., A Novel Data-Driven Stock Price Trend Prediction System, Expert Syst. Appl., Vol. 97, 2018, pp. 60–69.

[7] Chou, J. S., Nguyen, T. K., Forward Forecast of Stock Price Using Sliding-Window Metaheuristic-Optimized Machine-Learning Regression, IEEE Trans. Ind. Inform., Vol. 14, 2018, pp. 3132–3142.
[8] Delaney, L., Investment in High-Frequency Trading Technology: A Real Options Approach, Eur. J. Oper. Res., Vol. 270, 2018, pp. 375–385.
[9] Fischer, T., Krauss, C., Deep Learning with Long Short-Term Memory Networks for Financial Market Predictions, Eur. J. Oper. Res., Vol. 270, 2018, pp. 654–669.
[10] Long, W., Lu, Z., and Cui, L., Deep Learning-Based Feature Engineering for Stock Price Movement Prediction. Knowl. Based Syst., Vol. 164, 2019, pp. 163–173.
[11] Sutton, R. S., Learning to Predict by The Methods of Temporal Differences, Mach. Learn., Vol. 3, 1988, 3, pp. 9–44.
[12] Moody, J., Saffell, M., Learning to Trade Via Direct Reinforcement, IEEE Trans. Neural Netw., Vol. 12, 2001, pp.875–889.
[13] Sutton, R. S., Temporal Credit Assignment in Reinforcement Learning. Ph.D. Thesis, University of Massachusetts Amherst, Amherst, MA, USA, 1985.
[14] Mnih, V., Kavukcuoglu, K., Silver, D., Graves, A., Antonoglou, I., Wierstra, D., and Riedmiller, M., Playing Atari with Deep Reinforcement Learning. ArXiv 2013, arXiv: 1312.5602.
[15] Chung, H., Shin, K. S., Genetic Algorithm-Optimized Long Short-Term Memory Network for Stock Market Prediction, Sustainability, Vol. 10, 2018, 3765.
[16] Carta, S., Corriga, A., Ferreira, A., Recupero, D. R., and Saia, R., A Holistic Auto-Configurable Ensemble Machine Learning Strategy for Financial Trading, Computation, Vol. 7, 2019, pp. 67.
[17] Carta, S., Medda, A., Pili, A., Reforgiato, D. R., Saia, R., Forecasting E-Commerce Products Prices by Combining an Autoregressive Integrated Moving Average (ARIMA) Model and Google Trends Data, Future Internet, Vol. 11, 2019, pp. 5.
[18] Vukovic, D., Vyklyuk, Y., Matsiuk, N., and Maiti, M., Neural Network Forecasting in Prediction Sharpe Ratio: Evidence from EU Debt Market. Phys. A Stat. Mech. Appl., Vol. 542, 2020, pp. 123331.
[19] Maiti, M., Vyklyuk, Y., and Vuković, D., Cryptocurrencies Chaotic Co-Movement Forecasting with Neural Networks. Internet Technol. Lett., Vol. 3, 2020, pp. 157.
[20] Nabipour, M., Nayyeri, P., Jabani, H., Mosavi, A., and Salwana, E., Deep Learning for Stock Market Prediction, Entropy, Vol. 22, 2020, pp. 840.
[21] Nabipour, M., Nayyeri, P., Jabani, H., Shahab, S., and Mosavi, A., Predicting Stock Market Trends Using Machine Learning and Deep Learning Algorithms Via Continuous and Binary Data; A Comparative Analysis, IEEE Access, Vol. 8, 2020, pp. 150199–150212.
[22] Le Cun, Y., Bengio, Y., and Hinton, G. J., Hinton. Deep. Learn., Vol. 521, 2015, pp. 436.
[23] Ding, X., Zhang, Y., Liu, T., and Duan, J., Deep Learning for Event-Driven Stock Prediction, In Proceedings of the Twenty-Fourth International Joint Conference on Artificial Intelligence, Buenos Aires, Argentina, Vol. 25–31, 2015, pp. 2327–2333.
[24] Akita, R., Yoshihara, A., Matsubara, and T., Uehara, K., Deep Learning for Stock Prediction Using Numerical and Textual Information, In Proceedings of the 2016 IEEE/ACIS 15th International Conference on Computer and Information Science (ICIS), Okayama, Japan, Vol. 26–29, 2016, pp. 1–6.
[25] Nelson, D. M., Pereira, A. C., De Oliveira, R. A., Stock Market's Price Movement Prediction with LSTM Neural Networks, In Proceedings of the 2017 International Joint Conference on Neural Networks (IJCNN), Anchorage, AK, USA, Vol. 14–19, 2017, pp. 1419–1426.
[26] Liu, J., Chen, Y., Liu, K., and Zhao, J., Attention-Based Event Relevance Model for Stock Price Movement Prediction, In Communications in Computer and Information Science, Proceedings of the China Conference on Knowledge Graph and Semantic Computing, Chengdu, China, Vol. 26–29, 2017, pp. 37–49.
[27] Qin, Y., Song, D., Chen, H., Cheng, W., Jiang, G., and Cottrell, G., A Dual-Stage Attention-Based Recurrent Neural Network for Time Series Prediction, 2017, pp. 1704.02971.
[28] Zhao, R., Deng, Y., Dredze, M., Verma, A., Rosenberg, D., and Stent, A., Visual Attention Model for Cross-sectional Stock Return Prediction and End-to-End Multimodal Market Representation Learning, In Proceedings of the Thirty-Second International Flairs Conference, Sarasota, FL, USA, Vol. 19–22, 2019.
[29] Sutton, R. S., Barto, A. G., Introduction to Reinforcement Learning; MIT Press: Cambridge, MA, USA, 1998.
[30] Gold, C., FX Trading Via Recurrent Reinforcement Learning, In Proceedings of the 2003 IEEE International Conference on Computational Intelligence for Financial Engineering, 2003, Proceedings, Hong Kong, China, Vol. 20–23, 2003, pp. 363–370.
[31] Duerson, S., Khan, F., Kovalev, V., and Malik, A. H., Reinforcement Learning in Online Stock Trading Systems, Available online: http://citeseerx.ist.psu.edu/viewdoc/download?doi=10.1.1.83.5299&rep=rep1&type=pdf, 2021.
[32] Nevmyvaka, Y., Feng, Y., and Kearns, M., Reinforcement Learning for Optimized Trade Execution, In Proceedings of the 23rd International Conference on Machine Learning, Pittsburgh, PA, USA, Vol. 25–29, 2006, pp. 673–680.
[33] STMicroelectronics S.r.l.–ADG Central R & D Group, 95121 Catania, Italy Dempster, M. A., Leemans, V., An Automated FX Trading System Using Adaptive Reinforcement Learning, Expert Syst. Appl., Vol.30, 2006, pp. 543–552.
[34] Lee, J. W., Park, J., Jangmin, O., Lee, J., and Hong, E., A Multiagent Approach to $ Q $-Learning for Daily Stock Trading. IEEE Trans. Syst. Man Cybern.-Part A Syst. Hum., Vol. 37, 2007, pp. 864–877.
[35] Cumming, J., Alrajeh, D. D., and Dickens, L., An Investigation into the Use of Reinforcement Learning Techniques within the Algorithmic Trading Domain, Master's Thesis, Imperial College London, London, UK, 2015.

[36] Xiong, Z., Liu, X. Y., Zhong, S., Yang, H., and Walid, A., Practical Deep Reinforcement Learning Approach for Stock Trading, 2018, pp. 1811.07522.

[37] Wu, X., Chen, H., Wang, J., Torino, L., Lia, V., and Fujita, H., Adaptive Stock Trading Strategies with Deep Reinforcement Learning Methods, Inf. Sci., Vol. 538, 2020, pp. 142–158.

[38] Carta, S., Corriga, A., Ferreira, A., Podded, A. S., and Recupero, D. R., A Multi-Layer and Multi-Ensemble Stock Trader Using Deep Learning and Deep Reinforcement Learning, Appl. Intel., Vol. 51, 2021, pp.889–905.

[39] Carta, S., Ferreira, A., Podded, A. S., Recupero, D. R., and Sana, A., Multi-DQN: An Ensemble of Deep Q-Learning Agents for Stock Market Forecasting. Expert Syst. Appl., Vol. 164, 2021, pp. 113820.

[40] Seer, O. B., Ozbayoglu, A. M., Financial Trading Model with Stock Bar Chart Image Time Series with Deep Convolutional Neural Networks, 2019, pp. 1903.04610.

[41] Wen, Y., Yuan, B., Use CNN-LSTM Network to Analyze Secondary Market Data, In Proceedings of the 2nd International Conference on Innovation in Artificial Intelligence, 2018, pp. 54-58.

[42] Kim, T., Kim, H. Y., Forecasting Stock Prices with a Feature Fusion LSTM-CNN Model Using Different Representations of the Same Data, Plops one, Vol. 14, No. 2, 2019, pp. e0212320.

[43] Seer, O. B., Ozbayoglu, A. M., Algorithmic Financial Trading with Deep Convolutional Neural Networks: Time Series to Image Conversion Approach, Applied Soft Computing, Vol. 70, 2018, pp. 525-538

[44] Ghorbanifar, Yahyazadeh Far, M., Nabavi Chashmi, Stock Trading Signal Prediction Using Colored Petri Nets and Genetic Algorithm (Case Study: Tehran Stock Exchange), Research Journal of Executive Management, Vol. 11, No. 21, 2019, pp.205-227.

[45] Maleki Moghadam, P. A., Alam Tabriz, P., and Najafi., Designing an Intelligent Model to Determine Stock Trading Signals with A Data Mining Approach, New Researches in Mathematics, Vol. 6, No. 24, 2020, pp. 159-172.

[46] Chen, Y., Hao, Y., Integrating Principal Component Analysis and Weighted Support Vector Machine for Stock Trading Signals Prediction, Neurocomputing, Vol. 321, 2018, pp. 381-402.

[47] Lei, K., Zhang, B., Li, Y., Yang, M., and Shen, Y., Time-Driven Feature-Aware Jointly Deep Reinforcement Learning for Financial Signal Representation and Algorithmic Trading, Expert Systems with Applications, Vol. 140, 2020, pp. 112872.

[48] An, B., Sun, S., and Wang, R., Deep Reinforcement Learning for Quantitative Trading: Challenges and Opportunities, IEEE Intelligent Systems, Vol. 37, No. 2, 2022, pp. 23-26.

[49] Singh, V., Chen, S. S., Singhania, M., Nanavati, B., and Gupta, A., How Are Reinforcement Learning and Deep Learning Algorithms Used for Big Data Based Decision Making in Financial Industries–A Review and Research Agenda, International Journal of Information Management Data Insights, Vol. 2, No. 2, 2022, pp. 100094.

[50] Brim, A., Flann, N. S., Deep Reinforcement Learning Stock Market Trading, Utilizing a CNN with Candlestick Images, Plos one, Vol. 17, No. 2, 2022, pp. e0263181.

[51] Cheng, L. C., Huang, Y. H., Hsieh, M. H., and Wu, M. E., A Novel Trading Strategy Framework Based on Reinforcement Deep Learning for Financial Market Predictions, Mathematics, Vol. 9, No. 23, 2021, pp. 3094.

Int. J. Advanced Design and Manufacturing Technology, 2025, Vol. 18, No. 4, pp. 25-30

DOI: *ISSN: 2252-0406* *https://admt.isfahan.iau.ir*

Sensitivity Analysis of AFM Piezoelectric MC in Electromagnetic Excitation

Ahmad Haghani
Department of Mechanical Engineering, Shk. C, Islamic Azad University, Shahrekord, Iran
E-mail: a.haghani@iau.ac.ir

Reza Ghaderi *
Department of Mechanical Engineering, Shk. C, Islamic Azad University, Shahrekord, Iran
E-mail: Reza.Ghaderi@iau.ac.ir
*Corresponding author

Received: 15 July 2025, Revised: 1 August 2025, Accepted: 16 September 2025

Abstract: Atomic Force Microscopes (AFM) are reliable and accurate tools for surface imaging, mechanical properties detection, and measuring particle motion at the nanoscale. The vibration behavior of the microcantilever (MC) in an AFM is a highly crucial factor for its performance. Also, the dimensions of the MC contribute to its vibratory behavior. The exact surface topography of the sample, and determining its mechanical properties and behavior require thorough knowledge of the effects of different geometric parameters on the coefficients of the interaction forces and the vibration of the MC. In this paper, the authors analyze the dynamic behavior of an air piezoelectric MC under electromagnetic actuation. For this purpose, at first, a dynamic model of the system was developed using the Equation of motion of a continuous beam under vibrations. Then, the effects of the surface interaction force on the behavior of the MC under nonlinear vibrations are investigated. Also, a sensitivity analysis is carried out using the Sobol method to study how the dimensions of an MC affect its nonlinear frequency.

Keywords: Atomic Force Microscopes (AFM), Microcantilever Beams, Sensitivity Analysis

Biographical notes: Ahmad Haghani received his PhD in Mechanical Engineering from the University of IAU Science and Research Branch, Tehran, Iran, in 2017. He is currently an Assistant Professor at the Department of Mechanical Engineering, Shahrekord branch, Islamic Azad University, Shahrekord, Iran. His current research interests include Dynamics and Vibrations. **Reza Ghaderi** is an Associate Professor of Mechanical Engineering at the Shahrekord branch of Islamic Azad University, Shahrekord, Iran. He received his PhD in Mechanical Engineering from University of IAU Science and Research Branch, Tehran, Iran, in 2013. His current research interests include Dynamics and Vibrations.

Research paper

1 INTRODUCTION

AFMs are strong tools for nanoscale surface imaging [1-2], mechanical properties detection [3-4], and measuring particle motion [5]. It is possible to measure mechanical properties on the nanoscale using AFM. It has a wide range of applications, including measurement of intermolecular forces and mechanical properties of materials, pharmacology and biology research, biosensor design, DNA studies, etc [6-8], emphasizing the importance of AFM technology and its development. Several studies have been carried out on modelling and simulation of the MC of an AFM. Park et al. [9] expanded Euler-Bernoulli beam theory using couple stress theory and solved the Equations of equilibrium. Kong et al. [10] studied the Euler-Bernoulli theory for a beam with a circular profile and its boundary conditions, using the modified couple stress (MCS) theory and considering the impact of dimensions. Simsek [11] introduced Euler-Bernoulli theory for hollow beams with circular profiles and confirmed boundary conditions for a dense mass based on MCS theory. Lee et al. [12] presented a V-shaped model for an Euler-Bernoulli MC, using MSC theory. Ansari et al. [13] introduced a piezoelectric MC for Euler-Bernoulli and Timoshenko theories, using MCS theory and voltage. Utilizing MSC theory, Li et al. [6] derived the Equations of a piezoelectric Euler-Bernoulli micro beam. Kahrobaiyan et al. [14] investigated AFM for the Euler-Bernoulli beam, considering MCS theory, the impact of dimensions, and Hamilton's principle. Replacing the laser with a piezoelectric layer in AFMs was first proposed by Tortonise et al. and raised interest due to simplicity, accuracy, and low costs [15]. Fung et al. [16] then modeled the vibrations of an MC with a triangular tip and a piezoelectric layer. Mahmoodi et al. [17] investigated an MC with a piezoelectric layer in AFM and calculated its natural frequency for the first three modes of vibration. Shibata et al. [18] studied diamond MCs in AFM using piezoelectric material as both sensor and actuator and calculated d_{31} coefficient for piezoelectric Zinc oxide (ZnO). Mahmoodi et al. [19] investigated two types of piezoelectric MC in AFM with base excitation and self-excitation variations. In this paper, dynamic modeling of a piezoelectric MC with electromagnetic actuation close to the surface of the sample is achieved. Additionally, Sobol sensitivity analysis is conducted to examine the impact of the MC layers' dimensions.

2 DYNAMIC MODELLING OF MC NEAR THE SAMPLE

A non-homogeneous MC with a piezoelectric layer wrapped between two electrodes on the tip of it is considered for modeling purposes, as is shown in "Fig. 1". The MC is fixed at one end at an angle, and the other end is free. It is affected by interaction forces from the probe and the surface. Theoretical analysis of the structure is conducted using the Euler-Bernoulli theory, with the assumption that the impacts of shear deformation and moment of inertia are negligible.

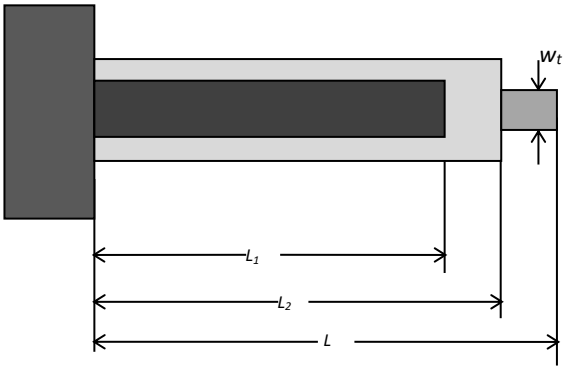

Fig. 1 Schematic of piezoelectric MC.

Using Hamilton's principle, the differential Equation of vibration of the MC is stated below [16]:

$$\rho A\ddot{u} + \left[K\left(x\right)u''\right]'' + c\dot{u} = F_{ts} + F_m \tag{1}$$

Where ρ, A, and c are density, cross-sectional area, and damping coefficient, respectively. F_{ts} and F_m are tip-sample and electromagnetic forces which act on the MC tip. K(x), ρA can be written as:

$$\rho A = \sum_{i=1}^{4} \rho_i h_i w_i \left(H_0 - H_{L_1}\right) + \rho_1 h_1 w_1 \left(H_{L_1} - H_{L_2}\right) + \rho_1 h_1 w_t \left(H_{L_2} - H_L\right) \tag{2}$$

h_i and w_i are the thickness and width of each layer of MC. H is the Heavisine function. The MC can be considered equivalent to three homogenous beams with two different conditions of continuity in each stage. In order to analytically solve "Eq. (1)", Galerkin method is used to separate the variables of "Eq. (1)":

$$v\left(x,t\right) = \sum_{n=0}^{\infty} U_n\left(x\right) q_n\left(t\right) \tag{4}$$

In this Equation, $q_n(t)$ and $U_n(x)$ are global coordinates and the comparison function of the nth vibration mode, respectively. Since the MC is replaced with three homogeneous beams, the comparison function is as shown:

$$U_n(x)=\begin{cases}A_{n1}\sin\beta_n x+B_{n1}\cos\beta_n x+C_{n1}\sinh\beta_n x+D_{n1}\cosh\beta_n x & 0<x<L_1\\ A_{n2}\sin\beta_n x+B_{n2}\cos\beta_n x+C_{n2}\sinh\beta_n x+D_{n2}\cosh\beta_n x & L_1<x<L_2\\ A_{n3}\sin\beta_n x+B_{n3}\cos\beta_n x+C_{n3}\sinh\beta_n x+D_{n3}\cosh\beta_n x & L_2<x<L\end{cases} \quad (5)$$

Here $\beta_n^4=\omega_n^2\rho A/EI$ and A_{n1}, B_{n1}, C_{n1}, D_{n1} are unknown variables that are calculated knowing continuity and boundary conditions, deformation, slope, bending moment, shear force, and also by normalizing relative to mass. By substituting "Eqs. (2) and (3)" into "Eq. (1)" and then calculating the dot product of the result with $U_n(x)$, the ordinary differential Equation below results:

$$\ddot{q}_n+\omega_n^2 q_n+\mu\dot{q}_n-g_{1n}q_n^2-g_{2n}q_n^3+g_{3n}F_m=0 \quad (6)$$

Where:

$$\omega_n^2=\int_0^L U_n(K(x)U_n'')''-F_{ts}'U_nH(x-L)\,dx \quad (7)$$

$$g_{1n}=\int_0^L U_n^3\,F_{ts}H(x-L)dx \quad (8)$$

$$g_{2n}=\int_0^L U_n^4\,F_{ts}H(x-L)dx \quad (9)$$

$$g_{3n}=\int_0^L U_n\,H(x-L)dx \quad (10)$$

3 FREQUENCY RESPONSE ANALYSIS

Multiscale method can be used to solve "Eq. (4)", a nonlinear differential Equation:

$$O(\varepsilon):\quad D_0^2\,q_{n1}+\omega_n^2 q_{n1}=0 \quad (11)$$

$$O(\varepsilon^2):\quad D_0^2q_{n2}+\omega_n^2q_{n2}+2D_0D_1q_{n1}-g_{1n}q_{n1}^2=0 \quad (12)$$

$$O(\varepsilon^3):\quad D_0^2q_{n3}+\omega_n^2q_{n3}+2D_0D_1q_{n2}+2D_0D_1q_{n1}+\mu D_0q_{n1}+g_{3n}F_m-2g_{1n}q_{n1}q_{n2}-g_{2n}q_{n1}^3=0 \quad (13)$$

The solution to "Eq. (9)" appears below:

$$q_{n1}=A_n(T_1,T_2)e^{i\omega_nT_0}+C_c \quad (14)$$

In this Equation, A_n is the amplitude of a complex number and C_c is the complex conjugate of the previous expressions. Substituting "Eq. (12)" in "Eq. (9)" yields:

$$D_0^2q_{n2}+\omega_n^2q_{n2}+2i\omega_nD_1A_ne^{i\omega_nT_0}-g_{1n}(A_n^2e^{2i\omega_nT_0}+A_nA_n^*)+C_c=0 \quad (15)$$

In which, A_n^* is the complex conjugate of A_n. Omitting monic expressions results in the Equation below:

$$2i\omega_nD_2A_1+i\mu\omega_nA_1+\frac{1}{2}g_3F_me^{i\sigma T_2}-8A_1^2A_1^*\gamma_f=0 \quad (16)$$

In which:

$$\gamma_f=\frac{\frac{10}{3\omega_n^2}g_{1n}^2+3g_{2n}}{8} \quad (17)$$

γ_f is a criterion for the effects of the nonlinearities in the system and, thus, it can be introduced as a nonlinear coefficient. If negative, this coefficient suggests hardening and if positive, the softening phenomena. Since, in this case it is always positive, it can be concluded that the nonlinear force between the tip of the probe and the sample always causes softening in the frequency response of the system.

4 SENSITIVITY ANALYSIS OF NONLINEARITY OF VIBRATION

A silicon MC is considered as sample to analyze the sensitivity of the vibrations. Also, a layer of a variety of piezoelectric materials is chosen for further analysis. The piezoelectric layer is placed between two electrodes made of Ti/Au and 0.25 μm thick. The piezoelectric layer goes on top the MC. The necessary geometric and physical properties of the system are stated in "Table 1".

Table 1 Mechanical properties of the piezoelectric MC

	Material	E (Gpa)	ρ (Kg/m^3)
Base Layer	Si	180	2330
Piezoelectric Layer	Zno	130	6390
tip	Si	180	2330

Since scientific and accurate research on the behavior of the MC on the surface requires sensitivity analysis,

Sobol sensitivity analysis is conducted near the surface of the sample to determine the effects of the force coefficients on the vibratory motion of the MC. Therefore, the effects of thickness, width, and length are investigated during sensitivity analysis.

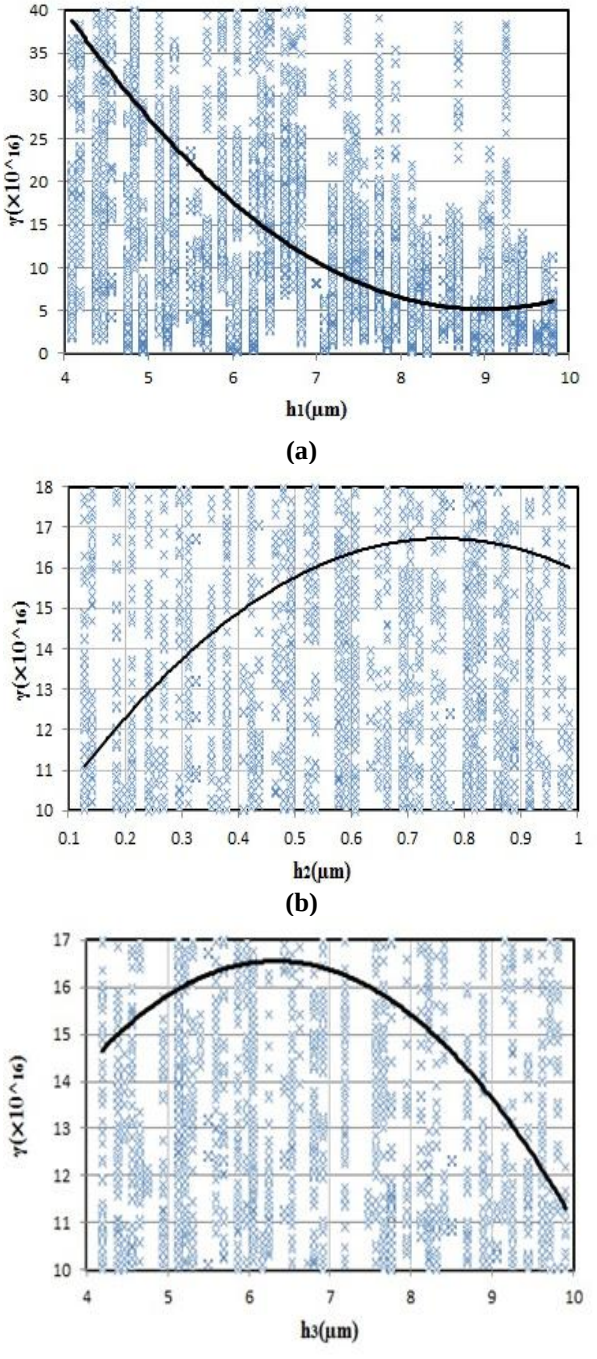

Fig. 2 Effect of MC thickness of layers on nonlinearity: (a): base layer thickness, (b): electrode thickness, and (c): piezoelectric layer thickness.

Figure 2 illustrates the changes in the magnitude of the coefficient of nonlinearity of the system with an increase in the thickness of the MC, electrodes, and the piezoelectric layer. The results in "Fig. 2a" demonstrate that the coefficient of nonlinearity of the system reduces for an increase in the thickness of the MC. This trend continues until a thickness of 8.97 μm, which yields a coefficient of nonlinearity of 5.06 × 10^16.

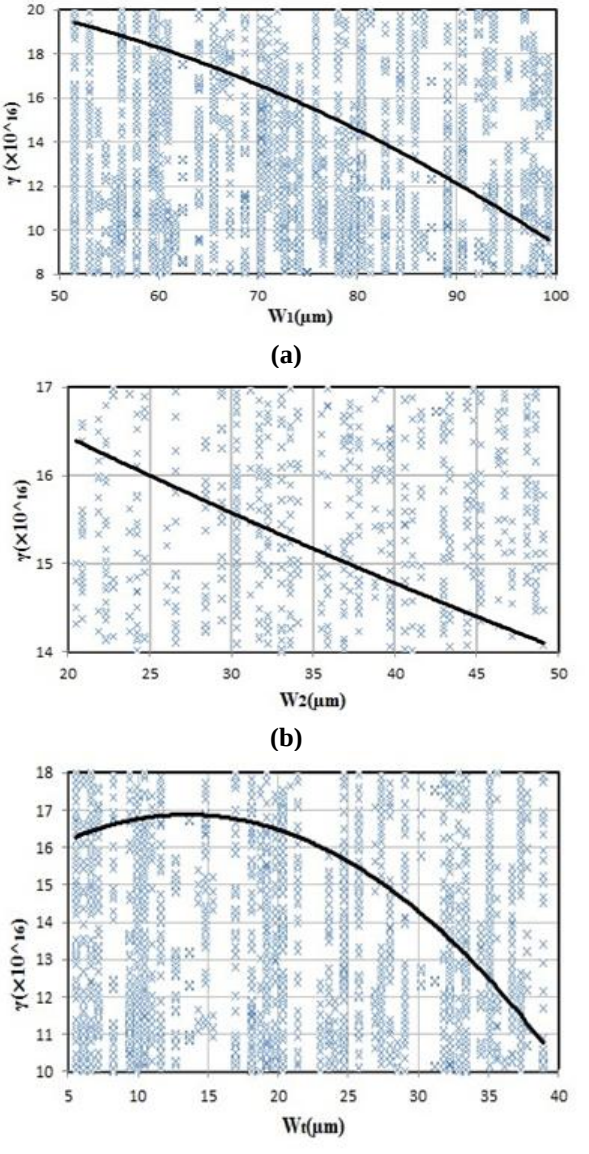

Fig. 3 Effect of width of layers on nonlinearity: (a): base layer width, (b): electrode width, and (c): piezoelectric layer width.

The effect of the thickness of the electrode layer on the coefficient of nonlinearity is presented in "Fig. 2b". According to the analysis results, an increase in the thickness of the electrode layer leads to an increase in the system's coefficient of nonlinearity. The maximum coefficient of nonlinearity in this case is 16.7×10^{16}, resulting from 0.761μm of electrode layer thickness. The

coefficient of nonlinearity of the system decreases with increasing thickness. According to "Fig. 2c", the coefficient of nonlinearity also increases with an increase in the thickness of the piezoelectric layer. The maximum amount results in 6.3 μm of thickness of the piezoelectric layer and equals 16.6×10^{16}. By comparing these three graphs, it is concluded that an increase in the thickness of the electrode layer or the piezoelectric layer initially leads to a rising trend in the coefficient of the nonlinearity of the system, but is followed by a decreasing trend. On the contrary, increasing the thickness of the MC initially decreases the coefficient of nonlinearity, only to be followed by an increasing trend after the minimum point of the graph.

Figure 3 demonstrates how an increase in the thickness of the MC, the piezoelectric layer, and the tip of the probe affects the coefficient of nonlinearity of the system.

Figure 3a shows a decrease in the coefficient of nonlinearity for an increase in the width of the MC. In other words, increasing the width of the MC dampens nonlinear vibrations of the system. Similarly, based on "Fig. 3b", increasing the width of the piezoelectric layer decreases the coefficient of nonlinearity. On the other hand, "Fig. 3c" suggests an initially decreasing but eventually rising trend for the coefficient of nonlinearity as a result of an increase in the width of the tip of the probe. The maximum coefficient of nonlinearity in this case is 16.6×10^{16}, which is achieved for a width of 13.7μm. By comparing these three graphs, it can be concluded that an increase in the width of the MC and the piezoelectric layer reduces the coefficient of nonlinearity. In contrast, such a change in the width of the beam tip leads to an increase in the coefficient of nonlinearity until a maximum width of 13.7 μm is reached, followed by a decrease thereafter.

Figure 4 demonstrates the influence of increasing the length of the MC and the piezoelectric layer on the coefficient of nonlinearity.

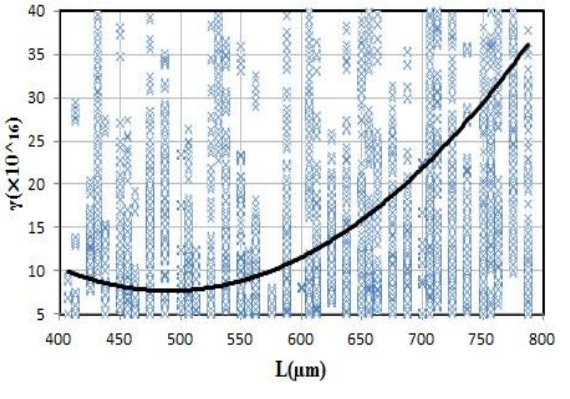

(a)

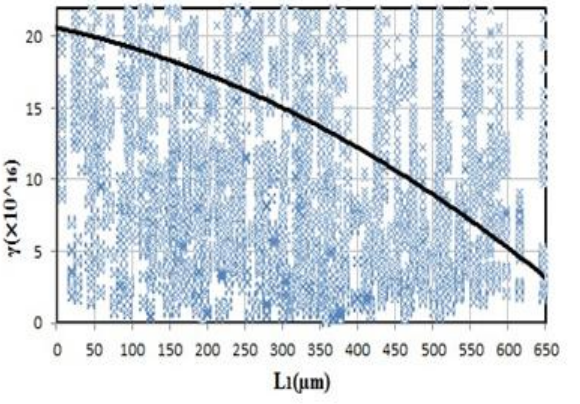

(b)

Fig. 4 Effect of: (a): MC length, and (b): piezoelectric length on nonlinearity.

According to "Fig. 4a", increasing the length of the MC initially leads to a decrease in the coefficient of nonlinearity. The minimum value is 7.49×10^{16}, achieved for a value of 487.5μm. Further increasing the length of the MC brings about an ascending trend in the coefficient of nonlinearity. Figure 4b shows that increasing the length of the piezoelectric layer reduces the coefficient of nonlinearity. This coefficient is 3.47×10^{16} for a piezoelectric layer with a length of 648.5μm, which is 83% less than 20.4×10^{16}, calculated when there is no piezoelectric layer.

5 CONCLUSIONS

To achieve a dynamic model of a vibrating MC in air with electromagnetic excitation, first, contact forces between the tip of the probe and the surface of the sample and the excitation force, concentrated at the tip of the MC, are applied. Then the differential Equations of motion are derived using Hamilton's principle and based on Euler-Bernoulli theory for a vibrating continuous beam. Since the interaction force between the tip of the probe and the surface of the sample is nonlinear and a function of the deformation of the MC, the differential Equations are solved using the Galerkin method, followed by the multiscale method. The impact of the MC dimensions on system nonlinearity is also studied using Sobol sensitivity analysis. The results have shown that:

- An increase in the thickness of the MC leads to an initial increase and eventual decrease in the coefficient of nonlinearity after the minimum point. An increase in the thickness of the electrodes leads to an initial decrease and eventual increase in the coefficient of nonlinearity with a maximum point. Similarly, the resulting graph for the changes in the coefficient of nonlinearity as a result of increasing the thickness of the

piezoelectric layer follows a rising trend initially, only to start falling after reaching its maximum point.

- The coefficient of nonlinearity reduces as a result of increasing the width of the MC or the piezoelectric layer. However, the graph of changes in the coefficient of nonlinearity for increasing the width of the beam's tip is initially descending and then ascending after the minimum point.
- Increasing the length of the MC yields a descending-ascending curve with a minimum point for the changes of the coefficient of nonlinearity. On the other hand, increasing the length of the piezoelectric layer results in a reduction of the system's coefficient of nonlinearity.

REFERENCES

[1] Xu, J., Miao, J., Liu, Y., and Yu, X., Performance Enhanced Terahertz Imaging Using a High-Response Thermomechanical Microcantilever FPA, Infrared Physics & Technology, Vol. 123, 2022, pp. 104161, https://doi.org/10.1016/j.infrared.2022.104161.

[2] Garming, M. W., Kruit, P., and Hoogenboom, J. P., Imaging Resonant Micro-Cantilever Movement with Ultrafast Scanning Electron Microscopy, Review of Scientific Instruments, Vol. 93, No. 9, 2022, pp. 093702, https://doi.org/10.1063/5.0089086.

[3] Yamaguchi, H., Tatami, J., and Iijima, M., Measurement of Mechanical Properties of BaTiO3 Layer in Multi-Layered Ceramic Capacitor Using a Microcantilever Beam Specimen, Journal of the Ceramic Society of Japan, Vol. 127, No. 6, 2019, pp. 335-338, https://doi.org/10.2109/jcersj2.19030.

[4] Kawa, B., Adamski, K., Lizanets, D., and Walczak, R., Mechanical Characterization of Inkjet 3d Printed Microcantilevers, In 2018 XV International Scientific Conference on Optoelectronic and Electronic Sensors (COE), IEEE. 1-3, 2018.

[5] Bertke, M., Kirsch, I., Uhde, E., and Peiner, E., Ultrafine Aerosol Particle Sizer Based on Piezoresistive Microcantilever Resonators with Integrated Air-Flow Channel, Sensors, Vol. 21, No. 11, 2021, pp. 3731, https://doi.org/10.3390/s21113731.

[6] Li, A., Zhou, S., Zhou, S., and Wang, B., Size-Dependent Analysis of a Three-Layer Microbeam Including Electromechanical Coupling. Composite Structures, Vol. 116, 2014, pp. 120-127, https://doi.org/10.1016/j.compstruct.2014.05.009.

[7] Mobed, A., Shirafkan, M., and Charsouei, S., Biosensors Modern Technology in Determination of Anti-Epileptic Drugs (AEDs), Clinica Chimica Acta, Vol. 533, 2022, pp. 175-182, https://doi.org/10.1016/j.cca.2022.06.027.

[8] Wu, C. X., Zhang, N. H., Zhang, C. Y. and Wu, J. Z., Regulation of Thermoelastic Properties of Concave-Packaged DNA Adsorption Films and Its Relevant Microcantilever Detection Signals, Acta Mechanica Sinica, Vol. 37, No. 4, 2021, pp. 705-711, https://doi.org/10.1007/s10409-020-01018-2.

[9] Park, S., Gao, X., Bernoulli–Euler Beam Model Based on A Modified Couple Stress Theory, Journal of Micromechanics and Microengineering, Vol. 26, No. 11, 2006, pp. 2355, https://doi.org/10.1088/0960-1317/16/11/015.

[10] Kong, S., Zhou, S., Nie, Z., and Wang, K., The Size-Dependent Natural Frequency of Bernoulli–Euler Micro-Beams, International Journal of Engineering Science, Vol. 46, No. 5, 2008, pp. 427-437, https://doi.org/10.1016/j.ijengsci.2007.10.002.

[11] Şimşek, M., Dynamic Analysis of An Embedded Microbeam Carrying a Moving Microparticle Based on The Modified Couple Stress Theory. International Journal of Engineering Science, Vol. 48, No. 12, 2010, pp. 1721-1732, https://doi.org/10.1016/j.ijengsci.2010.09.027.

[12] Lee, H. L., Chang, W. J., Sensitivity of V-Shaped Atomic Force Microscope Cantilevers Based on A Modified Couple Stress Theory, Microelectronic Engineering, Vol. 88, No. 11, 2011, pp. 3214-3218, https://doi.org/10.1016/j.mee.2011.09.001.

[13] Ansari, R., Ashrafi, M., and Hosseinzadeh, S., Vibration Characteristics of Piezoelectric Microbeams Based on The Modified Couple Stress Theory, Shock and Vibration, 2014, https://doi.org/10.1155/2014/598292.

[14] Kahrobaiyan, M. H., Asghari, M., Rahaeifard, M., and Ahmadian, M. T., Investigation of the Size-Dependent Dynamic Characteristics of Atomic Force Microscope Microcantilevers Based on The Modified Couple Stress Theory, International Journal of Engineering Science, Vol. 48, No. 12, 2010, pp. 1985-1994, https://doi.org/10.1016/j.ijengsci.2010.06.003.

[15] Tsukada, M., Watanabe, N., Theoretical Analyses of Cantilever Oscillation for Dynamic Atomic Force Microscopy in Liquids, Japanese journal of applied physics, Vol. 48, No. 3, 2009, pp. 035001, https://10.1143/JJAP.48.035001.

[16] Fung, R. F., Huang, S. C., Dynamic Modeling and Vibration Analysis of the Atomic Force Microscope, J. Vib. Acoust., Vol. 123, No. 4, 2001, pp. 502-509, https://doi.org/10.1115/1.1389084.

[17] Mahmoodi, S. N., Jalili, N., Piezoelectrically Actuated Microcantilevers: An Experimental Nonlinear Vibration Analysis, Sensors and Actuators A: physical, Vol. 150, No. 1, 2009, pp. 131-136, https://doi.org/10.1016/j.sna.2008.12.013.

[18] Shibata, T., Unno, K., Makino, E., Ito, Y., and Shimada, S., Characterization of Sputtered ZnO thin Film as Sensor and Actuator for Diamond AFM Probe, Sensors and Actuators A: Physical, Vol. 102, No. 2, 2002, pp. 106-113, https://doi.org/10.1016/S0924-4247(02)00339-4.

[19] Mahmoodi, S. N., Daqaq, M. F., and Jalili, N., On the Nonlinear-Flexural Response of Piezoelectrically Driven Microcantilever Sensors, Sensors and Actuators A: Physical, Vol. 153, No. 2, 2009, pp. 171-179, https://doi.org/10.1016/j.sna.2009.05.003.

Int. J. Advanced Design and Manufacturing Technology, 2025, Vol. 18, No. 4, pp. 31-39

DOI: ***ISSN: 2252-0406*** ***https://admt.isfahan.iau.ir***

Investigating Mental Models of Managers of Research and Technology Funds, in Accordance with the Concepts of Behavioral Economics, for the Development of Innovation Ecosystem in Manufacturing

Mahla Sadat Hosseini * Mohammad Yazdaanian, Majid Mokhtarianpour

Tehran University, Tehran, Iran

E-mail: mahla.hosseini@ut.ac.ir, yazdanian@ut.ac.ir

*Corresponding author

Received: 22 August 2025, Revised: 17 September 2025, Accepted: 29 October 2025

Abstract: The purpose of this article is to recognize and understand the views and mental models of managers of research and technology funds in line with the new concepts of behavioral economics. Research and technology funds are considered as one of the facilitating arms of the economic system, and make a significant contribution to the sustainable development of the country. The main idea is to recognize the viewpoints and subjectivities of these managers as scientific human resources, who influence the advancement of technology and research of the country, in line with the concepts of behavioral economics. The present study includes 13 senior managers of research and technology funds in 2022, which were obtained by purposive sampling and through in-depth interviews on the propositions resulting from Q methodology. The results show 17 verified propositions and three mental models of managers of research and technology funds related to behavioral economics concepts. The results indicate the existence of cognitive and behavioral bias of representativeness, competence, and confirmation in the first mental model, anchoring and adjustment bias, as well as overconfidence bias in the second mental model. In the third mental model obtained from managers, there are bias of eventuality and data dilution. Finally, by providing nudges (suggestions), an attempt has been made to reduce these biases and to see more efficient management decisions.

Keywords: Behavioral Economics, Managers of Research and Technology Funds, Mental Model, Sustainable Development

Biographical notes: Mahla Sadat Hosseini is currently a PhD student at Tehran University, Iran and his main research interests are Public Administration, Nano Coatings, and Mechanical Engineering. **Mohammad Yazdaanian** is currently a PhD student at University of Tehran, Iran and his main research interests is Mechanical Engineering. **Majid Mokhtarianpour** is currently Assistant Professor at the department of Public Administration, University of Tehran, Iran.

Research paper

1 INTRODUCTION

The age of digital and scientific economy has made many changes in the world of organizations, and these organizations have faced intense competition in this dynamic environment. Thus, revitalizing economic life takes place with a view to the competitive advantage and even the survival of economic organizations, the increasingly important ability to adapt to the rapidly evolving environment, introducing the superior strategies and new ideas that meet the needs of society, and ultimately introducing new products behind the knowledge-based and postindustrial economy [1-2]. The turbulent condition of the current economic fields indicates the need to rearrange economic concepts in organizations, decision makers, consultants and other involved people. Therefore, it is important that the effective organs in such proceedings, given the increasing speed of globalization that overshadows all social and economic systems, be equipped with up-to-date knowledge and new economic concepts such as behavioral economics. Because it tries to better describe and analyze our behaviors and decisions by combining economic knowledge with the psychology achievements, and in particular cognitive psychology. These conditions have forced managers to change paradigms to lead their organizations and to make strategic decisions faster [3-4]. Hence, the term behavioral economics is considered as a major challenge for behavioral management researchers and executives. In response to this challenge, many modern researchers have focused on understanding the cognitive aspects and mental structures of related managers. These researchers believe that in order to be familiar with the formation and emergence of behavioral economics concepts, they must go to the models of managers' minds and somehow deal with decoding this black box. In his book Organization Theory, Hatch writes: "The power of words is transferred to those who have better access to or influence on the mainstream discourse" [5]. With a similar argument to those who, as decision makers and main speakers as influencers, bring important results in the economic body of the society with appropriate comments, now if these people know the concepts of behavioral economics and believe them, what will be the result?

Research and Technology Funds are non-governmental institutions established alongside science and technology parks, universities and other research centers and technology development institutions in all provinces, and according to Article 100 of the third program, article 45 of the fourth program, and Article 44 of the Law on Removing Barriers to Competitive Production and Promoting the Country's Financial System, with the aim of creating opportunities for participation and investment of the non-governmental sector. Shareholding financing of research, scientific and technological activities, start-ups, technologists, creators, accelerators and knowledge-based companies up to non-governmental and up to public sectors in these funds is up to 49 percent, and the rest is non-governmental sector, and the upstream policies are based on the encouragement and presence of the majority of the private sector. Also, these research and financial institutions, as a consequence of the Law on the Protection of Knowledge-Based Companies and Institutions, are responsible for financing knowledge-based companies, and for this purpose, they provide various financial services to these companies across four groups of facilities, guarantees, investment and empowerment. So far, knowledge-based companies, whose number has exceeded 6400 companies, have received more than 190 billion Rials of financial services from the Innovation and Prosperity Fund. However, although the number of knowledge-based companies has gradually reached more than 6,400 companies over the past 10 years and is still increasing with a gentle slope, the share of these companies in the country's economy - Gross Domestic Product - is still estimated to be less than 1%, which is significantly far from the desired amount. Increasing the share of knowledge-based companies in the country's economy reasonably requires increasing their number and simultaneously developing the market and selling existing companies. This research tries to identify managers' mental models and provide alternative solutions for managing the allocation of financial resources in the field of research and technology towards sustainable development of the innovation ecosystem, considering the effective and increasing role of research and technology funds, and using new findings from behavioral economics.

Therefore, the main questions of the present research are as follows:

1. What is the mental model of managers of research and technology funds in Iran?
2. What is the categorization of these factors based on Q's methodology? In other words, what mental models do the participants have about the research topic?
3. According to the approaches of behavioral economics, what are the behavioral bias of managers of research and technology funds?

2 LITERATURE REVIEW

2.1. The Meaning of Mental Models

Although mental models are not actually visible, people can draw them, and their performance makes these models emerge and appear in the real world. In other words, mental models are internal aspects of external realities; This means that these models aim to describe how the surrounding world works, and draw a

manifestation of the external world and the relationships of its different parts in our minds, and we take action based on our conclusions from these phenomena, which in turn, form our behavior. Essentially all human beings, including managers, have an approach in their mind as a personal algorithm to solve problems or make decisions about issues, which is completely influenced by their mental model. Forrester believes that the image of the world around us which we have in our minds is just a model. No one imagines the entire world, government, or country in his mind; rather they only select concepts and relationships between them and use these to represent the real system in their mind. A view of human reasoning is determined according to the concepts of mental models and depends on the type of mental model. Johnson Laird believes that people's mental models are affected by perception, imagination, or discourse. Essentially, the structure of this type of thinking is exactly opposite to the use of solid logics used in judicial and formal theories of reasoning [12]. Laird and Byrne developed the theory of mental models and hypothesized that human reasoning about the phenomena around them is not based on logic, but is based on their mental models. The models are established upon a series of basic assumptions that make them perfectly distinct from other concepts of mental representation of peripheral realities in the psychology of reasoning and reasoning. According to their opinion, each mental model represents a possibility of all the different ways it can happen. Consequently, mental models are symbolic and only consider conditions that are likely to occur. Therefore, according to critical thinking, a proposition that is thought to be wrong may temporarily be displayed as correct. Like other people, managers have their own mental models. For example, the level of experience of two managers causes them to make different decisions in the operational field under similar conditions, because their perceptions of the issue may be completely different. Other factors that can affect decisions include politics, religion, culture, etc. Managers use mental models to refine the huge amount of information and stimuli received from the environment during the day. The working days of most senior executives are filled with meetings, calls, reports, political and economic news, etc. The type of their mental model directs their focus to stimuli they consider more important and relevant. Accordingly, a stimulus may be considered vital while it is not, or vice versa, and this may cause them to make a wrong decision. Mental models are reference frameworks by which managers interpret world phenomena and communicate with the real world through them. Mental models are rich in the knowledge of decision makers about peripheral phenomena, although they vary from person to person. These models, in different ways, affect the decisions that underpin the company's micro and macro strategies. Considering the research conducted in the field of behavioral economics in Iran, it has been observed that so far, no research has been carried out on the mental models of managers of research and technology funds at the country level in accordance with the concepts of behavioral economics.

Aslani et al. by examining the role of mental models in the organizational change process, have concluded that employees who have mental models of goal orientation, monism, balance orientation, pragmatism, and program orientation are more effective in organizational change processes and their acceptance [6]. Salsabil et al. in research titled "Explaining consumer behavior based on cognitive and behavioral sciences", have achieved 3 themes and 16 frequently repeated components. These decisions are categorized as complex decisions, daily decisions, limited decisions, unplanned purchases and instant buying decisions. Finally, they suggest that, considering that a rational human is an unrealistic human being, new observations and experiments can be considered as significant implications in explaining human behaviour [7]. Malekzadeh and Rahimnia (2016), by examining the mental models of managers of knowledge-based companies regarding the meaningfulness of work, using the Q methodology, identified four mental models of managers, which are career expectations, attitude to career, career nature, and individual characteristics. Recognizing these models is used in explaining and presenting appropriate strategies for job design and the path of development and progress of knowledge-based companies [8]. Sarboland (2021), in a study titled "Understanding the role of managers' mental models in innovative work behavior at public organizations using the Q-methodology", analyzes that the five main subjectivities of managers of public organizations in terms of innovative work behavior are examining opportunities, generating ideas, promoting ideas, realizing ideas, and contemplation [9]. Askarifar (2015) in his research has examined the mental model of Iranian entrepreneurs in providing capital to start a business. The findings show that the model of providing entrepreneurial capital in the start-up phase of business in Iran is significantly different from other countries studied. Furthermore, the results show that the laws and governance structure related to business have the greatest impact on the mental model of entrepreneurs [10]. Nasehi Far et al. (2021) in their research investigated the relationship between mental model and open innovation in the sport manufacturing industry, and the results showed that these two factors have a significant relationship with each other. They concluded that without a proper mental model, open innovation cannot be achieved. In other words, if there is a high level of mental ability in a manager's mental model, he can deal with the aspects of open innovation, including entry and exit, knowledge of customer and employee participations, and evaluation of his company; but if he

has more mental involvements in his mental model, he will be less able to engage in open innovation, because he is very busy. In this regard, each mental model determines how managers understand and interpret the company's system, and consequently how they react to it. Managers' mental models can be considered as the basis of innovation and changes in the company [11].

2.2. Research Methodology

According to the nature and objectives of the current research, a qualitative approach and Q methodology have been used in it. The Q method is usually considered as the link between qualitative and quantitative methods. Because, on the one hand, the selection of participants is not done through probabilistic sampling methods, but the sample of individuals is purposively selected with a small size, which brings it closer to the qualitative method; and on the other hand, the findings are obtained through factor analysis and in a completely quantitative manner. Also, due to the method of data collection (sorting), it is possible to be more deeply aware of the subjectivity of the participants [12]. The main difference between Q method and other social science research methods is that in Q methodology, people are analyzed instead of variables. The Q method consists of five phases. With library studies in the first phase, the research literature is reviewed, and the background for conducting the next phases is provided. By performing the first phase, the researcher gets a deep understanding of the subject. Using interviews and reviewing documents in the second phase, additional information will be obtained about the issues relating to the research. In the Q method, the sample of people is selected from those who have a special relationship with the research topic. In this study, the sample was selected from the managers of research and technology funds in the country. Lincoln and Guba state that in a carefully guided study in which sample selection is evolutionary and sequential, a saturation point can be reached with about 10 participants. Coyle states that if the purpose of the interview is to explore and describe the beliefs and attitudes of the interviewees, a sample size of 15 ± 10 will be sufficient to conduct the interview, according to the available time and resources. In this article, the researcher reached information saturation after conducting ten interviews. Carrying out this step will lead the researcher to describe countless aspects of the phenomenon. The results of the first and second phases constitute the discourse space. In the third phase, it should be organized by evaluating and summarizing the contents of the discourse space and selecting a sample of statements as a Q sample among them. McKeown and Thomas suggested a number of 30 to 100 statements for the Q sample, but usually between 50 and 70 statements are selected. Donner believes that the appropriate number of statements for the findings to be statistically valid is between 20 and 60 statements. In the fourth phase, the participants will sort and categorize the Q deck. This phase is actually the stage of data collection. In the last phase, the collected data will be analyzed using the Q-factor analysis method, and the extracted factors will be interpreted. It should be noted that in quantitative studies, there is a community where the results of the study are used at that level, and it has a sample that is selected randomly and is generally a representative sample of that society. The Q method lacks such a community and sample, and usually the researcher selects a sample of people from among those who either have a special relationship with the research topic or have special beliefs. On the other hand, the Q study does not provide information about the "distribution" of the variables in order to discuss their generalizability; rather, it talks about the "existence" of different subjectivities. While the whole sample is important in conventional quantitative studies, in the Q study, the collocation of each individual is considered to be quite important and a significant type of information. Therefore, unlike the usual quantitative methods in which a small number of questions are asked from a large number of respondents, in the Q study, a large number of questions are asked from a small number of respondents. In fact, quantitative studies emphasize distributions more than anything else, but Q studies emphasize questions. Therefore, the concept of generalizability in the Q study is quite different, because it only seeks to discover different mental models, and in order to discover a model, the existence of only one person with that specific model is sufficient.

3 VALIDITY AND RELIABILITY OF RESEARCH

Regarding the validity of the Q method, it can be said that the validity check is considered when a construct (a latent characteristic) is measured, because in such a case, the researcher is faced with the question of whether the constructed scale really measures the same thing it is intended to measure. This is despite the fact that the study of Q does not seek to measure any construction. What can be said about Q's study is the comprehensiveness of Q's sample statements. In other words, the researcher should ask himself whether the collected statements have such comprehensiveness and scope that they can show different subjectivities. Hence, the validity of the content can be evaluated based on the rating given by the participants to the statements and their adjacent statements. Also, formal validity is possible by examining the level of satisfaction of the participants regarding the capacity and capability of statements to show their mentality; i.e., whether the existing statements have addressed the various aspects of the subject under investigation so that they can express their mentality through sorting. For Q sorting,

reliability can also be considered. That is, it can be asked whether a participant sorts a deck of cards with the same instructions in different iterations in the same way. It should be noted that depending on the subject of the Q study, the spectral grades, and the number of cards, it can be expected that the repetition of the sorting will not lead to a completely identical result.

4 RESEARCH FINDINGS

By reviewing cognitive biases in behavioral economics, active statements in the field of economic behavior of managers of research and technology funds will be discussed.

At this stage, it has been tried to study written and unwritten opinions about behavioral economics and related mental models, macro-decisions, the comments of 13 CEOs of research and technology funds, and a review of the research literature among the 30 propositions obtained from the background and available sources, and finally 17 statements are confirmed, which are shown in the "Tables 1 to 3". For categorization, a Q-plot was set up for 17 Q-set statements in such a way that the managers could sort the sets of statements in a normal distribution and according to the standard method, from so much agree (+4) to disagree so much.

Table 1 Cognitive biases in behavioral economics

Access	People estimate the probability of an event based on its ease of recall.	traders place more emphasis on their recent trades and allow recent results to interfere with their trading decisions
Dilution effect	Irrelevant data undermines other relevant data	Using more trading tools and concepts for price analysis can weaken the importance of decision drivers
The sophistry of gamblers	People believe that probabilities should cover each other in short term.	Traders have misinterpreted the randomness of phenomena and believe that after three losing trades, the probability of a winning trade is higher, while the probability of the occurrence of phenomena does not change based on past results.
Anchoring	Paying too much attention to the first available piece of information.	When it comes to entering a trade, people base their entire charting and analysis on the entry price, and don't pay enough attention to the overall image of the market.
Confirmation-Affirmation	i.e., look for information that confirms your beliefs, ideas and actions.	The trader disregards the reasons and signals that disapprove his trade and only looks for confirmations.
Overconfidence	People have higher self-confidence in doing things, contrary to their skill level.	Traders misjudge their level of experience and skill; and those who lose all the time, do not consider it their fault.
Selective Perception	Forgetting the things that cause discomfort	Traders easily forget their mistakes and wrong trading decisions that cause them to lose heavily.
Profiteering	We consider ourselves responsible for our profits and do not bear the responsibility for our losses.	Traders blame the market or unfair conditions when they make losses, but accept full responsibility for their wins.
Insensitivity to sample size	Understanding the difference between large and small sample sizes.	Traders often make their assumptions about the accuracy of their trading system based on a few limited trades or change their trading parameters after a few losing trades.
Epidemic Mentality (Communicable)	Avoid contact with people who have been infected in previous contact.	Traders no longer go to markets and financial instruments in which they have experienced a heavy failure, even if the failure was due to the trader's own error.
Perception	We consider events happening right now to be more likely to have occurred in the past.	People by looking at past trades and investigating the cause of their failure, come to some conclusions that they did not have at the time.
Hot hand sophistry	After success in one random event, another success is also highly likely.	Traders believe that when they are on a winning streak (consecutive wins), it becomes easier to trade, and they can sense where the market is going.

Peak-End Rule	People judge an event based on how they feel at the peak of that event.	Traders look at losing trades and only see how much profit they gained, but they do not take into account the problem that followed. In fact, traders in losses are more likely to regret why they did not take the profits of the price movement than to regret why they lost so much, and they see the loss in not making money rather than in not losing.
Simulation Subjectivity	People regret more when they miss an event by a small amount.	A price where you missed profit by a small margin, or a trade where you stop because of a few pips, is more painful than other trading failures.
Social Reason	When people are not sure what to do, they look at what other people are doing.	Traders are more likely to seek advice from other traders when they are unsure of what to do, even if their trading strategy is completely different from theirs.
Framing	People make decisions based on how things appear. A profit is much more valuable than a loss, and a certain profit is much more valuable than a probabilistic larger profit.	Traders make trades in profit too early because the value of the current profit is greater than the value of a larger profit to them in the future.
Drowning	We invest in one thing just because we have invested in it before.	Add to a losing trade, because you invested in it, even if there is no reason to do so.

Table 2 CEOs opinions about behavioral economics

Statements No.	Statements	Factor scores of the 1'st mental model	Factor scores of the 2'nd mental model	Factor scores of the 3'rd mental model
Q1	The impact of the directives of the Vice Presidency for Science and the Innovation and Prosperity Fund is clearly evident in the performance of the funds.	22	40	36
Q2	Regarding the allocation of credits and facilities to knowledge-based companies, they will perform their analysis based on financial statements and profit and loss statements, and will not pay attention to the overall image of the market for that product in micro-facilities.	33	7	4
Q3	The bad record of the knowledge-based company has a great impact on not granting facilities to that company.	50	15	23
Q4	Failure to repay the facilities on the due date is directly related to the practical experience and reports of the assessors of these funds.	40	13	18
Q5	The ability of the knowledge base company to repay the loan is more important than the amount of the granted facility.	40	25	9
Q6	The current economic conditions of the country are the main reason for the reluctance of funds to participate in venture capital.	36	30	21
Q7	Short-term profitability from granting facilities for managers and appraisers is more attractive than higher profit with more risk.	28	19	4

Q8	Internal resolutions of research and technology funds are more enforceable than upstream resolutions.	19	5	12
Q9	The procedures established in different funds have a direct effect on the performance of other funds.	8	6	19
Q10	Referring high-yield and low risk projects, prevents managers from paying attention to lower-yielding business projects.	4	19	4
Q11	The effective contribution of communication in the plans sent to the funds is more than their skills and expertise.	39	15	30
Q12	Funds, as the influential leverage in the system of innovation and value creation, are directly involved in increasing the contribution of domestic production.	25	15	22
Q13	Funds, as venture capital project contributors, carry out large-scale transactions due to their high level of information.	11	29	38
Q14	Without a feasibility study and proper presentation plans of firms, it is not possible to invest in the plan.	39	20	37
Q15	In participating in venture capital projects, funds do not exceed a certain price range and prefer to diversify their risk portfolio.	20	35	27
Q16	Fund management board members tend to continue many low-yielding plans (as a result of wrong decisions) until reaching the break-even point.	27	8	10
Q17	Failure to timely reimbursement of firms' loans will cause the funds to not approve their loan requests in the future.	40	22	15

Table 3 Q-plot

Absolutely agree					Absolutely disagree			
-4	-3	-2	-1	0	1	2	3	4
(2)								(2)

5 CATEGORIZATION AND CONCLUSION

1- What is the mental model of the managers of research and technology funds in Iran? What is the categorization of these factors based on Q methodology? In other words, what mental models exist among the participants regarding the research topic?

Mental model 1: The first mental model includes the category of managers who, due to the non-specialist nature of the fund, the high initial capital, and the composition of the fund's board of directors, focus on the internal regulations and are less inclined to take risks in accepting investment plans and giving facilities. They pay a lot of attention to the experience of the fund's assessors and experts and consider the responsibility of their mistakes to be excessive. They spend a lot of time reviewing the plans and finally, with the intuitive view of the board members to reduce the risk of the plans, they refuse to participate.

Mental model 2: In the second mental model, there are managers who are interested in attracting new projects to participate in investment according to the specialized nature of their fund. These managers believe that all plans should be reviewed and their portfolios should be more diversified through a feasibility study. They share

in the risk of investments through their connections and by relying on their information knowledge about the specialized field (for instance, the electricity and energy fund). In granting all kinds of facilities, according to the credit line available in the Innovation and Prosperity Fund, they accept projects without prioritization and in order to accelerate earnings. According to these managers, the goal of earning profits and a better performance record of the fund is more important than the mission of establishing research and technology funds (the growth of domestic production and the increase of turnover in the country).

Mental model 2: These managers have a systematic view of the current situation and prepare explanatory plans according to market analysis in various fields and using the knowledge of experts. They try to reduce errors by organizing seminars and sharing and conveying experiences, and they do not limit themselves to their information. In the meetings of the board of directors, they persuade the shareholders and members of the board of directors, citing the information collected. This group have success in attracting high-return projects through their connections. The long-term view of these managers has caused them to experience higher profitability in the long term in participating in high-risk investments.

2- What behavioral errors occur in these mental models according to behavioral economics approaches?

In the first mental model, investors claim to have confidential information about the company and refuse to diversify it. People tend to have a lot of confidence in the correctness and accuracy of their judgments; and in an experiment on the General Information Test that was conducted, the dominant answer of them was that they were 100% sure, while they had actually answered 70 or 80% of the questions.

In the first mental model, managers and their investors have a representative cognitive bias. Essentially, humans tend to imagine chances and possibilities in a way that is consistent with their previous ideas and perceptions, even when the resulting inference is statistically invalid. For example, the "gambler's illusion" refers to the common misconception that success and luck in betting and gambling occur periodically. Similarly, fund managers tend to determine the success of an investment, for example, in Company A, by placing it in a familiar and understandable classification table. The description of this feature in brief is that investors often behave in a stereotypical manner when making investment decisions.

Another behavioral bias observed in the first mental model is when managers feel that they are skilled or knowledgeable, and prefer to bet on ambiguous phenomena that they believe can predict their consequences and outcomes based on their own judgment and evaluation, rather than betting on random events of equal probability. By contrast, when they don't feel proficiency or awareness in themselves, they prefer to bet on chance events. This is called the "resourcefulness" effect (or "know-how" effect), which is itself an aspect of ambiguity aversion and has a lot to do with fund managers.

Ambiguity aversion can lead investors to believe that the stocks of the companies they work for are safer and less risky compared to the stocks of other companies. The managers of subsidiaries of the holdings of research and technology funds are more reliable.

It should be noted that when investors are exposed to the resourcefulness effect, it is very important to advise them about potential mistakes such as repeated trades that are detrimental to one's assets. The resourcefulness effect is also involved in the formation of indigenous dependence bias or the tendency to keep assets close to oneself. Graham, Harvey, and Hong showed that the investors who are more willing to convert a portion of their assets into foreign securities are those who feel that they have the most resourcefulness in investing in foreign assets. The basic advice is not to let resourcefulness in a particular field prevent you from investing in other fields.

Another behavioral bias in the first mental model is the confirmation of fund managers and board members. This bias, called confirmation bias, refers to our ability to convince ourselves to believe whatever we like. We are overly focused on the events that consolidate and reinforce our desired outcomes, undervaluing what conflicts with them. Confirmation bias can be seen as a form of selective bias in gathering evidence and documents in order to determine certain beliefs, through which the decision-maker either overvalues information that confirms their claims or actively seeks out, while ignoring or underestimating evidence that may refute their claims.

In order to prevent this behavioral bias, it is suggested that managers avoid focusing too much on the stocks of their subsidiaries, and focus more against negative news and information about their companies. It is also essential to research on competing companies.

Behavioral bias in the second mental model based on anchoring and adjustment, is a psychological process that affects the way people evaluate probabilities. Managers who are exposed to this bias, often act under the influence of upstream rules based on individual preferences. Reasonable managers deal with new information realistically and do not involve predetermined issues such as the product market and the company’s performance in their decisions. However, the anchoring and adjustment bias causes managers to focus on psychological anchor points (tendencies, preferences, and the regulations of the Innovation and Prosperity Fund and the Scientific Vice President) rather than on statistics. In this way, financial decision-making

deviates from the prescribed norms of the "neoclassical school", i.e. “reasonableness".

There is also an overconfidence bias in the second mental model. Overconfident fund managers hold non-diversified portfolios. They do not exceed a certain range of risk and invest in industrial and non-industrial projects within a certain range.

The behavioral bias of the third model can be called hindsight bias. The managers with high risk-taking tendency have the false belief that they have predicted the outcome of an event from the very beginning. This bias affects future predictions. Managers subject to the event bias think that the outcome they see at the end is actually the only outcome that has always been possible. Therefore, they underestimate the uncertainty that exists before the event and underrate the consequences that could have be realized but did not happen. Also, relying too much on the data of evaluators and experts and the high volume of information causes the dilution effect in such a way that irrelevant data overshadows important data and prevents the prioritization of projects.

6 CONCLUSIONS

In this research at first, behavioral economics literature was reviewed. In the second phase, 13 managers of research and technology funds in Tehran and other provinces were interviewed. After detailed investigations and data organization, about 30 statements or phrases were identified; Finally, 17 statements were selected as Q sample. It is worth noting that those statements that were more frequent, or which the interviewees seemed to view at them from different sides or had different points of view, were selected as Q samples. In the next step, to form the Q category, 17 Q cards were designed in such a way that a Q sample statement (phrase) was written on each card. After reading the cards, the participants sorted them according to the given Q chart. The results imply the existence of cognitive and behavioral biases in representativeness, resourcefulness, and confirmation, in the first mental model, and the anchoring and adjustment bias as well as the overconfidence bias in the second mental model. In the third mental model, according to the findings obtained from managers, there are hindsight and data dilution biases. Finally, by providing nudges (suggestions) in the discussion section, an attempt has been made to reduce these biases, and managers can be more efficient and effective in their decisions by being aware of these behavioral biases.

REFERENCES

[1] Hosseini, M. H., Keshavarz, E., Identifying and Ranking of Factors Affecting Organizational Entrepreneurship with The Aim of Corporate Performance Improvement Using Fuzzy AHP Technique (Case: Coil manufacturing industry), Strategic Studies in The Oil and Energy Industry, Vol. 9, No. 36, 2018, pp. 213-242.

[2] Simon Nobre, F., Core Competencies of The New Industrial Organization, Journal of Manufacturing Technology Management, Vol. 22, No. 4, 2011, pp. 422-443. https://doi.org/10.1108/17410381111126391.

[3] Roger David Hall, C. A., Leadership Development for Managers in Turbulent Times, Journal of Management Development, 2016, pp. 942-955.

[4] Almgren, H., Start-up of advanced manufacturing systems – a case study", Integrated Manufacturing Systems, Vol. 10, No. 3, 1999, pp. 126-136. https://doi.org/10.1108/09576069910264385.

[5] Hatch, M. J., Organization Theory Modern, Symbolic, and Postmodern Perspectives, 2013.

[6] Aslani et al., Examining the Role of Mental Models in The Process of Organizational Change (Case Study of Isfahan Medical Records Investigating Office), Management Sciences Quarterly, No. 7, 2021, pp. 174-189.

[7] Salsabil, et al., Explaining the Consumer Decision-Making Model, based on Cognitive and Behavioral Sciences Using Meta-Combination Method, No. 2, 2022, pp. 88-109.

[8] Malekzadeh, Rahimnia, Mental Patterns of Iranian Knowledge Based Enterprises Manager’s about Meaningful Work: Application of Q Methodology. Scientific-Research Quarterly of Management Studies, 2016, pp. 81, 1-24.

[9] Sarboland, Understanding the Role of Managers' Mental Patterns in Innovative Work Behavior in Public Organizations Using Technique, Knowledge & Research in Applied Psychology, Vol. 22, No. 1, 2021, pp. 43-54.

[10] Askarifar, K., Determining the Mental Model of Iranian Entrepreneurs in Securing Business Start-Up Capital, International Conference on Management and Entrepreneurship, Shiraz University, Shiraz, Tehran, 2015, pp. 1-18.

[11] Nasehi Far, V., Saeedi, S., Presenting the Mental Model of Entrepreneurs in Preparing a Sustainable Business Model, First International Conference on Industrial Marketing Management, Allameh Tabatabaei University, Tehran, Iran, 2021.

[12] Pourezzati, A. A., Ghlipour, A., and Nadirkhanlou, S., Explaining the barriers to academic entrepreneurship and commercialization of knowledge in Tehran University, Science and Technology Policy - Quarterly, Vol. 2, No. 4, 2010, pp. 65-75.

Int. J. Advanced Design and Manufacturing Technology, 2025, Vol. 18, No. 4, pp. 41-47

DOI: ***ISSN: 2252-0406*** ***https://admt.isfahan.iau.ir***

Design and Simulation of a Jumping Quadruped Robot with Torsional Spring Joints

Mehrdad Naghsh Nilchi, Mohammad Saadat *, Ali Soleimani, Meisam Vahabi, Mehdi Salehi

Department of Mechanical Engineering, Najafabad Branch, Islamic Azad University, Najafabad, Iran,
E-mail: mhdnilchi@yahoo.com, saadat@pmc.iaun.ac.ir, soleimani@pmc.iaun.ac.ir, Vahabi.meisam@gmail.com, mehdi.salehi@pmc.iaun.ac.ir
*Corresponding author

Received: 1 June 2025, Revised: 3 July 2025, Accepted: 14 August 2025

Abstract: Many animals utilize jumping as a means of traversing uneven terrain in nature. Animal jumping enables them to overcome obstacles that exceed their body size. Today, there is a clear need for mobile robots that can perform human missions in complex environments instead of humans. Performing these tasks by humans is either risky or costly. Legged robots are more capable of performing missions than wheeled robots. The mechanism of these robots allows them to traverse inaccessible surfaces. In this paper, a two-dimensional, four-legged robot model is introduced. In the next step, the four-legged robot and the walking path are simulated using Adam's software. All the physical properties of the four-legged robot, as well as parameters related to jumping, are inputted into the software. Following that, the simulated model is implemented in Adam's software, and the four-legged robot jumps on the stairs. The Adams software is used to review jumping path diagrams, robot joint changes, and contact forces. The deformation diagram of the robot's torsion springs for the rear and front legs of the robot showed the same behavior, which showed the accuracy of the simulation. Also, for better analysis, the contact force diagram of the robot's legs was also examined, which showed the simultaneous impact of the rear legs on the step and the front legs on the steps in the diagram.

Keywords: Quadruped Robot, Robot Energy Consumption, Robot Jump, Stairs

Biographical notes: Mehrdad Naghsh Nilchi is a PhD student of Mechanical Engineering from Najaf Abad University. His current research focuses on robotics, optimization and robot jumping. **Mohammad Saadat** is an Assistant Professor of Mechanical Engineering at Najaf Abad University, Iran. His current research interest includes robotics. **Ali Soleimani** is an Assistant Professor of Mechanical Engineering at Najaf Abad University, Iran. His current research interests include Dynamic and control systems. **Meisam Vahabi** is an Assistant Professor of Mechanical Engineering at Najaf Abad University, Iran. His current research interest includes robotics. **Mehdi Salehi** is an Associate Professor of Mechanical Engineering at Najaf Abad University, Iran.

Research paper

1 INTRODUCTION

Robots have always been a preferred solution for addressing movement challenges in unstructured environments. Legged robots offer several advantages over wheeled and tracked robots, although they also come with increased complexity. This complexity arises not only from the mechanism used but also from electronic systems, sensory capabilities, and control algorithms. Numerous studies have been conducted in the field of four-legged robots, which exhibit significant flexibility in their movement. In general, legged robots surpass other mobile robots in their ability to navigate complex environments [1].

Researchers have focused explicitly on designing robots capable of crossing obstacles like stairs. Through various designs and control systems, several robots have demonstrated successful stair-climbing capabilities. Examples include two-legged robots like Cassie [2] and ASIMO [3], as well as four-legged robots like HyQ [4], Anymal [5], MIT Cheetah [6], Pegasus [7], Jueying [8], and Scalf [9]. Furthermore, robots such as THU-QUAD II [10], ALPHRED [11], and Qingzhui [12] have utilized six-legged configurations.

Li et al [13] devised dimension-based designs to enhance the stair-climbing ability of a six-legged robot, investigating various scenarios while also addressing foot-step mechanism interference. To achieve this, they initially derived the analytical model of the single-leg mechanism based on step size.

The belt base mechanism is frequently employed in six-legged robots. Additionally, stability [14-15] is a crucial concern during stair climbing. Liu et al [16] explored the behavior of a defective leg on a ramp in a six-legged robot. In the meantime, four-legged robots have lower computational and economic costs than six-legged or eight-legged types and can ensure the stability of the robot. Robots are very capable of helping COVID-19 patients. Naghsh Nilchi et al. [17] presented a six-legged robot that was able to find a suitable method to help the medical staff and COVID-19 patients. They simulated a robot that can easily walk and cross the unevenness in front of it, and provide services to COVID-19 patients. Coelho et al. [18] examined the six-legged robot in CoppeliaSim software. By using the control system defined for the robot, they managed to make the robot pass through several types of uneven surfaces. On the other hand, legged robots face many challenges in order to be widely used in various cases. Some of these challenges are the design of stepping mechanisms [19], choosing the appropriate stepping mechanism [20-21], designing the stepping pattern [22-23], stability and balance of the robot [24-25], increasing the speed of stepping [26-27], passing or moving away from obstacles [28-29], planning the sequence of steps [30-31], and planning the movement path to the target point [32-33].

In nature, all creatures utilize their muscle-equipped movement organs to execute jumps. By contracting their muscles, they propel themselves into the air, storing and subsequently releasing energy. In this paper, the Dinavit-Hartenberg matrix and Jacobian matrix associated with the four-legged robot were determined based on available parameters. Subsequently, a simulation of the four-legged robot's stair jump was performed. For this simulation, all springs and joints were designed to enable successful jumps from the stairs. By compressing and releasing the stored force within the springs, the robot was propelled and landed on the stairs. After the simulation, all relevant diagrams were obtained from the Adams software for analysis and evaluation. Finally, an optimization process was undertaken, resulting in the best outcomes for this research project.

2 FOUR-LEGGED ROBOT MODELING

To mimic the jumping ability observed in animals, it is necessary to define joints for the robot. In nature, animals possess multiple muscles within their joints that facilitate jumping. Figure 1 illustrates the two-dimensional model of the four-legged robot. In this study, torsion springs are utilized in each joint of the four-legged robot to emulate the function of muscles.

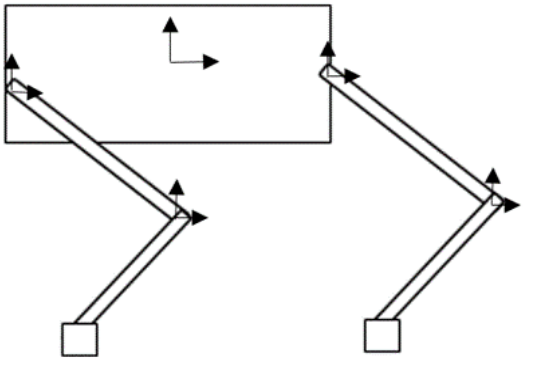

Fig. 1 Two-dimensional model of four-legged robot.

As we know, configuration variables are [16]:

$$Q=[x;z;q_{pitch};q] \quad (1)$$

In "Eq. (1)", x and z represent the COM (center of mass) position of the robot, q_{pitch} is the body pitch angle in the world frame, and q is the joint angle vector that includes the hip and knee joint angles of the front and back legs [16]. By using space vector algebra [17], the dynamic equations of the robot can be derived [16]:

$$H(Q)\ddot{Q}+C(Q,\dot{Q})\dot{Q}+g(Q)=B\tau+B_{fric}+\tau_{fric}(\dot{Q})+\sum_i J_i^T(Q)F_i \quad (2)$$

In "Eq. (2)", H denotes the mass matrix, and the matrix C contains the Coriolis and centrifugal terms. Additionally, g represents the gravity vector, J_i is the spatial Jacobian of the body containing the i^{th} foot expressed at the foot and in the world coordinate system, F_i is the spatial force at the i^{th} foot, and matrices B and B_{fric} define how the actuator torques τ and the joint friction torques τ_{fric} are incorporated into the model [29]. To obtain the kinematics of the robot, it is necessary to define the movement of the body in space and the corresponding generalized coordinates. For this purpose, the Denavit-Hartenberg (DH) matrix is employed. The reference variables for the legs of the four-legged robot are shown in Figure 2.

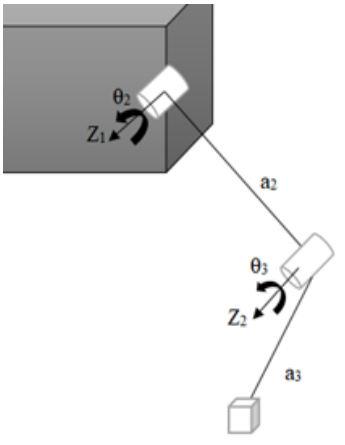

Fig. 2 Reference variables for four-legged robot legs.

The parameters of the DH matrix are listed in "Table 1". It is important to note that each leg of the four-legged robot in this paper has three degrees of freedom**.**
On the other hand, the DH matrix for the i^{th} joint is ($s_i=\sin(\theta_i)$ and $c_i=\cos(\theta_i)$):

$$A_i^{i-1}=\begin{bmatrix} c\theta_i & -s\theta_i c\alpha_i & s\theta_i s\alpha_i & a_i c\theta_i \\ s\theta_i & c\theta_i c\alpha_i & -c\theta_i s\alpha_i & a_i s\theta_i \\ 0 & s\alpha_i & -c\theta_i s\alpha_i & d_i \\ 0 & 0 & 0 & 1 \end{bmatrix} \quad (3)$$

Table 1 DH parameters for legs

.1 ink	a_i .2	.3 $_i$	α .4 $_i$	θ .5 $_i$
.6	a_1 .7	.8	0 .9	θ .10 $_1$
.11	a_2 .12	.13	0 .14	θ .15 $_2$

So the DH matrix of each joints is:

$$A_1^0=\begin{bmatrix} c_1 & -s_1 & 0 & a_1c_1 \\ s_1 & c_1 & 0 & a_1s_1 \\ 0 & 0 & 1 & 0 \\ 0 & 0 & 0 & 1 \end{bmatrix} \quad (4)$$

$$A_2^1=\begin{bmatrix} c_2 & -s_2 & 0 & a_2c_2 \\ s_2 & c_2 & 0 & a_2s_2 \\ 0 & 0 & 1 & 0 \\ 0 & 0 & 0 & 1 \end{bmatrix} \quad (5)$$

Also, the Jacobian matrix of the leg is [32]:

$$J(q)=\begin{bmatrix} Z_0\times(p-p_0) & Z_1\times(p-p_1) \\ z_0 & z_1 \end{bmatrix} \quad (6)$$

In "Eq. (5)", z_0, z_1, and z_2 represent the joint axes, while p_0, p_1, and p_2 are joint position vectors, and p is the foot position vector. The submatrices of the Jacobian matrix can be found in Equations (6) and (7):

$$J(\theta_1)=\begin{bmatrix} -a_1s_1-a_2s_{12} \\ a_1c_1+a_2c_{12} \\ 0 \\ 0 \\ 0 \\ 1 \end{bmatrix} \quad (7)$$

$$J(\theta_2)=\begin{bmatrix} -a_2s_{12} \\ a_2c_{12} \\ 0 \\ 0 \\ 0 \\ 1 \end{bmatrix} \quad (8)$$

3 FOUR-LEGGED ROBOT JUMPING SIMULATION

To simulate the jumping of a four-legged robot on the stairs, the dimensions of the robot, including the dimensions of the legs and the body, need to be determined. Similarly, the dimensions of the stairs also need to be determined. "Table 2" presents the dimensions of the simulated robot, and "Fig. 3" illustrates the dimensions of the stairs.

Table 2 The dimensions of the four-legged robot

Parameter .16	Value .17
Four-legged robot body dimensions .18	(20cm× 20cm×50cm) .19
Hip of the four-legged robot .20	(12.5cm ×4cm) .21
Knee of the four-legged robot .22	(12.5cm ×4cm) .23
Ankle of the four-legged robot .24	(7cm×6. 5cm×4cm) .25
The total mass of the robot .26	32.6 (kg) .27

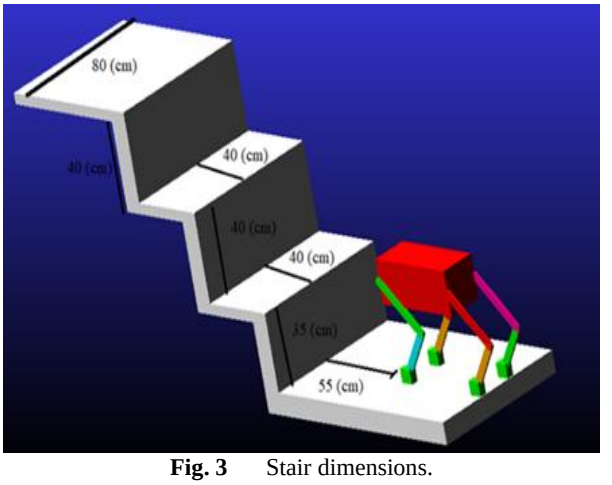

Fig. 3 Stair dimensions.

As mentioned, springs are used to mimic the muscles of the robot during the jumping process. The compression of these springs allows energy to be stored and released, propelling the robot forward. In this research, torsional springs were utilized in the joints, as shown in "Fig. 4".

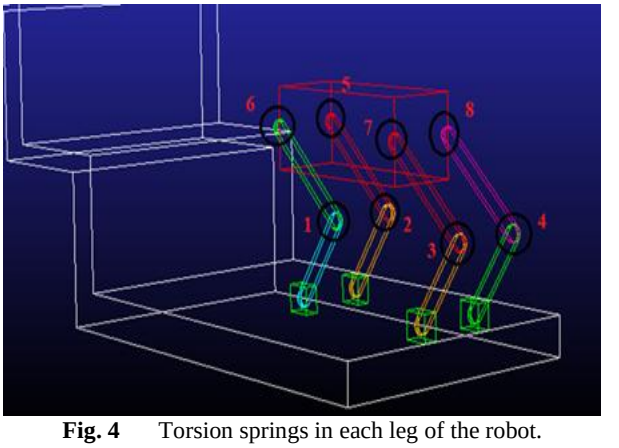

Fig. 4 Torsion springs in each leg of the robot.

The stiffness values of these torsional springs are provided in "Table 3". Additionally, it should be noted that the damper coefficient for all joints is set to 10000 (Newton-mm-sec/deg).

Table 3 Stiffness value torsional spring

Spring .28	Stiffness value (Newton-mm/deg) .29
1 .30	7000 .31
2 .32	7000 .33
3 .34	7000 .35
4 .36	7000 .37
5 .38	2000 .39
6 .40	2000 .41
7 .42	2000 .43
8 .44	2000 .45

Once all the contact conditions between the legs of the four-legged robot and the stairs are applied, the software initiates the simulation. As seen in "Fig. 5", the four-legged robot begins to jump after running the simulation using Adam's software.

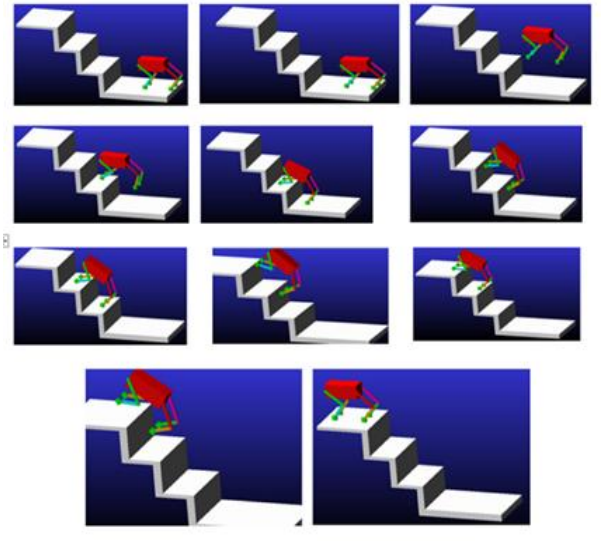

Fig. 5 Four-legged robot jumping on the stairs.

By exerting force on its legs, the four-legged robot generates the necessary energy to jump and land on the first step. Subsequently, it prepares itself to jump onto the second step by turning a small angle. This process continues until the four-legged robot successfully reaches the upper terrace through a series of jumps.

4 CONCLUSIONS

After simulating Adam's software, the results of the four-legged robot's jumping on the mineral stairs are analyzed and evaluated using relevant diagrams. Figure 6 displays the position of the robot's center of mass along the y-axis. This helps understand the robot's movement during jumping.

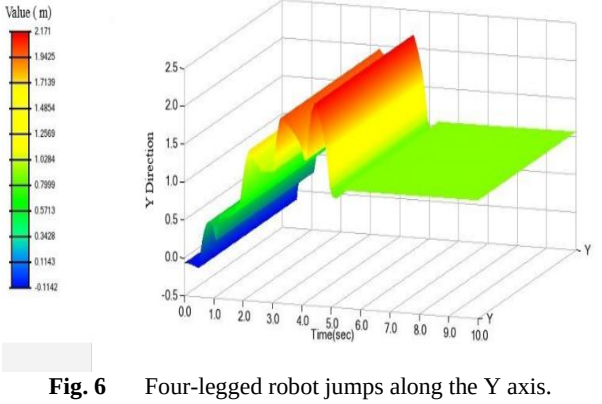

Fig. 6 Four-legged robot jumps along the Y axis.

The deformation of the torsional springs in the knee joints is an important aspect to analyse the jumping behaviour of the robot on the stairs. Figure 7 illustrates the deformation of the knee joint torsional springs. Additionally, there are four torsion springs in the hip part of the robot, and "Fig. 8" shows the deformation of these hip joint torsional springs.

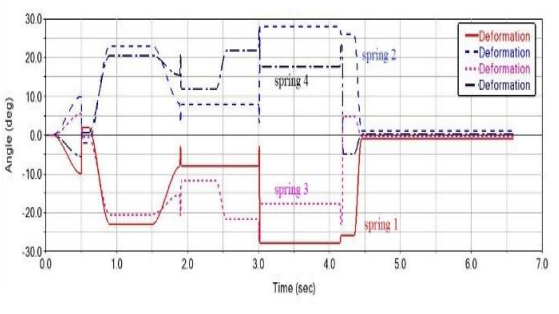

Fig. 7 The deformation of the torsional spring in the knee joint.

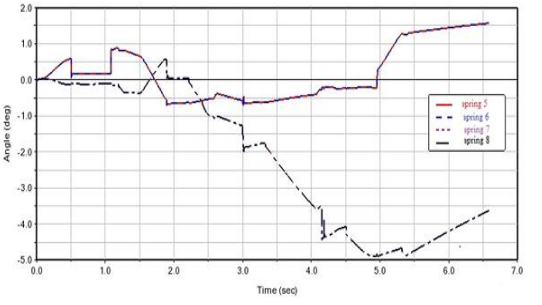

Fig. 8 The deformation of the torsional spring in the hip joint.

Based on "Fig. 7", springs 3 and 4 (back legs of the quadruped robot) exhibit similar behavior, while springs 1 and 2 (front legs of the robot) demonstrate a similar pattern at different times. This highlights the significance of the front legs in the jumping and landing process when the robot jumps on the stairs.

According to "Fig. 8", springs 5 and 6 (front legs of the quadruped robot) and springs 7 and 8 (rear legs of the robot) display similar behavior at different times. Furthermore, the rear legs of the four-legged robot undergo greater changes in angle compared to the front legs. In general, during the jumping of the four-legged robot on the stairs, the rear legs experience more significant angle changes.

The impact of the robot's feet on the surface of the stairs is another crucial aspect of the jumping process. The contact between the robot's legs and the stair surface is carefully analyzed. This is depicted in "Fig. 9", where the surfaces between the robot's legs are defined as step surfaces in the modeling process using Adam's software. "CONTACT" constraints are utilized to define these surfaces.

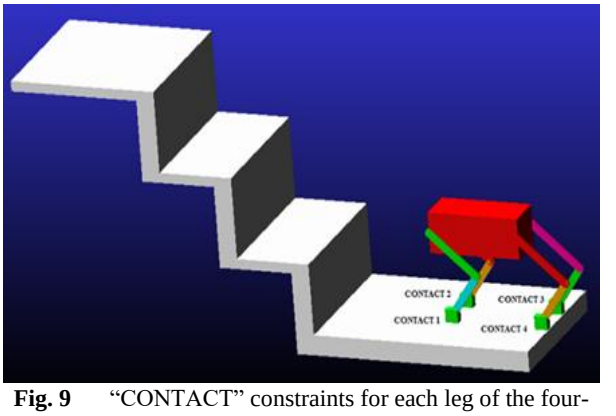

Fig. 9 "CONTACT" constraints for each leg of the four-legged robot.

To gain a better understanding of the contact forces between the four-legged robot's legs and the stairs, a contact force diagram is provided in "Fig. 10".

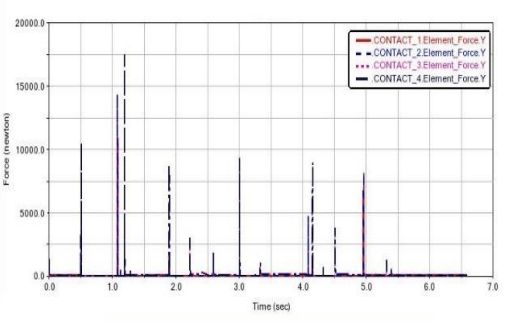

Fig. 10 Contact force diagram of the robot's legs.

All the contact lines in the diagram coincide with each other. This indicates that when the four-legged robot jumps and lands on the stairs, all legs of the robot are simultaneously separated from the ground and land on the stairs together.

The four-legged robot modeled in this paper can be considered as the best model for jumping on the stairs. Additionally, this robot has the ability to jump up to a certain height over other obstacles. Based on the relationships obtained and the simulation of the four-legged robot in this article, future research can focus on the robot's ability to perform jumps on the path of the mineral stairs while carrying weight. Moreover, a potential area of investigation for future research could involve the four-legged robot jumping with a defective leg, utilizing the model presented in this paper.

REFERENCES

[1] Zaitsev, V., Gvirsman, O., Hanan, U. B., Weiss, A., Ayali, A., and Kosa, G., A Locust-Inspired Miniature Jumping Robot, Bioinspiration & Biomimetics, Vol. 10, No. 6, 2015, pp. 066012. DOI: http://dx.doi.org/10.1088/1748-3190/10/6/066012.

[2] Hereid, A., Harib, O., Hartley, R., Gong, Y., and Grizzle, J. W., Rapid Trajectory Optimization Using C-Frost with Illustration on A Cassie-Series Dynamic Walking Biped, In 2019 IEEE/RSJ International Conference on Intelligent Robots and Systems (IROS), 2019, pp. 4722-4729.

[3] Chestnutt, J., Lau, M., Cheung, G., Kuffner, J., Hodgins, J., and Kanade, T., Footstep Planning for The Tili Asimo Humanoid, In Proceedings of the 2005 IEEE International Conference on Robotics and Automation, 2025, pp. 629-634

[4] Chestnutt, J., Lau, M., Cheung, G., Kuffner, J., Hodgins, J., and Kanade, T., Footstep Planning for The Tili Asimo Humanoid, In Proceedings of the 2005 IEEE International Conference on Robotics and Automation, 2005, pp. 629-634.

[5] Chestnutt, J., Lau, M., Cheung, G., Kuffner, J., Hodgins, J., and Kanade, T., Footstep Planning for The Tili Asimo Humanoid, In Proceedings of the 2005 IEEE International Conference on Robotics and Automation, 2005, pp. 629-634.

[6] Bledt, G., Powell, M. J., Katz, B., Di Carlo, J., Wensing, P. M., and Kim, S., MIT Cheetah 3: Design and Control of a Robust, Dynamic Quadruped Robot, In 2018 IEEE/RSJ International Conference on Intelligent Robots and Systems (IROS), 2018, pp. 2245-2252.

[7] Liao, T., Ye, S., Chen, L., Sun, C., and Zhang, A., Energy Efficient Swing Leg Trajectory Planning for Quadruped Robots Walking on Rough Terrain, In 2019 IEEE International Conference on Robotics and Biomimetics (ROBIO), 2019, pp. 2128-2133.

[8] Mc Guire, K. N., De Wagter, C., Tuyls, K., Kappen, H. J., and De Croon, G. C., Minimal Navigation Solution for A Swarm of Tiny Flying Robots to Explore an Unknown Environment, Science Robotics, Vol. 4, No. 35, 2019, pp. 9710.

[9] Zhang, G., Rong, X., Hui, C., Li, Y., and Li, B., Torso Motion Control and Toe Trajectory Generation of a Trotting Quadruped Robot Based on Virtual Model Control, Advanced Robotics, Vol. 30, No. 4, 2016, pp. 284-97.

[10] Ye, L., Liu, H., Wang, X., Liang, B., and Yuan, B., Multi-Task Control for a Quadruped Robot with Changeable Leg Configuration, In 2020 IEEE/RSJ International Conference on Intelligent Robots and Systems (IROS), 2020, pp. 3944-3950.

[11] Ahn, M. S., Chae, H., and Hong, D. W., Stable, Autonomous, Unknown Terrain Locomotion for Quadrupeds Based on Visual Feedback and Mixed-Integer Convex Optimization, In 2018 IEEE/RSJ International Conference on Intelligent Robots and Systems (IROS), 2018, pp. 3791-3798.

[12] Mao, L., Gao, F., Tian, Y., and Zhao, Y., Novel Method for Preventing Shin-Collisions in Six-Legged Robots by Tilizing a Robot–Terrain Interference Model, Mechanism and Machine Theory, Vol. 151, 2020, pp. 103897.

[13] Li, H., Qi, C., Mao, L., Zhao, Y., Chen, X., and Gao, F., Staircase-Climbing Capability-Based Dimension Design of a Hexapod Robot, Mechanism and Machine Theory, Vol. 164, 2021, pp. 104400.

[14] Rastgar, H., Naeimi, H. R., and Agheli, M., Characterization, Validation, And Stability Analysis of Maximized Reachable Workspace of Radially Symmetric Hexapod Machines. Mechanism and Machine Theory, 2019, pp. 315-35.

[15] Mummolo, C., Mangialardi, L., and Kim, J. H., Numerical Estimation of Balanced and Falling States for Constrained Legged Systems, Journal of Nonlinear Science, Vol. 4, 2017, pp. 1291-323.

[16] Liu, Tao, et al. Hexapod Robot Fault Tolerant Gait on Slope and Simulation Verification, Journal of Physics: Conference Series, Vol. 1601, No. 6. IOP Publishing, 2020.

[17] M. Nagsh Nilchi, Saadat, M., Improving the Movement Path of a Six-Legged Robot in A Rough Environment in Order to Serve Corona Patients, The Second National Conference on Health Knowledge Production and Governance in the Post-Corona World, 2022.

[18] Coelho, J., Sá, R., Ribeiro, T., Ribeiro, F., Dias, B., Lopes, G., and Flores, P., Study of the Locomotion of a Hexapod Using CoppeliaSim and ROS, International

Conference on Computers and Automation (CompAuto), 2021, PP. 109-116.
[19] Ding, L., Gao, H., Deng, Z., Song, J., Liu, Y., Liu, G., and Iagnemma, K., Foot–Terrain Interaction Mechanics for Legged Robots: Modeling and Experimental Validation, The International Journal of Robotics Research, 2013, pp. 1585-1606.
[20] Zhang, T., Wei, Q., Ma, H., Position/Force Control for A Single Leg of a Quadruped Robot in An Operation Space, International, Journal of Advanced Robotic Systems, 2013, pp. 137.
[21] Zhu, Y., Jin, B., Compliance Control of a Legged Robot Based on Improved Adaptive Control: Method and Experiments, Int. J. Robot, 2016, pp. 366-373.
[22] Luneckas, M., Luneckas, T., Udris, D., Plonis, D., Maskeliunas, R., and Damasevicius, R., Energy-Efficient Walking Over Irregular Terrain: A Case of Hexapod Robot, Metrology and Measurement Systems, 2019.
[23] Zhang, S., Xing, Y., and Hu, Y., Composite Gait Optimization Method for A Multi-Legged Robot Based on Optimal Energy Consumption, Chinese Space Science and Technology, 2018.
[24] Zhang, L., Zhou, C., Optimal Three-Dimensional Biped Walking Pattern Generation Based on Geodesics, International Journal of Advanced Robotic Systems, 2017, 729881417696235.
[25] Li, M., Wang, X., Guo, W., Wang, p., and Sun, L., System Design of a Cheetah Robot Toward Ultra-High Speed, International Journal of Advanced Robotic Systems, 2014, pp. 73.
[26] Zhang, S., Liu, M., Yin, Y., Rong, X., Li, Y., and Hua, Z., Static Gait Planning Method for Quadruped Robot Walking on Unknown Rough Terrain, IEEE Access, 2019, pp. 177651-177660.
[27] Spröwitz, A. Tuleu, A., Vespignani, M., Ajallooeian, M., Badri, E., and Ijspeert, A., Towards Dynamic Trot Gait Locomotion: Design, Control, And Experiments with Cheetah-Cub, A Compliant Quadruped Robot, The International Journal of Robotics Research, 2013, pp. 935-950.
[28] Xin, Y., Liang, H., Mei, T., Huang, R., Chen, L., Zhao, P., Sun, C., and Wu. Y., A New Dynamic Obstacle Collision Avoidance System for Autonomous Vehicles. International Journal of Robotics & Automation, Vol. 30, No. 3, 2015.
[29] Luneckas, M., Luneckas, T., Udris, D., Plonis, D., Maskeliūnas, R., and Damaševičius, R., A Hybrid Tactile Sensor-Based Obstacle Overcoming Method for Hexapod Walking Robots, Intelligent Service Robotics, Vol. 202, pp. 9-24.
[30] Chen, J., Gao, F., Huang, C., and Zhao, J., Whole-Body Motion Planning for A Six-Legged Robot Walking on Rugged Terrain, Applied Sciences, Vol. 9, No. 24, 2019, pp. 5284.
[31] Boscariol, P., Richiedei, D., Optimization of Motion Planning and Control for Automatic Machines, Robots and Multibody Systems, Applied Sciences, Vol. 10, No. 14, 2020, pp. 4982.
[32] Gasparetto, A., Boscariol, P., Lanzutti, A., and Vidoni, R., Trajectory Planning in Robotics, Mathematics in Computer Science, Vol. 6, No. 3, 2012, pp. 269-279.
[33] Carabin, G., Scalera, L., On the Trajectory Planning for Energy Efficiency in Industrial Robotic Systems. Robotics, Vol. 9, No. 4, 2020, pp. 89.

Int. J. Advanced Design and Manufacturing Technology, 2025, Vol. 18, No. 4, pp. 49-56

DOI: *ISSN: 2252-0406* *https://admt.isfahan.iau.ir*

Analysis of Machining Parameters Influencing Thrust Force in Drilling of Carbon Dot Nanoparticle-Reinforced Epoxy Matrix Composites

Mohammad Baraheni *, Mahan Karkhaneh, Erfan Agha Bagheri

Manufacturing Engineering Department, Arak University of Technology, Arak, Iran

E-mail: mbaraheni@arakut.ac.ir, Mahan@gmail.com, aghabagheri@gmail.com

*Corresponding author

Received: 29 May 2025, Revised: 14 July 2025, Accepted: 2 August 2025

Abstract: Epoxy matrix composites reinforced with carbon dot nanoparticles are increasingly utilized in industries due to their enhanced mechanical, thermal, and electrical properties. Drilling, a critical machining process for assembling these composites, often induces defects, such as delamination and stress concentrations, that impact structural integrity. Unlike prior studies that primarily focused on surface quality or delamination in conventional composites, this work systematically investigates the thrust force response in nanomodified epoxy composites reinforced with carbon dot nanoparticles. A full factorial design of experiments was employed, with thrust forces measured using a high-precision load cell. Statistical analysis revealed that drill bit diameter is the dominant factor, contributing 66.18% to thrust force variation, followed by spindle speed (19.90%) and feed rate (7.16%). The regression model, with an R-squared value of 98.90%, captured significant linear and nonlinear parameter interactions. Increasing feed rate and tool diameter elevated drilling forces, while higher spindle speeds slightly reduced them. The incorporation of carbon dots up to 1 wt.% reduced thrust force by enhancing interfacial bonding, although excessive concentrations led to embrittlement. Optimization results identified ideal drilling conditions—spindle speed of 2500 rpm, feed rate of 10 mm/min, drill bit diameter of 0.3 mm, and 1 wt.% carbon dots—achieving a minimum thrust force of 0.0639 N.

Keywords: Carbon-Dot Nanoparticle, Drilling, Statistical Analysis, Optimization, Thrust Force

Biographical notes: **Mohammad Baraheni** received his PhD in Manufacturing Engineering from Kashan University in 2019 and is currently an Assistant Professor in the Manufacturing Engineering Department at Arak University of Technology, Iran. His research interests encompass advanced machining of composite and nanocomposite materials, ultrasonic-assisted machining, and data-driven manufacturing. **Mahan Karkhaneh** is pursuing his MSc in Manufacturing Engineering at Arak University of Technology. **Erfan Agha Bagheri** is an undergraduate student of Manufacturing Engineering at Arak University of Technology.

Research paper

1 INTRODUCTION

Nanotechnology refers to the manipulation and utilization of materials at the nanometer scale (1–100 nm), where their physical and chemical properties may significantly differ from those observed at larger scales [1]. This field has found extensive applications across various disciplines, including medicine, electronics, energy, environmental science, and advanced materials. Epoxy is a thermosetting polymer widely employed in industries such as coatings, adhesives, composites, and electronics due to its superior mechanical, chemical, and thermal properties [2]. These properties can be further enhanced by incorporating nanofillers, such as carbon dots (CDs). CDs are carbon-based nanomaterials with unique optical and electronic characteristics, making them suitable for applications in sensors, solar cells, optoelectronics, and biomedicine. CDs can be synthesized through various methods, including combustion, laser ablation, chemical synthesis, and biological routes [3]. Epoxy/carbon dot nanocomposites are fabricated by dispersing CD nanoparticles within an epoxy matrix. These nanocomposites exhibit enhanced electromagnetic, optical, mechanical, and thermal properties compared to pure epoxy. For instance, the incorporation of CDs can improve electrical conductivity, light absorption, tensile strength, and Young's modulus [4]. However, machining these nanocomposites, particularly drilling, poses challenges including delamination, fiber pull-out, and stress concentration, which can compromise structural integrity. Previous studies have identified delamination as a critical failure mode in carbon fiber-reinforced composites during drilling operations [5-7].

Composite materials are widely recognized for their near-net-shape manufacturing capabilities through molding processes, which allow them to closely match the final part geometry. However, machining operations such as drilling remain essential for assembling composite components, making the analysis of machining parameters critically important in engineering design. Drilling composites is inherently more challenging than machining metals or alloys due to the material's anisotropic nature and susceptibility to machining-induced damage. Over 60% of industrial composite machining involves drilling, driving extensive research into optimizing cutting parameters to reduce thrust forces and improve hole quality [8]. Gao et al. [9] investigated the surface characteristics of machined carbon composites, with Analysis of variance (ANOVA) results highlighting the significant influence of cutting speed. Similarly, Pólachon et al. [10] analyzed the surface topography of drilled carbon fiber composites, noting that increasing feed rates markedly alters surface quality. Tsao et al. [11] conducted drilling experiments on carbon composites using high-speed steel (HSS) drills under varying cutting speeds and feed rates, concluding that both parameters profoundly affect surface roughness. Wang et al. [12] developed a thrust force prediction model for CFRP drilling by focusing on the chisel edge, which significantly contributes to exit delamination. They introduced the novel concept of an azimuth angle to characterize better the contact between the chisel edge and carbon fibers. Modeling a single fiber as a beam on an elastic foundation, they used bending fracture theory to account for material properties, tool geometry, drilling parameters, and ultrasonic vibration effects. Magyar et al. [13] investigated the drilling of basalt fiber-reinforced polymer (BFRP) composites, focusing on the effect of feed rate and cutting speed on thrust force. Using response surface methodology (RSM) and advanced statistical modelling, they developed predictive models based on experimental data. Thrust force was measured during mechanical drilling and processed via FFT-based low-pass filtering. Their models demonstrated high prediction accuracy (96.74% for RSM and 95.01% for advanced models), with the latter also capturing force characteristics with a determination coefficient of 0.68. Results were also compared with those for CFRP composites to highlight performance differences.

The drilling process often leads to matrix cracking, fiber breakage, and delamination—the latter being a critical concern in composite assembly, as it compromises structural integrity and service life. Ramuluet al. [14] attributed delamination to inadequate support of upper plies during drilling and milling. Delamination extent and damage zones are governed by drilling forces and tool geometry, often resulting in irregular hole profiles. Beyond mechanical forces, heat generation during drilling further degrades composite strength. Elevated temperatures induce matrix deterioration and thermal damage, making temperature control a pivotal parameter in the process.

Ying et al. [15] compared three drill types (tungsten carbide, chemical vapor deposition diamond-coated, and multi-edge tools), monitoring thrust force, temperature, and delamination. Results underscored feed rate as the dominant factor influencing thrust forces, while multi-edge tools minimized delamination. Pathak et al. [16] reported that adding 0.3 wt.% graphene oxide to carbon fiber composites increased flexural strength by 60%, modulus by 70%, and interlaminar shear strength by 25%. Moreover, Baraheni et al. [17] conducted a comprehensive study on the drilling of CFRP laminates, evaluating the effects of nano-graphene addition, ultrasonic vibration, tool type, and feed rate on thrust force. Using statistical and machine learning methods along with image processing, they developed predictive models with high accuracy. Their findings showed that feed rate had the most significant effect on thrust force and burr formation. While nano-graphene increased

thrust force due to enhanced rupture resistance, it reduced burr formation. Additionally, ultrasonic vibration and high-cobalt tools significantly improved hole quality by minimizing both thrust force and burr damage. The shift from metals to composites—driven by their high strength-to-weight ratio, near-net-shape production, and minimal machining needs—has revolutionized industries like aerospace and automotive. For instance, passenger aircraft components demand durable, dimensionally stable joints, necessitating optimized machining processes. Recent decades have seen remarkable progress in carbon fiber composite research. Early 21st century, studies focused on cutting parameters and tool geometry, whereas contemporary work explores alternative strategies.

In this study, the thrust force generated during drilling of carbon dot–reinforced epoxy composites was thoroughly analyzed. A detailed statistical analysis was conducted to examine the influence of key machining parameters, including spindle speed, feed rate, and drill bit diameter on drilling performance. These parameters were systematically varied to understand their individual effects on thrust force. The findings aim to provide a comprehensive understanding of the drilling behavior of nanomodified composite materials. This work not only addresses the growing need for precision in composite manufacturing but also opens new avenues for future research on carbon dot enhanced polymer composites.

2 MATERIALS AND METHODS

Epoxy matrix composites reinforced with carbon dot nanoparticles were fabricated for this study. The epoxy resin (ML 506 from Mokarrar company) and hardener were mixed in the manufacturer-recommended ratio under continuous stirring to ensure homogeneity. Carbon dot nanoparticles were synthesized and dispersed into the epoxy resin at a concentration of 1 wt.%, using ultrasonic agitation for 30 minutes to promote uniform dispersion. The mixture was then poured into a pre-designed mold and cured at room temperature for 24 hours, followed by post-curing at 80°C for 2 hours to achieve optimal mechanical properties. After curing, the composite sheets were cut into rectangular samples of dimensions 100 mm × 100 mm × 5 mm using a diamond saw.

Drilling experiments were conducted using a vertical universal milling machine. The manual milling machine used in this experiment is an FP4M model, manufactured by Tabriz Machine Manufacturing Company. All drilling experiments were performed using high-speed steel (HSS) twist drills of varying diameters (“Fig. 1”). A total of 54 drilling tests were carried out based on a full factorial design of experiments (DOE), with three levels for each factor (“Table 1”). The sample of the drilled holes is shown in “Fig. 2”.

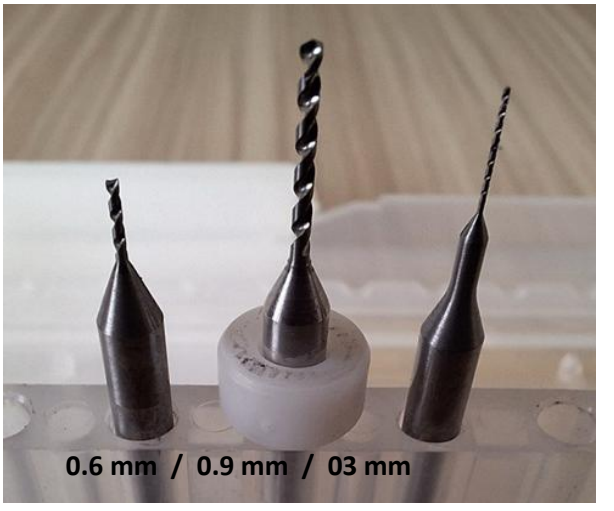

Fig. 2 The used carbide tools.

Table 1 Process factors

Factor	Symbol	Level		
		1	2	3
Spindle speed (rpm)	N	1000	2000	2500
Feed rate (mm/min)	F	10	30	50
Tool diameter (mm)	D	0.3	0.6	0.9
Carbon dot (%)	C	0	1	-

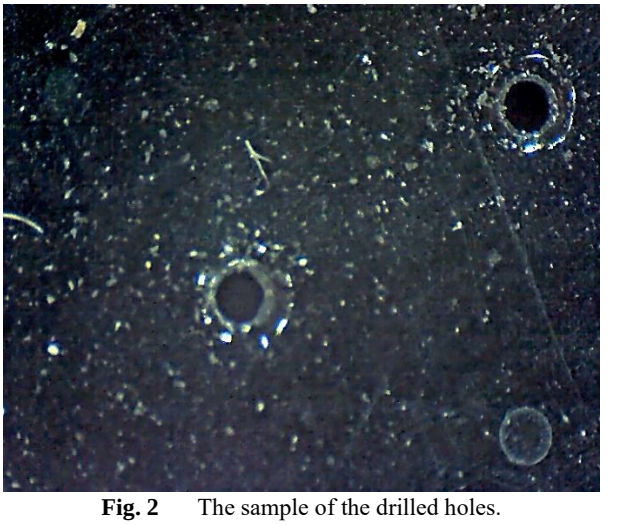

Fig. 2 The sample of the drilled holes.

Drilling experiments were conducted using a vertical universal milling machine (FP4M model, manufactured by Tabriz Machine Manufacturing Company). High-speed steel (HSS) twist drills were used throughout the experiments (“Fig. 1”). A total of 54 drilling tests were carried out based on a full factorial DOE, with three levels for each factor (“Table 1”). The drilling process was performed under dry conditions without the use of coolant to avoid altering the mechanical properties of the

epoxy matrix or introducing additional variables related to coolant interaction with the composite. The specimens were rigidly clamped using a custom fixture with a clamping force of approximately 500 N to ensure stability and minimize vibration during drilling, which could affect thrust force measurements or induce machining defects such as delamination. The clamping force was monitored using a torque wrench to maintain consistency across all experiments.

The thrust force during drilling was measured using a loadcell (manufactured by SEWHA). The used load cell is capable of measuring forces ranging from 1 to 200 kgs, an accuracy of ±0.1% of full scale (equivalent to ±0.2 kg), and a sampling rate of 1000 Hz, enabling precise capture of dynamic force variations during drilling. It has an IP67 protection rating, indicating resistance to water and dust ingress. The device is primarily used for both tensile and compressive force applications. The recommended operating voltage for this load cell is 10 volts. The loadcell is connected to a data acquisition system. Force signals were recorded in real-time, and the peak thrust force for each trial was extracted for analysis. The setup ensured rigid clamping of the specimen to minimize vibration and displacement during drilling ("Fig. 3").

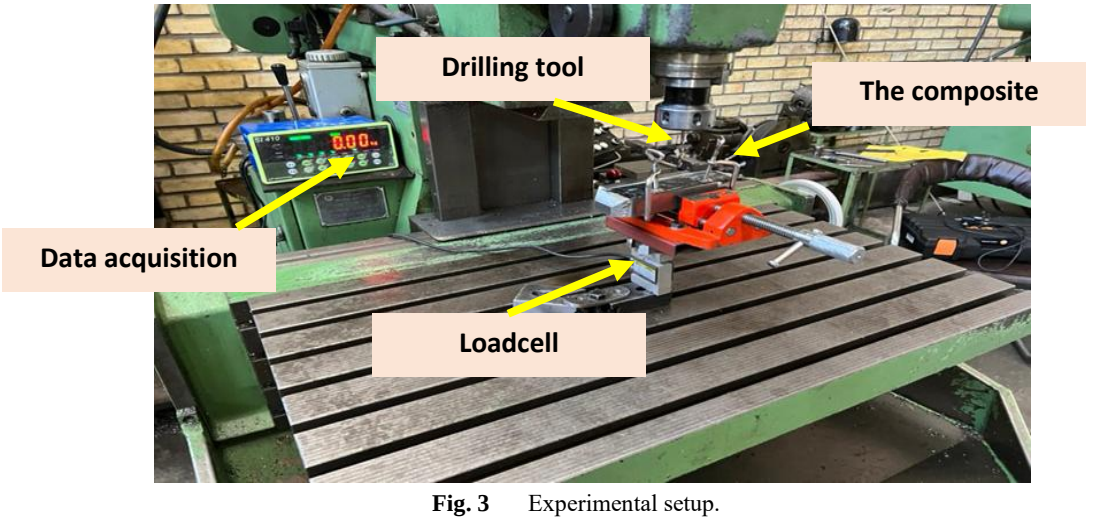

Fig. 3 Experimental setup.

3 RESULTS AND DISCUSSION

This section presents the experimental results and statistical analyses performed on the drilling process of carbon dot–reinforced epoxy composites. It focuses on quantifying how the machining parameters—spindle speed, feed rate, drill bit diameter, and their interactions—affect the maximum thrust force during drilling. The following details the model performance, main effects, and analysis of variance.

3.1. Model Performance and Regression Analysis

The developed regression model ("Eq. (1)") demonstrated excellent predictive capability, with an R-squared value of 98.90% and an adjusted R-squared of 98.55%. The low standard error (S = 0.0077351) and the high predicted R-squared value (97.84%) further confirm the robustness of the model. The regression equation obtained is as "Eq. (1)":

Thrust force = 0.0654 - 0.000054 N + 0.002106 F + 0.1857 D + 0.01020 M - 0.000015 F*F + 0.0926 D*D - 0.000048 N*D + 0.000004 N*M + 0.001042 F*D + 0.000139 F*M - 0.05926 D*M (1)

This comprehensive model illustrates both the linear and nonlinear effects of the drilling parameters, indicating that each factor, as well as their combined interactions, plays a significant role in determining the maximum thrust force.

3. 3.2. Main Effects and Interaction Contributions

ANOVA results, presented in "Table 2", provide a detailed statistical evaluation of the factors influencing the thrust force during the drilling of carbon dot-reinforced epoxy composites. The table summarizes the contribution of each machining parameter—spindle speed, feed rate, drill bit diameter, and material (carbon dot reinforcement level)—along with their quadratic and interaction effects on the maximum thrust force. The ANOVA was conducted using Minitab software, based on a full factorial DOE with 54 trials, ensuring a robust assessment of the model's significance and the individual effects of the parameters. The overall regression model is highly significant, as indicated by an F-value of 277.46 and a p-value less than 0.001, confirming that the model effectively explains the variability in thrust force. The model accounts for 98.90% of the total variation (Contribution), with an R-

squared value of 98.90% and an adjusted R-squared of 98.55%, underscoring its predictive accuracy. The low standard error (S = 0.0077351) further validates the model's precision.

Table 2 ANOVA results of thrust force

Source	DF*	Seq SS*	Contribution	Adj SS*	Adj MS*	F-Value	P-Value
Regression	13	0.215807	98.90%	0.215807	0.016601	277.46	0.000
Spindle	1	0.043430	19.90%	0.000636	0.000636	10.63	0.002
Feed	1	0.015625	7.16%	0.001464	0.001464	24.46	0.000
Diameter	1	0.144400	66.18%	0.001801	0.001801	30.10	0.000
Material	1	0.002400	1.10%	0.000074	0.000074	1.23	0.273
Spindle*Spindle	1	0.000604	0.28%	0.000604	0.000604	10.09	0.003
Feed*Feed	1	0.000408	0.19%	0.000408	0.000408	6.82	0.013
Diameter*Diameter	1	0.000833	0.38%	0.000833	0.000833	13.93	0.001
Spindle*Feed	1	0.001302	0.60%	0.001302	0.001302	21.76	0.000
Spindle*Diameter	1	0.002857	1.31%	0.002857	0.002857	47.75	0.000
Spindle*Material	1	0.000096	0.04%	0.000096	0.000096	1.61	0.212
Feed*Diameter	1	0.000937	0.43%	0.000937	0.000937	15.67	0.000
Feed*Material	1	0.000069	0.03%	0.000069	0.000069	1.16	0.288
Diameter*Material	1	0.002844	1.30%	0.002844	0.002844	47.54	0.000
Error	40	0.002393	1.10%	0.002393	0.000060		
Total	53	0.218200	100.00%				

DF: Degrees of Freedom, Seq SS: Sequential Sum of Squares, Adj SS: Adjusted Sum of Squares, Adj MS: Adjusted Mean of Squares.

Among the main effects, drill bit diameter is the dominant factor, contributing 66.18% to the thrust force variation, followed by spindle speed (19.90%) and feed rate (7.16%). The material factor, representing carbon dot reinforcement, has a minimal direct effect (1.10%, $p = 0.273$), but its interactions with other parameters are significant. Quadratic effects, such as those for spindle speed (0.28%, $p = 0.003$), feed rate (0.19%, $p = 0.013$), and diameter (0.38%, $p = 0.001$), indicate nonlinear relationships that influence thrust force. Key interaction effects include spindle speed × diameter (1.31%, $F = 47.75$, $p < 0.001$) and diameter × material (1.30%, $F = 47.54$, $p < 0.001$), highlighting that the impact of one parameter often depends on the level of another. The error term, contributing only 1.10% to the total variation, suggests that unaccounted factors have a negligible impact, reinforcing the model's robustness.

The ANOVA results provide critical insights into the relative importance of each parameter and their interactions, guiding the optimization of drilling processes for carbon dot-reinforced epoxy composites. The significant contributions of drill bit diameter and its interactions underscore the need for careful tool selection, while the nonlinear and interaction effects emphasize the importance of balanced parameter settings to minimize thrust forces and machining-induced damage.

3.3. Main effects plot

The main effects plot ("Fig. 4") provides a comprehensive visual representation of the relationships between the drilling parameters—spindle speed, feed rate, drill bit diameter, and carbon dot reinforcement level—and the resultant thrust force during the drilling of carbon dot-reinforced epoxy composites.

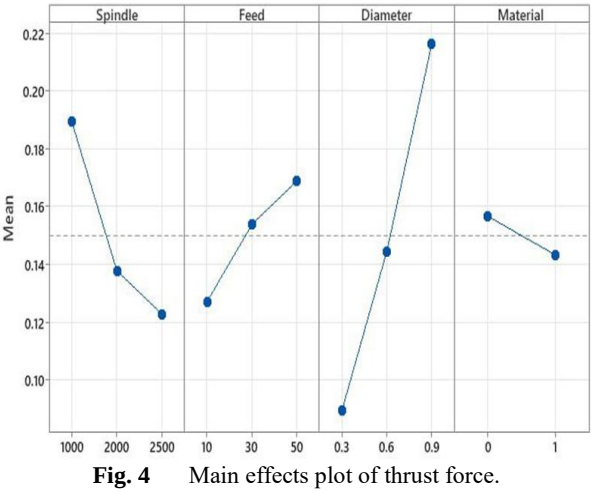

Fig. 4 Main effects plot of thrust force.

These relationships, derived from a full factorial DOE and analyzed using Minitab software, offer critical insights into the mechanical behavior of the composite under varying machining conditions. The following discussion elaborates on the observed trends, their underlying mechanisms, and their implications for optimizing the drilling process.

For spindle speed, the regression model reveals a negative coefficient, indicating that an increase in spindle speed (from 1000 to 2500 rpm) results in a slight reduction in thrust force. This trend can be attributed to the enhanced cutting efficiency at higher rotational speeds, which reduces the contact time between the drill

bit and the workpiece. Higher spindle speeds facilitate smoother chip evacuation and lower frictional resistance at the tool-workpiece interface, thereby decreasing the axial force required for material removal [18]. However, the relatively modest contribution of spindle speed (19.90% to thrust force variation, as per ANOVA results) suggests that its effect is less pronounced compared to other parameters, likely due to the anisotropic nature of the composite, which limits the extent of speed-induced force reduction. The main effects plot illustrates this subtle downward trend, with a shallow negative slope, underscoring the need for balanced spindle speed settings to avoid excessive heat generation, which could induce thermal damage in the epoxy matrix [19].

In contrast, feed rate exhibits a strong positive correlation with thrust force, as evidenced by the steep upward slope in the main effects plot. As the feed rate increases from 10 to 50 mm/min, the thrust force rises proportionally, contributing 7.16% to the total variation. This near-linear relationship reflects the dominance of mechanical forces in the drilling process, where higher feed rates increase the rate of material removal, leading to greater resistance from the composite [20]. The increased feed rate amplifies the shear and compressive stresses at the cutting zone, necessitating higher axial forces to advance the drill [21]. This behavior is consistent with the composite's heterogeneous structure, where the epoxy matrix and carbon dot reinforcements create varying resistance to tool penetration [22]. The linear progression observed in the plot suggests that feed rate increments produce predictable, proportional increases in thrust force, making it a critical parameter for controlling machining-induced stresses and minimizing defects such as delamination.

The drill bit diameter emerges as the dominant factor influencing thrust force, contributing 66.18% to the variation, as confirmed by the ANOVA results. The main effects plot demonstrates a strong positive relationship, with thrust force increasing significantly as the diameter rises from 0.3 to 0.9 mm. This trend is driven by the larger tool-workpiece contact area associated with wider drill bits, which increases the volume of material removed per revolution and amplifies the cutting forces required. The larger diameter also enhances the shear and compressive stresses at the cutting interface, leading to higher axial loads [23]. Additionally, the increased chip load with larger diameters contributes to greater resistance, further elevating the thrust force [24]. The pronounced slope in the plot underscores the critical role of tool geometry in drilling performance, highlighting the need for careful diameter selection to balance material removal efficiency with the risk of machining-induced damage, such as matrix cracking or fiber pull-out.

The incorporation of carbon dot nanoparticles up to 1 wt.% results in a notable reduction in thrust force, as observed in the main effects plot. This reduction is attributed to the enhanced interfacial bonding and load distribution within the composite, facilitated by the uniform dispersion of carbon dots within the epoxy matrix. Carbon dots, with their high surface area and unique mechanical properties, strengthen the matrix-reinforcement interface, improving the composite's resistance to shear and compressive forces during drilling [25-26]. This leads to a more efficient stress transfer, reducing the axial force required for material removal. However, the plot also indicates that increasing carbon dot concentrations beyond 1 wt.% induces material embrittlement, characterized by a transition from ductile to brittle fracture behavior. This shift is likely due to the agglomeration of nanoparticles at higher concentrations, which creates stress concentration points and weakens the matrix integrity. As a result, the composite becomes more susceptible to brittle fracture, reducing the thrust force but potentially compromising structural integrity at critical concentrations. This dual effect of carbon dot reinforcement underscores the importance of optimizing nanoparticle content to achieve a balance between enhanced mechanical properties and machining performance.

The interplay of these parameters, as visualized in the main effects plot, provides a robust framework for understanding the drilling behavior of carbon dot-reinforced epoxy composites. The significant influence of drill bit diameter, coupled with the linear effect of feed rate and the subtle mitigating effect of spindle speed, highlights the need for a holistic approach to parameter optimization.

3.4. Optimization

In this section, desirability method is conducted to determine the optimized condition to obtain least possible thrust force. In this order, desirability amount (d) will be acquired from the "Eq. (2)" and "Eq. (3)" relationships:

$$d_i = \begin{cases} 1 & Y_i < Low_i \\ \left(\dfrac{Y_i - Low_i}{High_i - Low_i}\right)^w & Low_i < Y_i < High_i \\ 0 & Y_i > High_i \end{cases} \tag{2}$$

$$D = \left(\prod_{i=1}^{n} d_i^{r_i}\right)^{1/\sum r_i} \tag{3}$$

That Y is the thrust force factor, Low and High are the minimal and maximal thrust force values, respectively, r is the number of experimental tests and w is the weigh coefficients. Figure 5, an optimization plot, illustrates the impact of spindle speed, feed rate, drill bit diameter,

and carbon dot concentration on thrust force during drilling of carbon dot-reinforced epoxy composites. Each panel shows the parameter's range on the x-axis and predicted thrust force on the y-axis, with red lines marking current (Cur) and high/low settings, and a blue dashed line indicating the target minimum thrust force (y = 0.0639, desirability d = 0.98552). The settings—spindle speed of 2500 rpm, feed rate of 10 mm/min, tool diameter of 0.3 mm, and 1 wt.% carbon-dot—minimize thrust force effectively, ensuring better hole quality and structural integrity.

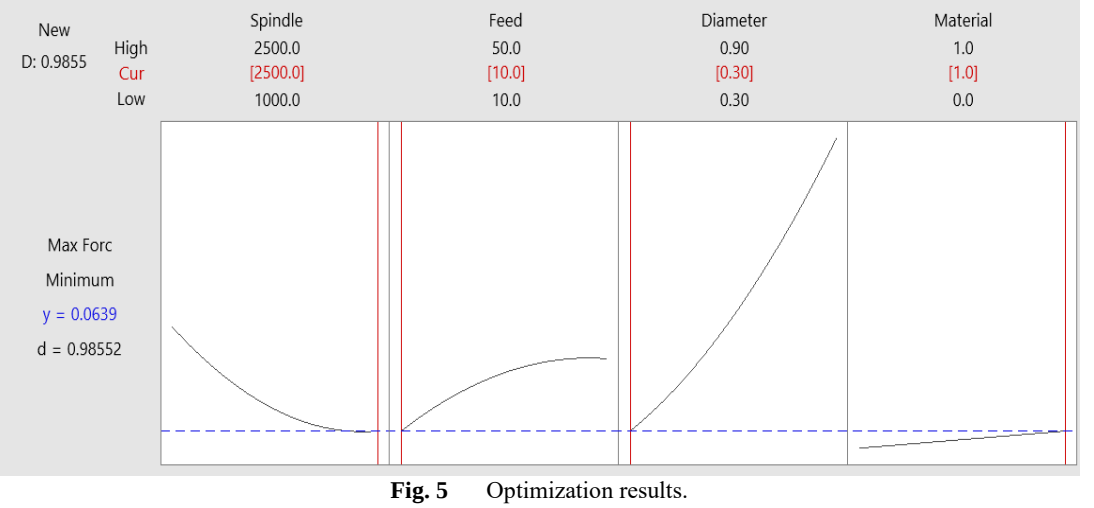

Fig. 5 Optimization results.

4 CONCLUSIONS

This study examined the effects of drilling parameters—spindle speed, feed rate, and drill bit diameter—on thrust force during the machining of epoxy composites reinforced with carbon dot nanoparticles. Drill bit diameter was identified as the most influential factor (66.18%), followed by spindle speed (19.90%) and feed rate (7.16%). A regression model (R^2 = 98.90%) confirmed significant parameter interactions. Increased feed rate and tool diameter raised thrust force, while higher spindle speeds reduced it slightly. Carbon dot additions up to 1 wt.% lowered thrust forces through improved bonding, though higher contents led to embrittlement and brittle fracture. The optimal drilling conditions (2500 rpm, 10 mm/min feed rate, 0.3 mm diameter, and 1 wt.% carbon dots) minimized thrust force (0.0639 N) with high desirability (0.98552), offering valuable insights for precision machining of nanocomposites in advanced applications.

REFERENCES

[1] Nasrollahzadeh, M., Sajadi, S. M., Sajjadi, M., and Issaabadi, Z., An Introduction to Nanotechnology, Interface Science and Technology, Elsevier, Vol. 28, 2019. pp. 1-27.

[2] Saba, N., Jawaid, M., Alothman, O. Y., Paridah, M., and Hassan, A., Recent Advances in Epoxy Resin, Natural Fiber-Reinforced Epoxy Composites and Their Applications, Journal of Reinforced Plastics and Composites, Vol. 35, No. 6, 2016, pp. 447-70.

[3] Liu, J., Li, R., and Yang, B., Carbon Dots: A New Type of Carbon-Based Nanomaterial with Wide Applications. ACS Central Science, Vol. 6, No. 12, 2020, pp. 2179-95.

[4] Abdel-Galil, A., Ali, H., and Balboul, M., Influence of CDS Nano-Additives on Optical, Thermal and Mechanical Performance of CDS/Polyvinyl Alcohol Nanocomposites, Optik, Vol. 129, 2017, pp. 153-62.

[5] Hintze, W., Hartmann, D., and Schütte, C., Occurrence and Propagation of Delamination During the Machining of Carbon Fibre Reinforced Plastics (CFRPs)–An Experimental Study. Composites Science and Technology, Vol. 71, No. 15, 2011, pp. 1719-26.

[6] Marques, A. T., Durão, L. M., Magalhães, A. G., Silva, J. F., and Tavares, J. M. R., Delamination Analysis of Carbon Fibre Reinforced Laminates: Evaluation of a Special Step Drill, Composites Science and Technology, Vol. 69, No. 14, 2009, pp. 2376-82.

[7] Teti, R., Machining of Composite Materials, CIRP Annals, Vol. 51, No. 2, 2002, pp. 611-34.

[8] Liu, D., Tang, Y., and Cong, W., A Review of Mechanical Drilling for Composite Laminates, Composite Structures, Vol. 94, No. 4, 2012, pp. 1265-79.

[9] Gao, C., Xiao, J., Xu, J., and Ke, Y., Factor Analysis of Machining Parameters of Fiber-Reinforced Polymer Composites Based on Finite Element Simulation with Experimental Investigation, The International Journal of Advanced Manufacturing Technology, Vol. 83, No. 5, 2016, pp. 1113-25.

[10] Poulachon, G., Outeiro, J., Ramirez, C., André, V., and Abrivard, G., Hole Surface Topography and Tool Wear in CFRP Drilling, Procedia CIRP, Vol. 45, 2016, pp. 35-8.

[11] Tsao, C., Taguchi Analysis of Drilling Quality Associated With Core Drill In Drilling of Composite Material, The International Journal of Advanced Manufacturing Technology, Vol. 32, No. 9, 2007, pp. 877-84.

[12] Wang, D., Jiao, F., and Mao, X., Mechanics of Thrust Force on Chisel Edge in Carbon Fiber Reinforced Polymer (CFRP) Drilling Based on Bending Failure Theory, International Journal of Mechanical Sciences, Vol. 169, 2020, pp. 105336.

[13] Magyar, G., Geier, N., Analysis and Modelling of Thrust Force in Drilling of Basalt And Carbon Fibre-Reinforced Polymer (BFRP and CFRP) Composites, Journal of the Brazilian Society of Mechanical Sciences and Engineering, Vol. 45, No. 6, 2023, pp. 323.

[14] Colligan, K., Ramulu, M., The Effect of Edge Trimming on Composite Surface Plies, Manufacturing Review(USA), Vol. 5, No. 4, 1992, pp. 274-83.

[15] Wei, Y., An, Q., Ming, W., and Chen, M., Effect of Drilling Parameters and Tool Geometry on Drilling Performance in Drilling Carbon Fiber–Reinforced Plastic/Titanium Alloy Stacks, Advances in Mechanical Engineering, Vol. 8, No. 9, 2016, pp. 1687814016670281.

[16] Pathak, A. K., Borah, M., Gupta, A., Yokozeki, T., Dhakate, S. R., Improved Mechanical Properties of Carbon Fiber/Graphene Oxide-Epoxy Hybrid Composites, Composites Science and Technology, Vol. 135, 2016, pp. 28-38.

[17] Baraheni, M., Soudmand, B. H., Amini, S., Bayat, M., and Ebrahimi, A., Burr Constitution Analysis in Ultrasonic-Assisted Drilling of CFRP/Nano-Graphene Via Experimental and Data-Driven Methodologies, Journal of Reinforced Plastics and Composites, Vol. 44, No. 11-12, 2025, pp. 602-19.

[18] Fereiduni, F., Ansari, M., and Baraheni, M., The Role of Drilling Parameters in Controlling Delamination and Hole Quality of Novel Long-Fiber PLA-Glass Composites Manufactured by FDM, Iranian Journal of Manufacturing Engineering, 2025.

[19] Baraheni, M., Amini, S., Ultrasonic Vibratory Drilling Carbon Fiber/Graphene Nanoparticle Reinforced Polymers to Produce Desired Hole Quality: Experimental Analysis and Optimization, AUT Journal of Mechanical Engineering, Vol. 9, No. 2, 2025, pp. 195-210.

[20] Baraheni, M., Soudmand, B., and Amini, S., Delamination Assessment and Prediction in Ultrasonic-Assisted Drilling of Laminated Hybrid Composites, Proceedings of the Institution of Mechanical Engineers, Part E: Journal of Process Mechanical Engineering, 2024, pp. 09544089241293584.

[21] Hoseini, S. M., Akbari, J., Drilling of Engineering Ceramics using Combination of Ultrasonic Vibrations and Diamond Slurry, 2013.

[22] Baraheni, M., Amini, S., Influence of Machining Condition and Nano-Graphene Incorporation on Drilling Load and Hole Quality in Both Conventional Drilling and Ultrasonic-Assisted Drilling of CFRP, Arabian Journal for Science and Engineering, Vol. 49, No. 11, 2024, pp. 14593-606.

[23] Baraheni, M., Hoseini, A. M., and Najimi, M. R., Investigation on Carbon Fiber-Reinforced Polymer Combined with Graphene Nanoparticles Subjected to Drilling Operation Using Response Surface Methodology and Non-Dominated Sorting Genetic Algorithm-II, Proceedings of the Institution of Mechanical Engineers, Part E: Journal of Process Mechanical Engineering, 2024, pp. 09544089241230160.

[24] Baraheni, M., Khoshdoni Farahani, R., and Malekhoseini, A., Exprimental Study on Effect of Machining Parametrs in Slotting Polymers Reinforced by Carbon Fibers and MWCNT Nanoparticles, Modares Mechanical Engineering, Vol. 23, No. 10, 2023, pp. 57-62.

[25] Latif, Z., Ali, M., Lee, E. J., Zubair, Z., and Lee, K. H., Thermal and Mechanical Properties of Nano-Carbon-Reinforced Polymeric Nanocomposites: A Review, Journal of Composites Science, Vol. 7, No. 10, 2023, pp. 441.

[26] Saini, V. K., Khan, Z. A., and Siddiquee, A. N., Developments in Conventional Machining of Aluminium Matrix Composite Material: A Review, 2014.